

RADC-TR-78-164
Final Technical Report
July 1978

12
NW

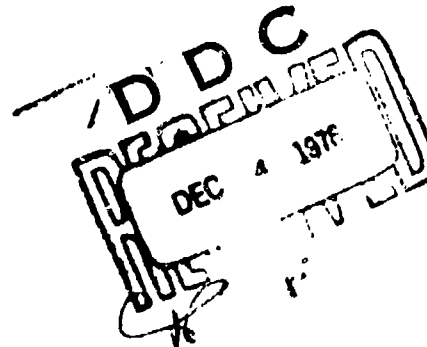
LEVEL



IMPURITY INDUCED ABSORPTION IN POTASSIUM BROMIDE
CRYSTALS FOR INFRARED OPTICAL APPLICATIONS

A. J. Sievers A. Chraplyvy
R. O. Pohl D. Pramanik
R. Alexander G. Schmidt
Y. Chabal

Cornell University



Approved for public release; distribution unlimited.

DDC FILE COPY
ADA061794

ROME AIR DEVELOPMENT CENTER
Air Force Systems Command
Griffiss Air Force Base, New York 13441

78 11 23 003

This report has been reviewed by the RADC Information Office (OI) and is releasable to the National Technical Information Service (NTIS). At NTIS it will be releasable to the general public, including foreign nations.

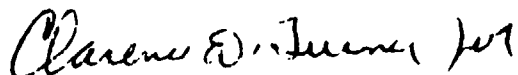
RADC-TR-78-164 has been reviewed and is approved for publication.

APPROVED:



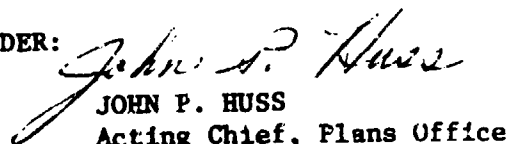
LYN H. SKOLNIK
Project Engineer

APPROVED:



ROBERT M. BARRETT, Director
Solid State Sciences Division

FOR THE COMMANDER:


JOHN P. HUSS
Acting Chief, Plans Office

If your address has changed or if you wish to be removed from the RADC mailing list, or if the addressee is no longer employed by your organization, please notify RADC (ESE) Hanscom AFB MA 01731. This will assist us in maintaining a current mailing list.

Do not return this copy. Retain or destroy.

UNCLASSIFIED

SECURITY CLASSIFICATION OF THIS PAGE (When Data Entered)

| REPORT DOCUMENTATION PAGE | | READ INSTRUCTIONS BEFORE COMPLETING FORM |
|--|---|--|
| 1. REPORT NUMBER RADCTR-78-164 | 2. GOVT ACCESSION NO. | 3. RECIPIENT'S CATALOG NUMBER |
| 4. TITLE (If not elsewhere indicated) | | TYPE OF REPORT & PERIOD COVERED Final Technical Report 1 April 1975 - 31 March 1977 |
| IMPURITY INDUCED ABSORPTION IN POTASSIUM BROMIDE CRYSTALS FOR INFRARED OPTICAL APPLICATIONS | | 5. PERFORMING ORG. REPORT NUMBER N/A |
| 7. AUTHOR(s) A. J. Sievers R. O. Pohl R. Alexander Y. Chabal | A. Chraplyvy D. Pramanik G. Schmidt | 6. CONTRACT OR GRANT NUMBER(s) 15 F19628-75-C-0177 |
| 9. PERFORMING ORGANIZATION NAME AND ADDRESS Cornell University Ithaca NY 14850 | | 10. PROGRAM ELEMENT, PROJECT, TASK AREA & WORK UNIT NUMBERS 61101E D900ARAA 11 A.V. |
| 11. CONTROLLING OFFICE NAME AND ADDRESS Deputy for Electronic Technology (RADC/ESE) Hanscom AFB MA 01731 Monitor/Lyn H. Skolnik/ESE | | 12. REPORT DATE July 1978 |
| 14. MONITORING AGENCY NAME & ADDRESS(if different from Controlling Office) | | 13. NUMBER OF PAGES 152 |
| Same | | 15. SECURITY CLASS. (of this report) UNCLASSIFIED |
| 16. DISTRIBUTION STATEMENT (of this Report) Approved for public release; distribution unlimited. 1471 | | 15a. DECLASSIFICATION/DOWNGRADING SCHEDULE N/A |
| 17. DISTRIBUTION STATEMENT (for the abstract entered in Block 20, if different from Report) Same | | |
| 18. SUPPLEMENTARY NOTES RADC Project Engineer: Lyn H. Skolnik (ESE) | | |
| 19. KEY WORDS (Continue on reverse side if necessary and identify by block number) Low Absorption Coefficients Laser Window Materials Alkali Halides M1411 | | |
| 20. ABSTRACT (Continue on reverse side if necessary and identify by block number) Investigations of the optical properties of "pure" and doped alkali halide crystals between 9 μ m and 11 μ m were carried out using CO ₂ lasers and Michelson interferometers. The extrinsic absorption due to residual impurities in purified alkali halides was used to categorize the optical quality of the crystals. The absorption in doped crystals was studied both interferometrically from which the internal vibrational modes of the molecular impurities were identified and by means of saturation spectroscopy from which excited-state | | |

lifetimes of molecular vibrations were determined.

The absorption coefficients of the ultratransparent ($\alpha \approx 10^{-3} \text{ cm}^{-1}$) alkali halides were measured between 923 cm^{-1} and 1080 cm^{-1} using a vacuum laser calorimeter in conjunction with a tunable CO_2 laser. All the alkali halides investigated have an absorption resonance in the region of $9.6 \mu\text{m}$ which deviates from the exponentially decreasing frequency dependence of α predicted by theory. This absorption resonance was found to be primarily a surface absorption. The effect of various purification techniques on the $10 \mu\text{m}$ optical purity of KBr crystals was examined. Reactive atmosphere treatment of the starting material as well as slow growths produced KBr crystals with absorption coefficients $\approx 10^{-4} \text{ cm}^{-1}$. Bridgeman-grown crystals oriented along the [111] direction were found to be superior to Czochralski-grown crystals. The degradation of the absorption coefficient due to polishing and divalent ion doping was also investigated.

Various alkali halides were doped with ReO_4^- impurities whose v_3 internal vibrational modes are infrared active and in close coincidence with CO_2 laser lines. The impurity absorption was studied as a function of host lattice and temperature using a Michelson interferometer and a helium-cooled detector. The absorption spectra of the ReO_4^- impurities indicate that the impurities undergo some degree of motion in the larger hosts (KI, RbI) but are "locked" in smaller lattices (KBr). The absorption of laser radiation by the ReO_4^- impurities was studied as a function of temperature and incident laser intensity. Using a pulsed-discharge Q-switched CO_2 laser the v_3 absorption of ReO_4^- in a KI lattice was partially or totally saturated at all temperatures between 300 K and 1.3 K. The saturation data were analyzed using rate-equation theory and the excited-state lifetimes of the v_3 vibration were computed. The lifetimes range from as short as 80 psec at 300 K to longer than 10 nsec at 1.3 K. Similar experiments were performed on KBr + ReO_4^- at 100 K yielding an excited-state lifetime of 16 nsec.

Below 18 K the KI + ReO_4^- samples exhibited a peculiar threshold effect when irradiated by intense CO_2 laser pulses. Q-switched laser pulses with intensities greater than about 500 kW/cm^2 were not only attenuated but distorted by the samples (the peaks of the pulses were absorbed or scattered from the forward direction). This effect was shown not to be the breakup of $n2\pi$ pulses. A variety of processes were eliminated as possible sources for this new threshold effect.

UNCLASSIFIED

EVALUATION

1. This report is the Final Report of the contract. It covers research done on impurity absorption in infrared nearly transparent materials during the period 1 April 1975 to 31 March 1977. The objective of the work is to study the causes of residual absorption in potential high power laser window materials, particularly alkali halides and to devise optical techniques for quantitatively measuring concentrations of low level impurities and for identifying species which are responsible for optical absorption at key high power laser frequencies. A new approach to measuring surface absorption losses utilizing optically guided surface waves was developed which may lead to identification of impurity losses in antireflection coatings for laser windows. Coating losses are now believed in many cases to be the limiting factor in developing environmentally and optically sound high energy laser windows.
2. The above work is of value since it provides the basic knowledge and understanding required to improve present materials which are candidates for high power laser windows and optical coatings.


LYN H. SKOLNIK
Project Engineer

| | |
|--------------------------------------|---|
| ACQUISITION OR | |
| NTIS | 1.0 Section <input checked="" type="checkbox"/> |
| DDC | 3.0 Section <input type="checkbox"/> |
| UNANNOUNCED <input type="checkbox"/> | |
| JUSTIFICATION | |
| BY | |
| DISTRIBUTION/AVAILABILITY CODES | |
| DR | SPECIAL |
| F | |

Table of Contents

| | Page |
|--|------|
| I. INTRODUCTION | 1 |
| II. ULTRATRANSPARENT CRYSTALS AND LASER CALORIMETRY | 6 |
| A. Introduction | 6 |
| B. Calorimetry | 7 |
| C. CO ₂ Laser: Modified Apollo cw Laser | 19 |
| 1. Construction | 19 |
| 2. cw and Pulsed Optical Characteristics | 24 |
| D. Sample Preparation | 29 |
| E. Results | 31 |
| F. Conclusions | 44 |
| III. ABSORPTION, SATURATION AND EXCITED STATE LIFETIMES OF IMPURITIES IN ALKALI HALIDES | 45 |
| A. Introduction | 45 |
| B. Microsecond CO ₂ Laser Pulses | 48 |
| 1. Q-switched CO ₂ Laser (cw Discharge) | 48 |
| 2. Pulsed-Discharge Q-Switched CO ₂ Laser | 62 |
| 3. Precursor Pulses | 69 |
| C. Detectors and Cryostats | 71 |
| 1. Room Temperature Detectors | 71 |
| a. Thermopile | 71 |
| b. Moletron Pyroelectric Detector | 71 |
| c. Laser Precision Pyroelectric Detector | 72 |
| d. Japanese Pyroelectric Detector | 72 |
| 2. Cryogenic Detectors | 73 |
| a. Santa Barbara Ge:Cu Detector I | 73 |
| b. Santa Barbara Ge:Cu Detector II | 73 |
| c. 1.2 K Ge Bolometer | 73 |
| 3. Cryostats | 73 |
| a. Near Infrared Helium Immersion Cryostat | 73 |
| b. Liquid Nitrogen Cryostat | 75 |
| c. Far Infrared Cryostat | 78 |
| D. Interferometry and Raman Spectroscopy | 81 |
| 1. Apparatus | 81 |
| 2. Results | 81 |
| a. Infrared Absorption | 81 |
| b. Raman Scattering | 90 |

Table of Contents (continued)

| | Page |
|--|------|
| III. ABSORPTION, SATURATION AND EXCITED STATE LIFETIMES OF IMPURITIES IN ALKALI HALIDES (continued) | |
| E. Theory of Incoherent Saturation | 96 |
| 1. Phenomenological Decay Constants | 97 |
| 2. Rate Equation Theory of Saturation | 98 |
| a. Steady State Solution for Homogeneously Broadened Lines | 98 |
| b. Steady State Solution for Inhomogeneously Broadened Lines | 101 |
| c. Dynamic Solution | 104 |
| F. Absorption and Saturation Measurements | 106 |
| 1. Experimental | 106 |
| 2. Sample Preparation | 108 |
| G. Results of Saturation and Excited State Lifetime Measurements | 109 |
| H. Pulse Attenuation and Reshaping | 119 |
| References | 135 |

List of Tables

| | Page |
|--|------|
| Table II-1. State of the art sensitivities of various tech- niques for measuring low bulk and surface absorption coefficients | 8 |
| Table II-2. Specifications of modified Apollo CO ₂ laser | 22 |
| Table II-3. Summary of calorimetric results for alkali halides measured during Infrared Laser Window Project | 32 |
| Table III-1. Tuning range of Q-switched CO ₂ laser using gas mixture I | 68 |
| Table III-2. Summary of Raman scattering and infrared absorption measurements of internal vibrational modes of ReO ₄ ⁻ in alkali halides | 93 |
| Table III-3. Summary of saturation data for KI + ReO ₄ ⁻ and KBr + ReO ₄ ⁻ | 112 |

List of Figures

| | Page |
|--|------|
| Figure II-1. Schematic diagram of laser calorimetry experiment | 9 |
| Figure II-2. Typical experimental laser calorimetry data | 10 |
| Figure II-3. Schematic diagram of room temperature vacuum calorimeter | 12 |
| Figure II-4. Calorimetric data with some direct scattering of laser radiation to the thermocouple | 14 |
| Figure II-5. Two calorimetric temperature vs. time curves (with and without scattering at the end faces of the sample) | 15 |
| Figure II-6. Plots of fractional power absorbed as a function of length | 17 |
| Figure II-7. Sample temperature vs. time curve for "long-rod" geometry sample with nonzero surface absorption | 18 |
| Figure II-8. Schematic diagram of the modified Apollo CO ₂ laser | 21 |
| Figure II-9. Transmission vs. frequency of output coupling mirror on the Apollo laser | 23 |
| Figure II-10. Maximum cw output power of modified Apollo laser | 25 |
| Figure II-11. Maximum output peak power of modified Apollo laser operating in the chopped mode | 26 |
| Figure II-12. Maximum output peak power of modified Apollo laser operating in the pulsed mode | 27 |
| Figure II-13. Photograph of CO ₂ pulse from the modified Apollo laser operating in the chopped mode | 28 |
| Figure II-14. Photograph of CO ₂ pulse from the modified Apollo laser operating in the pulsed mode | 30 |
| Figure II-15. Absorption coefficient vs. frequency for two different KBr crystals | 35 |
| Figure II-16. Comparison of absorption coefficient in KCl and KBr in the 10 μm region | 36 |

List of Figures (continued)

| | Page |
|--|------|
| Figure II-17. Absorption coefficient vs. frequency for a KBr crystal showing the absorption near 1900 cm^{-1} measured with a CO laser | 37 |
| Figure II-18. Plot of absorption channel (bulk or surface) vs. frequency for KBr crystal | 39 |
| Figure III-1. Schematic diagram of tunable Q-switched CO_2 laser | 49 |
| Figure III-2. Shape (intensity vs. time) of typical Q-switched CO_2 laser pulse | 50 |
| Figure III-3. Peak Q-switched power vs. mirror frequency for P(8), P(20), P(36) lines of the (00 0 1-10 0 0) band using gas mixture I | 53 |
| Figure III-4. Peak Q-switched power vs. mirror frequency for R(8), R(22), R(32) lines of the (00 0 1-10 0 0) band using gas mixture I | 54 |
| Figure III-5. Peak Q-switched power vs. discharge current for P(8), P(20), P(36) lines of the (00 0 1-10 0 0) band using gas mixture I | 55 |
| Figure III-6. Peak Q-switched power vs. discharge current for R(8), R(22), R(32) lines of the (00 0 1-10 0 0) band using gas mixture I | 56 |
| Figure III-7. Peak Q-switched power vs. laser gas pressure for P(8), P(20), P(36) lines of the (00 0 1-10 0 0) band using gas mixture I | 57 |
| Figure III-8. Peak Q-switched power vs. laser gas pressure for R(8), R(22), R(32) lines of the (00 0 1-10 0 0) band using gas mixture I | 58 |
| Figure III-9. Intensity vs. time plots of various Q-Q-switched pulses showing some distorted pulses | 60 |
| Figure III-10. Schematic diagram of the pulsed-discharge Q-switched CO_2 laser | 63 |
| Figure III-11. Schematic diagram of photo-diode trigger circuit | 64 |

List of Figures (continued)

| | Page |
|--|------|
| Figure III-12. Schematic diagram of variable pulse width, variable delay circuit which controls the laser discharge during pulsed-discharge Q-switching | 65 |
| Figure III-13. Optimum relative temporal orientation of discharge pulse with respect to optical pulse | 67 |
| Figure III-14. Photograph of precursor pulse preceding the main pulse in the chopped or pulsed mode of the Apollo laser | 70 |
| Figure III-15. Schematic diagram of pumped-helium immersion cryostat for near infrared optical measurements | 74 |
| Figure III-16. Window holder design for cold windows in the immersion cryostat | 76 |
| Figure III-17. Schematic diagram of liquid nitrogen cold-finger cryostat | 77 |
| Figure III-18. Schematic diagram of 1.2 K bolometer cryostat and sample insert | 79 |
| Figure III-19. Bias circuit for 1.2 K Ge bolometer | 80 |
| Figure III-20. Schematic diagram of Raman spectrometer used for Raman scattering experiments | 82 |
| Figure III-21. Transmission spectrum of KBr + .6% KReO ₄ at 1.2 K in the region of the v ₂ absorption of ReO ₄ ⁻ | 84 |
| Figure III-22. Transmission spectrum of KI + .4% KReO ₄ at 1.2 K in the region of the v ₂ absorption of ReO ₄ ⁻ | 85 |
| Figure III-23. Transmission spectrum of RbI + .8% KReO ₄ at 1.2 K in the region of the v ₂ absorption of ReO ₄ ⁻ | 86 |
| Figure III-24. Transmission spectrum of KBr + .6% KReO ₄ at 1.3 K in the region of the v ₃ absorption of ReO ₄ ⁻ | 87 |

List of Figures (continued)

| | Page |
|---|------|
| Figure III-25. Transmission spectrum of KI + .3% KReO ₄ at 1.3 K in the region of the ν_3 absorption of ReO ₄ ⁻ | 88 |
| Figure III-26. Transmission spectrum of RbI + .8% KReO ₄ at 1.3 K in the region of the ν_3 absorption of ReO ₄ ⁻ | 89 |
| Figure III-27. Raman spectrum of KI + .2% KReO ₄ at 8 K | 92 |
| Figure III-28. Experimental arrangement for absorption and saturation measurements | 107 |
| Figure III-29. Cross section of ReO ₄ ⁻ impurity molecules in KI as a function of temperature | 111 |
| Figure III-30a. Excited state lifetime T_1 of the ν_3 vibrational mode of ReO ₄ ⁻ impurities in KI as a function of temperature assuming a homogeneously broadened absorption line | 113 |
| Figure III-30b. Excited state lifetime T_1 of the ν_3 vibrational mode of ReO ₄ ⁻ impurities in KI as a function of temperature assuming homogeneous broadening above 100 K and extreme inhomogeneous broadening at 1.3 K | 116 |
| Figure III-30c. Range of possible excited state lifetime of ν_3 vibrational mode of ReO ₄ ⁻ impurities in KI as a function of temperature | 118 |
| Figure III-31. Pulse distortion of millisecond-long pulses by .021-inch thick KI + ReO ₄ ⁻ sample at 1.3 K | 121 |
| Figure III-32. Magnified view of pulse distortion by KI + ReO ₄ ⁻ sample | 122 |
| Figure III-33. Pulse distortion of microsecond Q-switched pulses by .056-inch thick KI + ReO ₄ ⁻ sample | 124 |
| Figure III-34. Pulse distortion of Q-switched pulses by .164-inch thick KI + ReO ₄ ⁻ sample | 125 |
| Figure III-35. Relative orientation of the P(42) CO ₂ laser frequency to the absorption line of ReO ₄ ⁻ impurities in KI + Cs ⁺ at low temperatures | 130 |
| Figure III-36. Diagram of a Raman scattering process originating in the ν_3 vibrational state and ending in the ν_1 vibrational state | 133 |

Chapter I

INTRODUCTION

Vibrational modes of impurities and defects in alkali halides have been the subject of study for nearly fifty years. Maslakowez¹ first studied internal vibrational modes of impurities in alkali halides in 1928. A few years later the first defect-induced lattice absorption was observed in diamond by Robertson *et al.*² The first observation of a local mode occurred in 1958³ and since then there has been a flurry of experimental and theoretical activity in the field of defect- and impurity-induced absorption in alkali halides. References to most of the work done on disordered solids can be found in a comprehensive review article by Barker and Sievers.⁴

Many of the optical studies of impurity and defect absorption have taken place in the far infrared spectral region. More recently, however, there has been a shift in interest from the far infrared to the near infrared spectral region. The need for optical components for high power lasers has led to a concerted effort to understand impurity absorption in the near ir especially in the spectral regions in which high power gas lasers operate ($\text{CO}_2 \sim 9\text{-}11 \mu\text{m}$, $\text{CO} \sim 5\text{-}5.3 \mu\text{m}$, $\text{DF} \sim 3.6\text{-}4.1 \mu\text{m}$, $\text{HF} \sim 2.6\text{-}3.4 \mu\text{m}$).

A number of materials are theoretically suitable for use as highly transparent ir optics. Among these, alkali halides possess the best absorption properties around $10 \mu\text{m}$. However, the residual absorption measured in alkali halides for the most part has not been intrinsic, i.e. the absorption is due to impurities rather than to

multiphonon processes intrinsic to a perfect lattice. It is the elimination of the extrinsic absorption that has attracted the attention of many researchers. The first ultrapure alkali halides to be studied experimentally in the 10 μm region were KCl and KBr.^{5,6} KCl and KBr along with NaCl are the only alkali halides seriously considered for use as ir laser windows because although heavier salts such as KI should have lower ir absorption coefficients, they also possess poorer mechanical properties.

Perhaps one weakness in these recent studies on infrared absorption in alkali halides is the empirical nature of most investigations. Numerous crystal growing and purification techniques have been tried in order to reduce existing absorption coefficients and some of them have been successful. However, very little work has been done to understand the interaction between impurities, the host lattices and ir radiation. Knowledge of such interactions will not only give a good indication of what impurities should be considered (i.e., small molecules vs. large molecules vs. monatomic impurities, 2-dimensional vs. 3-dimensional impurities, etc.) in further purification attempts, but will also aid in understanding how residual impurities will behave in the presence of intense external radiation fields.

This thesis describes some of the work done on the Infrared Window Project at Cornell University and is divided into two major sections. The first section (Chapter II) deals with the study of the extrinsic absorption in KBr crystals in the 9-11 μm spectral region. In "pure" crystals these absorptions are extremely small ($<10^{-3} \text{ cm}^{-1}$) and

therefore special techniques are required to be able to detect such low levels of absorption. A laser calorimeter has been constructed to measure the minuscule losses in KBr crystals in the vicinity of 10 μm . Both bulk and surface absorption are of interest and both are monitored using calorimetric techniques. The effects of various purification, growing, and surface preparation techniques on the 10 μm absorption coefficient of KBr are also investigated. Divalent alkaline earth impurities are purposely doped into KBr crystals (which increases the structural strength of the crystals) and the effect on the absorption coefficient is studied. The 10 μm absorption of other alkali halides is also investigated and it is found that all the alkali halides studied thus far exhibit anomalous bulk and surface absorption coefficients near 9.8 μm .

The second section (Chapter III) of the thesis is devoted to a much more basic problem. The interaction of an impurity-lattice system with CO₂ laser radiation is investigated. Various alkali halides were purposely doped with ReO₄⁻ molecules* which enter the lattice substitutionally in place of a halide ion. The absorption properties of the ν_3 internal vibrational mode of the ReO₄⁻ impurity molecules were studied in the 10 μm region as a function of temperature and laser intensity. We found that the ν_3 absorption of ReO₄⁻ in a KI lattice can be partially or totally saturated at all temperatures between 300 K and 1.3

* ReO₄⁻ molecules in alkali halides serve as ideal model systems for laser studies of impurity-lattice interactions. The ReO₄⁻ molecule is easily doped into nearly all alkali halides and possesses an infrared active vibrational mode in the CO₂ laser tuning range.

K for sufficiently high laser intensity. The threshold saturation intensity decreases as the sample temperature is lowered. Partial saturation of the same vibrational mode of ReO_4^- in a KBr matrix at 100 K has also been observed. To the best of our knowledge this represents the first observation of saturation of an internal vibrational model of an impurity embedded in a solid matrix. From the saturation data the vibrational excited state lifetimes of the ReO_4^- impurities can be determined and lifetimes as low as 10 picoseconds can be measured using a Q-switched CO_2 laser putting out pulses greater than 500 nsec long. The results of such measurements, as well as the theoretical background, are presented in Chapter III.

Chapter III also contains a section describing a series of puzzling effects observed in the $\text{KI} + \text{ReO}_4^-$ samples. The effects observed are pulse attenuation and reshaping processes in which a variety of pulses (some as long as several milliseconds, others as short as 1 μsec) are attenuated and distorted by the sample at low temperatures (<18 K). There is a distinct threshold incident intensity ($\sim 500 \text{ kW/cm}^2$) associated with these effects which is slightly temperature dependent (it is about 100 kW/cm^2 lower for the 5-15 K region than for the 1.3-5 K and 15-18 K regions). Below this threshold intensity transmitted pulses are undistorted while pulses with peak intensities greater than the threshold intensity are reshaped into multiply-peaked or flat-topped pulses. A variety of processes are investigated as possible explanations for these pulse-reshaping effects.

The studies described in this thesis have also been fruitful from

a technical standpoint. Numerous technical difficulties such as low temperature 10 μm window seals and Q-switching of very weak CO₂ laser lines were overcome to make these projects successful.

Not all the contributions to the Infrared Laser Window Project have been included in this thesis. For example, ultra-transparent protective surface coatings for high power laser optics have attracted nearly as much attention as the study of bulk materials. Our novel contribution to this field is described in reference 7.

More detailed description of the contents of the subsequent chapters can be found in the introduction to each chapter.

Chapter II

ULTRATRSPARENT CRYSTALS AND LASER CALORIMETRY

A. Introduction

The study of highly transparent materials for high power laser applications has evolved fairly rapidly over the past few years.⁹ The transparent nature of these materials necessitated the development of new measurement techniques to detect minuscule absorptions. The work-horse of the techniques (and the one used in our laboratory) is laser calorimetry. Laser calorimetry is in principle a very straightforward measuring technique requiring only a cw laser and calorimeter. The experimental technique as well as the details of the calorimeter are described in the first section of this chapter. This will be followed by a section describing the cw and quasi-cw laser source (in our case a CO₂ laser) used in the calorimetry experiments. The third section describes the efforts to produce highly transparent KBr crystals for the 10 μm spectral region. The effects of various crystal purification and growing techniques on the 10 μm absorption coefficient are investigated. Two other alkali halides, KI and RbCl, are also briefly studied. One of the most interesting general results of these investigations is that all alkali halides measured thus far exhibit the same anomalous surface and bulk absorptions near 9.8 μm.

B. Calorimetry

Since conventional spectroscopic techniques are not suitable for measuring very low absorption coefficients ($\alpha < 10^{-3}$) numerous techniques

have been developed to detect minuscule losses in highly transparent optical materials.¹⁰ These techniques can be divided into two broad classes: direct loss methods¹⁰⁻¹⁷ and calorimetric methods.^{10,18-23}

The sensitivities of the various techniques are tabulated in Table II-1 taken from Hordvik.²⁴ Of all the techniques laser calorimetry²⁵⁻³⁰ is the most popular. The method is fairly straightforward and yields reproducible data when properly employed.

A schematic diagram of a laser calorimetry experiment is shown in Figure II-1. The sample is irradiated by a cw laser beam and the sample temperature is measured by a thermocouple and recorded as a function of time. A typical temperature vs. time curve is shown in Figure II-2. The absorption is related to the temperature change of the sample by the following formula.²⁶⁻²⁸

$$\alpha = \frac{mc}{LP_t} \left[\frac{dT}{dt} \text{ rise} \right]_{T_1} + \left| \frac{dT}{dt} \text{ decay} \right|_{T_1} \left(\frac{2n}{n^2+1} \right)$$

where m = mass of sample

c = specific heat of sample

L = sample length

n = index of refraction of sample

P_t = power transmitted through sample

$\frac{dT}{dt}$ rise) _{T_1} = slope of the heating curve at temperature T_1

$\frac{dT}{dt}$ decay) _{T_1} = the absolute value of the slope of the cooling curve at temperature T_1

Table II-1
State of the Art Sensitivities
Bulk Absorption (after Hordvik)

| | <u>Routine</u> | <u>Possible</u> |
|---------------------------|---------------------------------------|---------------------------------------|
| Transmission | 10^{-2} - 10^{-3} cm^{-1} | 10^{-4} - 10^{-5} cm^{-1} |
| Emittance | 10^{-4} - 10^{-5} cm^{-1} | 10^{-6} - 10^{-7} cm^{-1} |
| Thermocouple Calorimetry | 10^{-4} - 10^{-5} cm^{-1} | 10^{-6} cm^{-1} |
| Photoacoustic Calorimetry | 10^{-4} - 10^{-5} cm^{-1} | 10^{-6} cm^{-1} |
| D.C. Interf. Calorimetry | 10^{-4} cm^{-1} | 10^{-5} cm^{-1} |
| A.C. Interf. Calorimetry | --- | 10^{-6} cm^{-1} |

| | <u>Routine</u> | <u>Possible</u> |
|---------------------------|-----------------------|-----------------------|
| Transmission | 10^{-3} - 10^{-4} | 10^{-5} |
| Emittance | 10^{-4} - 10^{-5} | 10^{-6} - 10^{-7} |
| Thermocouple Calorimetry | 10^{-4} - 10^{-5} | 10^{-6} |
| Photoacoustic Calorimetry | 10^{-4} - 10^{-5} | 10^{-6} |

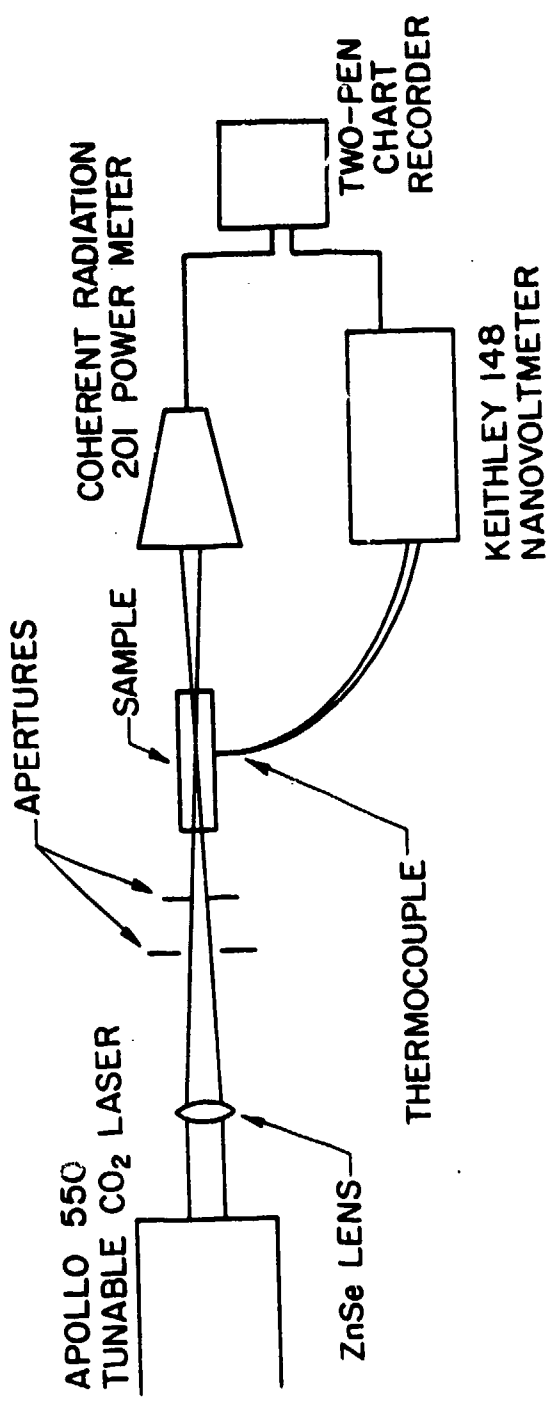
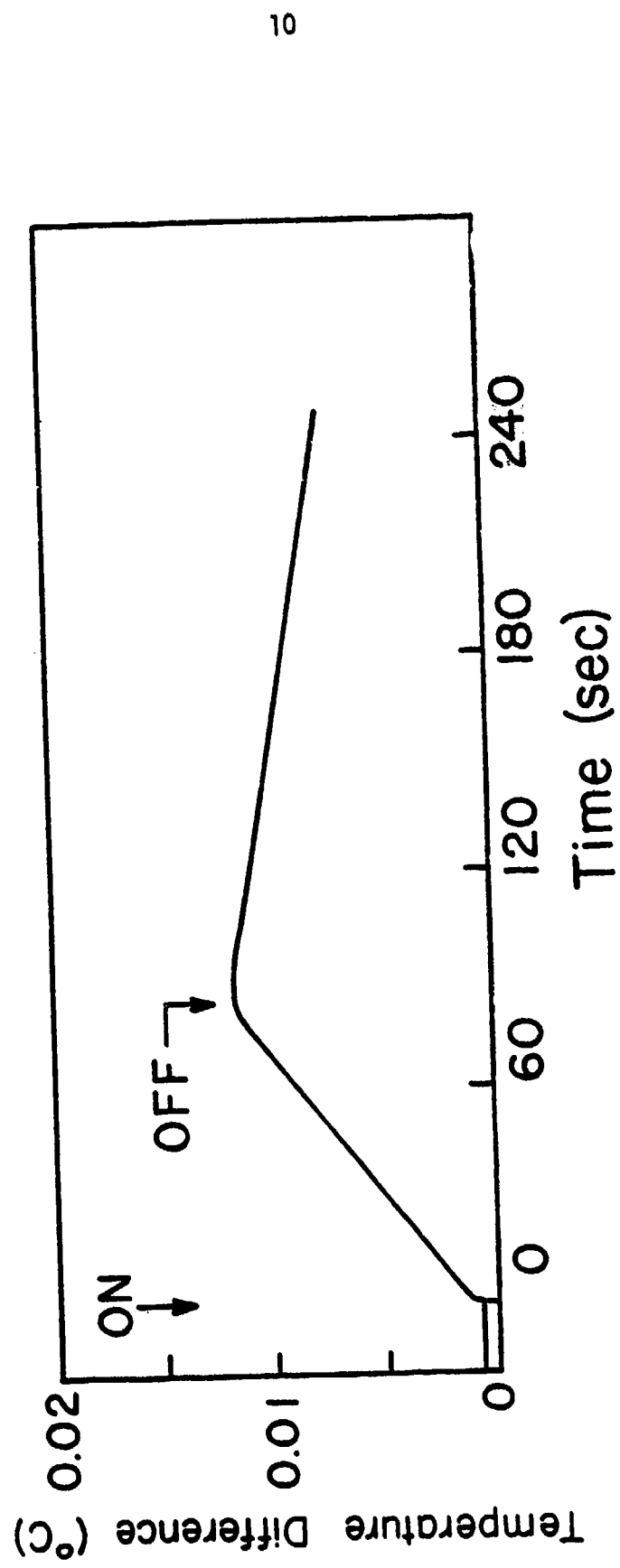


Figure II-1. Schematic diagram of laser calorimetry experiment.

Figure II-2. Typical experimental laser calorimetry data. Temperature is plotted vs. time. The ON and OFF refer to the laser irradiation of the sample.



This is the basic formula used in laser calorimetry to determine bulk absorption coefficients. However, it should be noted that common processes such as scattered laser radiation and surface absorption are ignored in this treatment. These processes will be treated in more detail later.

For accurate calorimetric results the sample should be isolated from its surroundings as much as possible. This is achieved by mounting the sample in a calorimeter (a box which minimizes room convection currents and thermal fluctuations). Calorimeters vary greatly in size, shape and complexity. However for extremely sensitive measurements a vacuum calorimeter is the most appropriate. Figure II-3 shows a schematic diagram of the vacuum laser calorimeter used in our measurements. The sample is suspended on nylon threads in the center of the calorimeter. A shielded reference sample is mounted on four nylon screws in the corner of the calorimeter. One junction of a differential thermocouple (either copper vs. constantan, $\frac{dE}{dt} \sim 41 \mu\text{V}/\text{K}$ at room temperature or iron vs. constantan, $\frac{dE}{dt} \sim 52 \mu\text{V}/\text{K}$ at room temperature) is attached to the sample by either a nylon thread or by spring loading. A dab of silicon grease establishes good thermal contact between the sample and the thermocouple. The other thermocouple junction is attached to a reference crystal and the wires from the two junctions are directed out of the calorimeter through a vacuum feedthrough. Scattered radiation from the vacuum windows is minimized by mounting polished salt windows at Brewster's angle on tubes leading into the vacuum chamber. The long narrow tubes are blackened to absorb any scattered radiation from the windows. Further isolation of the sample from scattered light is provided by irises between the sample and the windows and focusing lens. The walls of the calorimeter are blackened

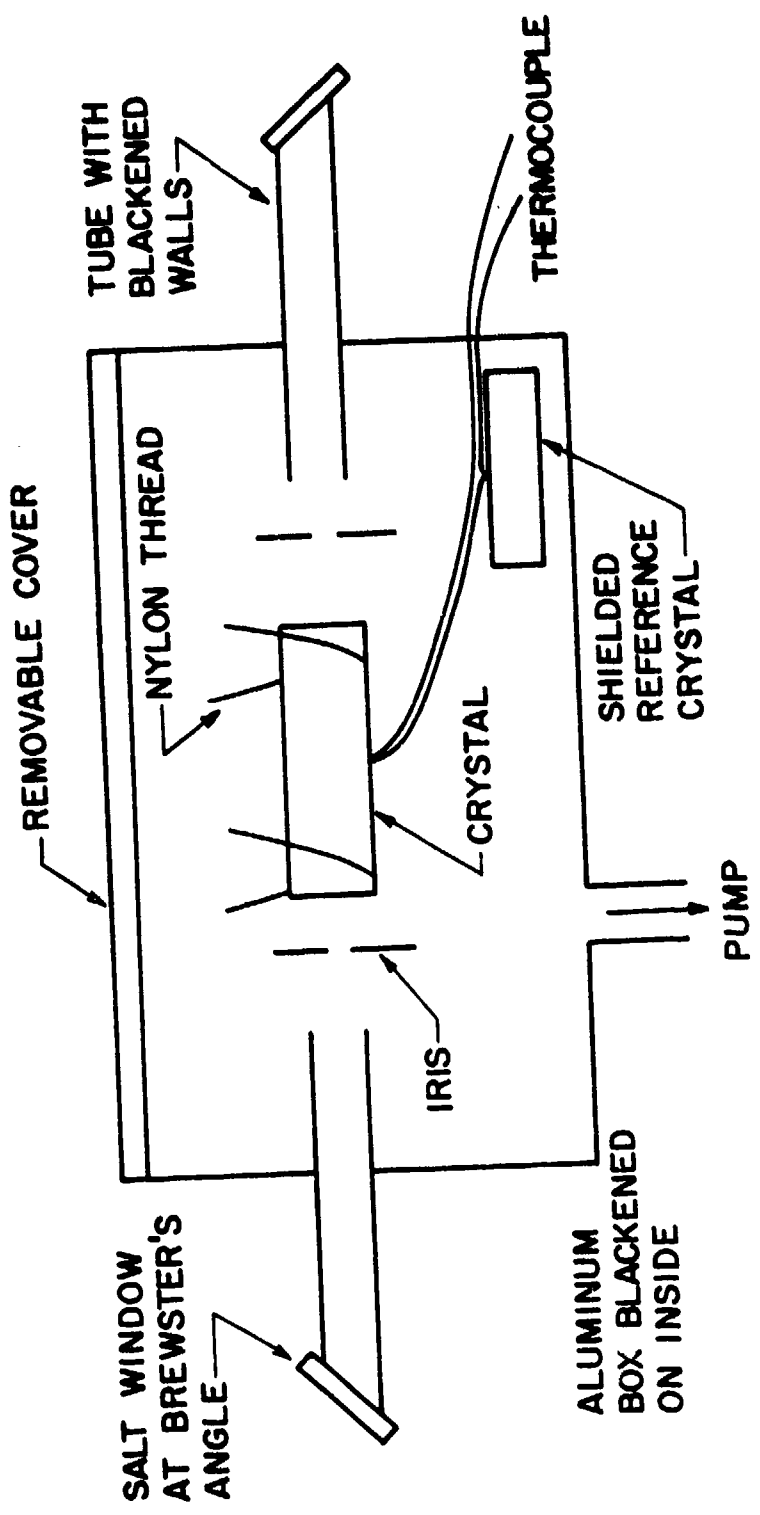


Figure II-3. Schematic diagram of room temperature vacuum calorimeter. and blackened light pipes decrease stray radiation.

Brewster windows

to suppress any stray radiation within the vacuum chamber. Typically a vacuum of better than .1 torr is maintained during measurements.

The experimental arrangement described above is sufficient to measure temperature slopes (i.e. $\frac{dT}{dt}$) of about 10^{-6} K/sec. For typical laser powers this sets the minimum detectable $\alpha \sim 10^{-6} \text{ cm}^{-1}$. This is considerably lower than any of the absorption coefficients measured thus far in our laboratory.

As mentioned previously there are two processes that can significantly affect calorimetric data. One of these is laser radiation scattered directly to the thermocouple (the scattering can occur from the sample itself or from optical components in the system). Such direct scattering of laser light to the thermocouple is accompanied by an anomalously fast temperature rise when the laser is turned on followed by an equally sudden drop in temperature when the laser is turned off³³ (see Figure II-4). If the scattering originates outside the sample then it is assumed that the scattering contribution to the thermal rise and decay is constant, i.e. a dc level shift, and the slopes are unaffected. However, if the scattering is produced at the sample surface or in the sample bulk, some of the scattered radiation will be trapped and absorbed in the sample. This will no longer produce merely a dc level shift but will change the slopes and hence the measured absorption coefficient (see Figure II-5). Because of this non-negligible effect of scattered laser radiation on measured values of α there is great emphasis placed on minimizing scattering by means of irises, absorbing calorimeter walls, etc.

The second problem that is becoming more prevalent is surface

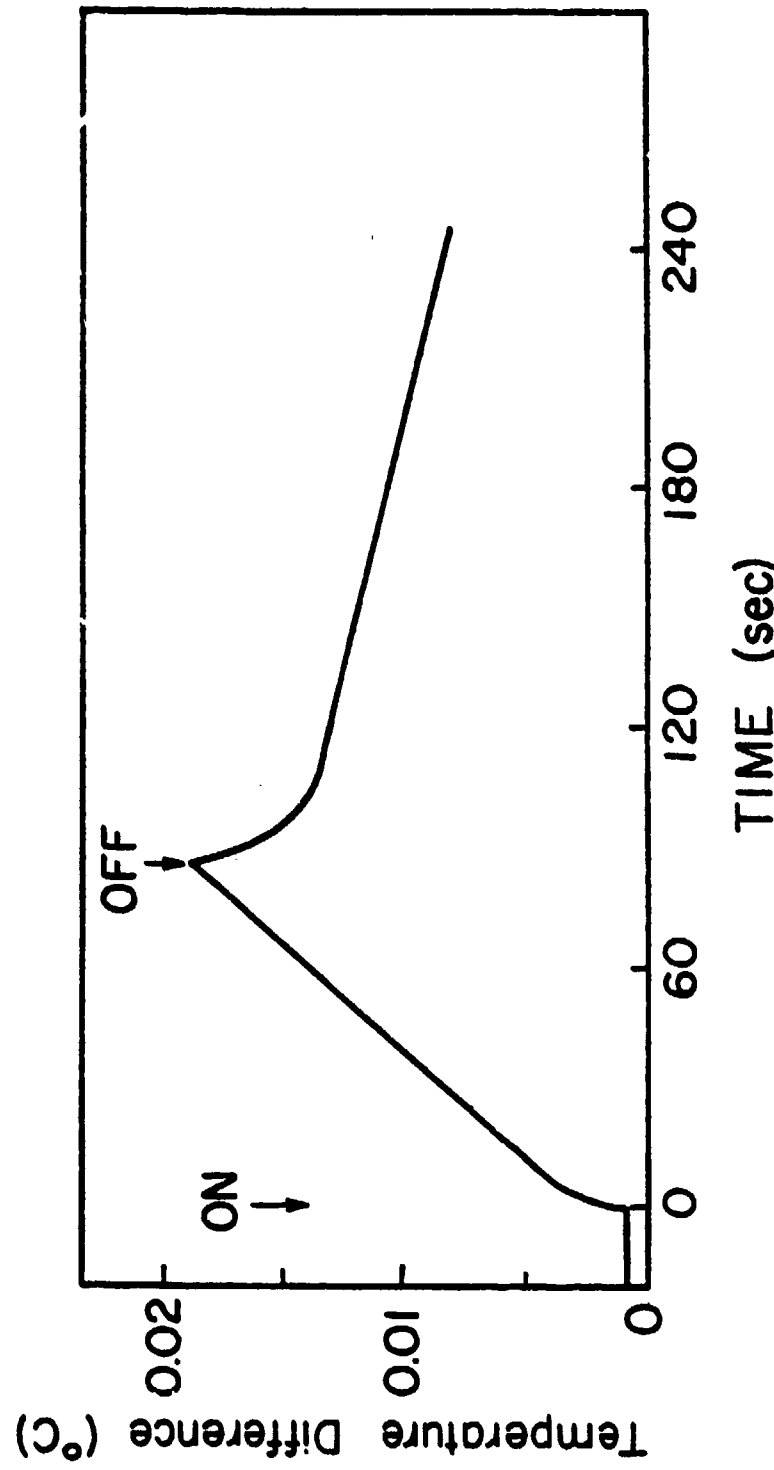


Figure II-4. Calorimetric data with some direct scattering of laser radiation to the thermocouple. Note the sudden rise in temperature when laser is turned on and sudden drop in temperature when laser is turned off.

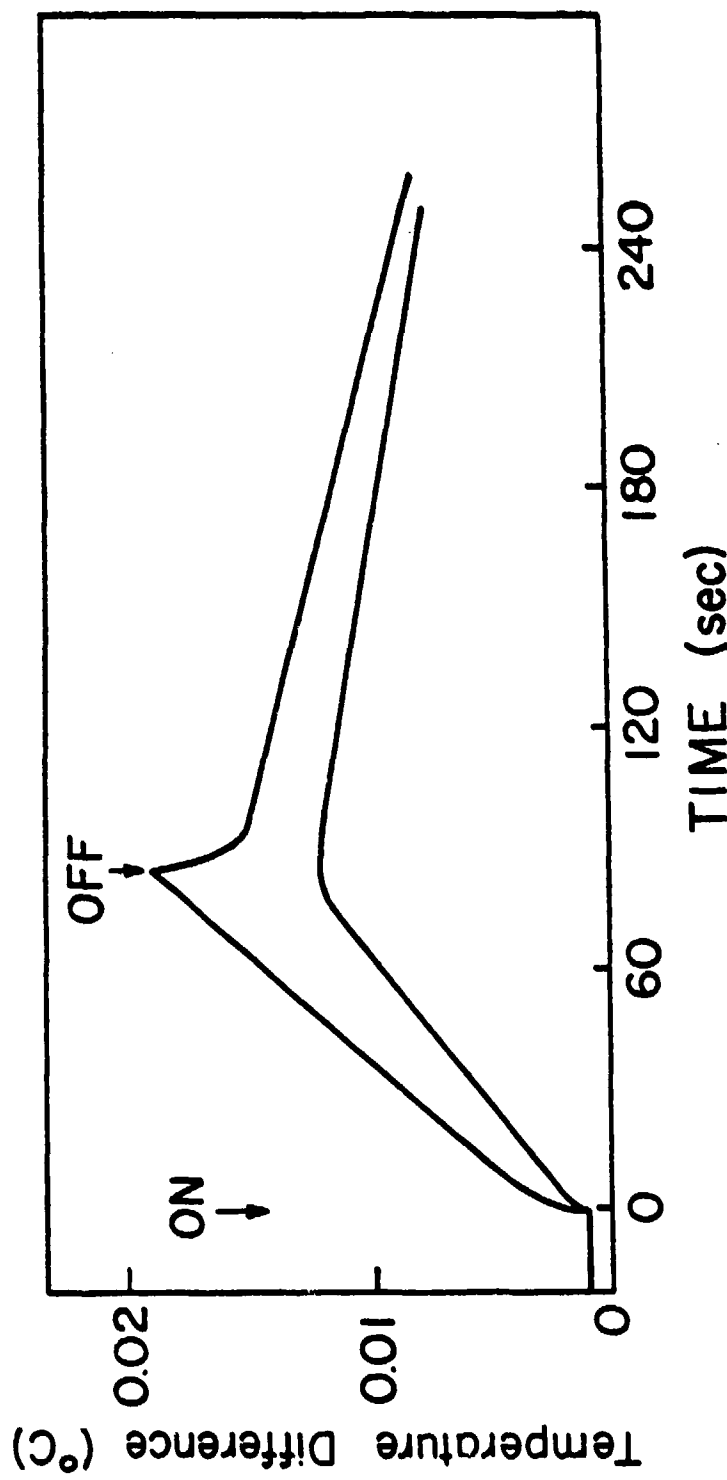


Figure II-5. Two temperature v.s. time calorimetric curves. A sample with no scattering at the faces or in the bulk produces the lower curve. The same sample with some scattering on one of the end faces produces the upper curve. Not only are there cusps indicating scattering but the heating slope increases due to scattered radiation trapped and absorbed in the sample.

absorption. Improved purification techniques have lowered bulk absorption coefficients of many materials to very low levels and therefore surface absorptions become important or even dominant absorption mechanism in some crystals. There are two ways to calorimetrically distinguish between bulk and surface absorptions but both techniques have drawbacks that make them somewhat less than satisfactory.

The first technique involves making calorimetric absorption measurements as a function of sample length.¹³ One assumes that

$\alpha_{\text{total}} L = \alpha_{\text{bulk}} + 2\sigma$ where σ is the surface loss. A plot of $\alpha_{\text{total}} L$ vs. L will be a straight line with slope α_{bulk} and intercept (extrapolating to $L = 0$) equal to 2σ . Figure II-6 shows two plots of absorbed power vs. sample length. In Figure II-6a the extrapolated line passes through the origin indicating no surface absorption. Figure II-6b shows a sample with a surface absorption of 2×10^{-3} per surface. There are two drawbacks to this technique. First of all, a great deal of time is required to repeat the measurements for a number of different sample lengths. Secondly, there is no guarantee that for every sample length the surface will be prepared identically. This will give rise to surfaces of differing absorption and scattering properties.

A second technique developed by Hass *et al.*³² separates bulk absorption from surface absorption by exploiting the low thermal conductivity of insulators (in particular, alkali halides). By using a long sample ($\gtrsim 7$ cm) with a thermocouple attached in the middle portion of the long dimension the thermal diffusion from absorbing end faces will arrive at the thermocouple later than the thermal diffusion from the bulk of the sample. The heating curve will then consist of two parts (see Figure II-7).

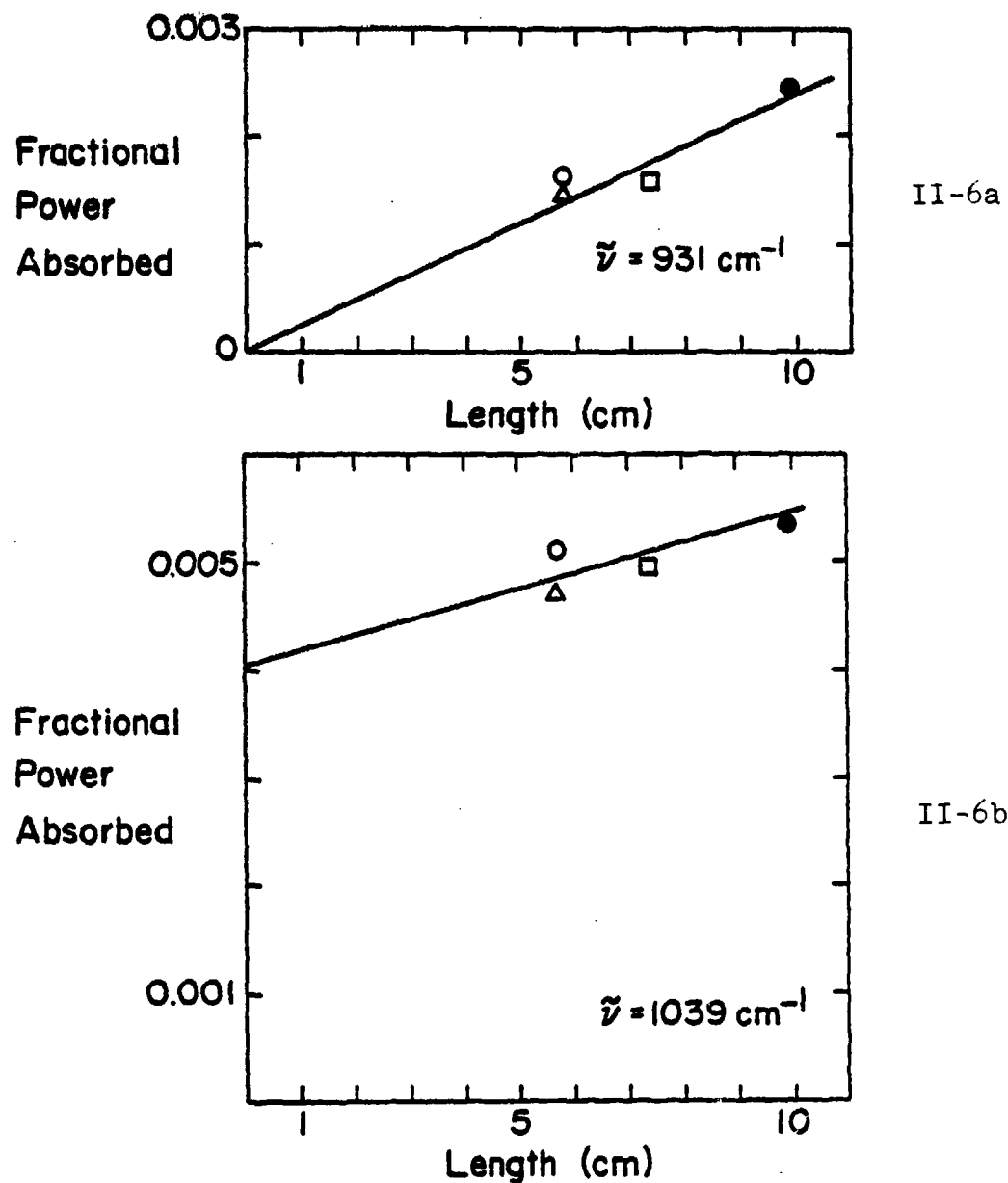


Figure II-6. a) Fractional power absorbed as a function of length. The slope of the straight line is equal to the bulk absorption coefficient ($\alpha = 2.4 \times 10^{-4} \text{ cm}^{-1}$). The intercept at the origin indicates no surface absorption.
 b) Fractional power absorbed as a function of length. The slope corresponds to a bulk absorption of $1.5 \times 10^{-4} \text{ cm}^{-1}$. The intercept corresponds to $2\sigma = .004$ or a surface loss of $2 \times 10^{-3}/\text{surface}$.

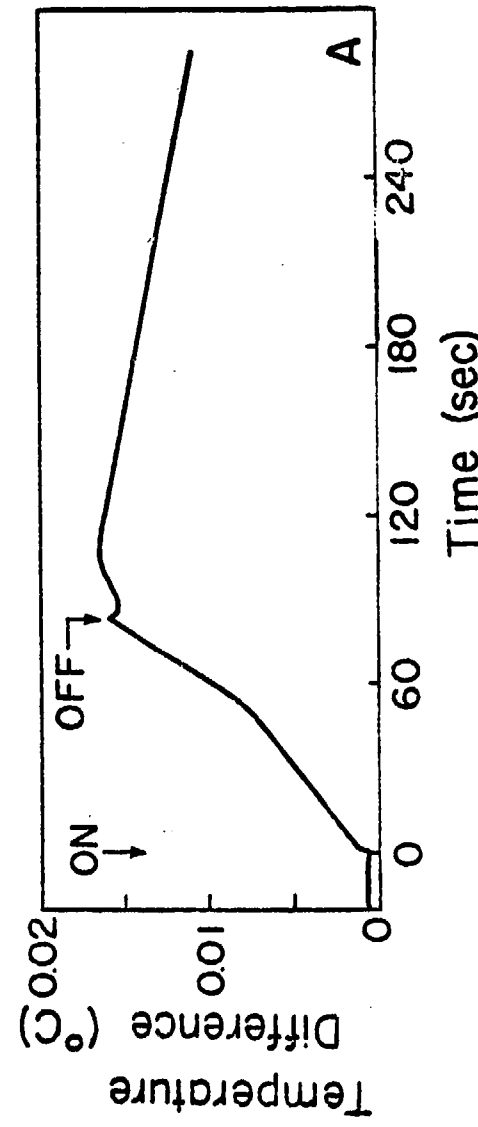


Figure 11-7. Sample temperature vs. time curve for "long-rod"-geometry sample with finite surface absorption. The initial slope of the heating curve corresponds to the bulk absorption. About 60 sec later heating due to the surface "arrives" at the thermocouple increasing the slope of the heating curve.

The initial slope will be due to bulk heating. At some later time*
 $(t \sim (\frac{L}{2})^2 / 6K)$ where L = sample length, K = thermal diffusivity of sample
the heat from the end faces will arrive at the thermocouple and the slope
of the heating curve will increase. However, to compute the surface loss
the heat transfer coefficient must also be determined and three-dimensional
heat flow equations must be solved. This involves measurements using
multiple thermocouples to measure sample temperatures at a number of
different point on the crystal.

In summary, the multiple-length technique suffers from the numerous
presumably non-identical surface preparations on the sample as the length
is changed. On the other hand, the measurements and calculations are
quite straightforward. In the "long-rod" technique the measurements and
the calculations are more complex but only one sample needs to be measured
and there is no longer any problem with non-identical surface preparations.

C. CO₂ Laser: Modified Apollo cw Laser

The laser source used for the calorimetry experiments is a modified
Apollo 550 tunable CO₂ laser. This section describes the construction and
cw and quasi-cw characteristics of this laser. The theory behind the CO₂
laser is briefly described in Appendix I.

1. Construction

An Apollo 550 CO₂ laser was extensively modified to provide line
tunable cw, pulsed-current, Q-switched and pulsed-discharge Q-switched
output. In addition, the output mirror was mounted on piezoelectric
translator (PZT) to provide approximately 100 MHz of tunability on each

*For example, this time for a 10 cm KCl crystal is about 80 sec.

line. A schematic diagram of the modified cw laser is shown in Figure II-8 and Table II-2 lists the specifications of the laser. Premixed gas 18% N₂, 6% CO₂, 76% He at ~20 torr enters the laser tube in the middle and is removed by larger pump lines at both ends of the tube. The discharge passes between the pin anode at the middle of the tube and two cylindrical cathodes mounted concentrically with the laser tube one on each end. Two adjustable ZnSe windows mounted on bellows at Brewster's angle complete the laser tube. The optical cavity is completed at one end by one of two gratings. The first is a 75 line/mm, 10.6 μm blaze angle grating. The second is a 120 line/mm, 9.6 μm blaze angle grating. The 120 line/mm grating provides higher resolution as well as provides cw laser output on P and R branches of both the (00⁰1-10⁰0) and (00⁰1-02⁰0) bands. The 75 line/mm grating does not provide cw laser output on the R branch of the (00⁰1-02⁰0) band. All the operating characteristics of the CO₂ laser presented henceforth were measured with the 120 line/mm grating. At the other end of the optical cavity is a 5-meter radius of curvature coated Ge mirror whose transmission curve in the 10 μm region is shown in Figure II-9. The output mirror is mounted on a Lansing model 21.937 piezoelectric translator. Application of 0-1600 V to the PZT translates the mirror 0-16.4 μm with a linearity of about 5%. A Lansing model 80.214 lock-in stabilizer provides a variety of voltage ramps and modulations for this PZT. In addition, frequency stabilization of the CO₂ laser can be achieved by means of the lock-in stabilizer.³³ The laser tube, ZnSe windows and grating are water cooled and the output mirror, grating, and laser tube are all mounted on a granite slab for cavity length stability.

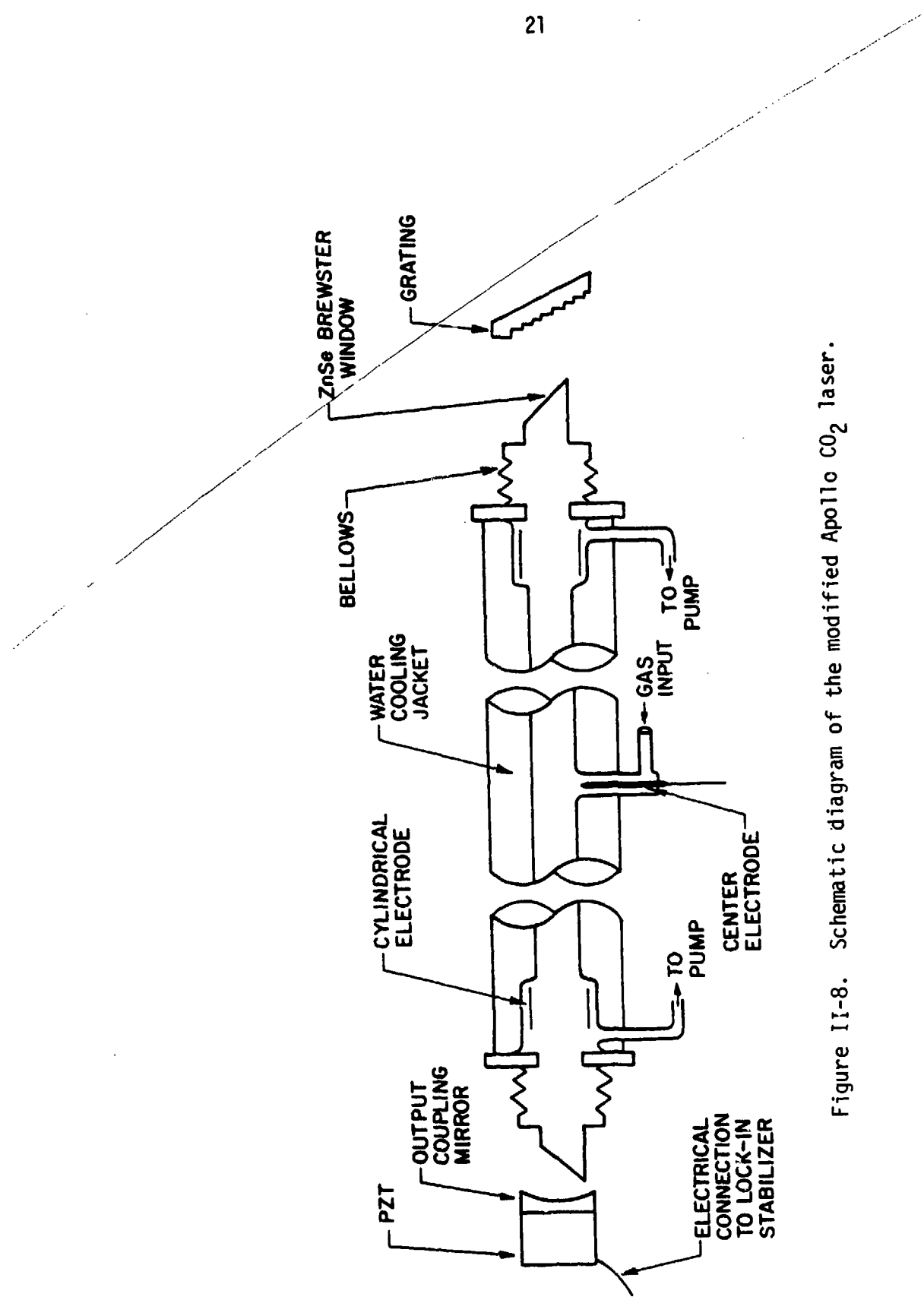


Figure II-8. Schematic diagram of the modified Apollo CO₂ laser.

Table II-2

Specifications of Modified Apollo CO₂ Laser

| | |
|--|--------------------------------|
| Active Length | $L_A = 112 \text{ cm}$ |
| Total Cavity Length | $L_C = 167 \text{ cm}$ |
| Bore Diameter | $D_T = 6 \text{ mm}$ |
| Radius of Curvature of Output Mirror | $R = 5 \text{ m}$ |
| Transmission of Output Mirror | See Figure II-9 |
| g-factor: $1 - L_C/R$ | $g = .67$ |
| Fresnel Number: $D_T^2/4 L_C$ | $N = .51-.56$ |
| TEM ₀₀ Output Beam Diameter | $d = 6 \text{ mm}$ |
| Beam Divergence (full angle) | $\theta \sim 2.2 \text{ mrad}$ |
| Beam Waist Diameter | $d_w = 5.4 \text{ mm}$ |

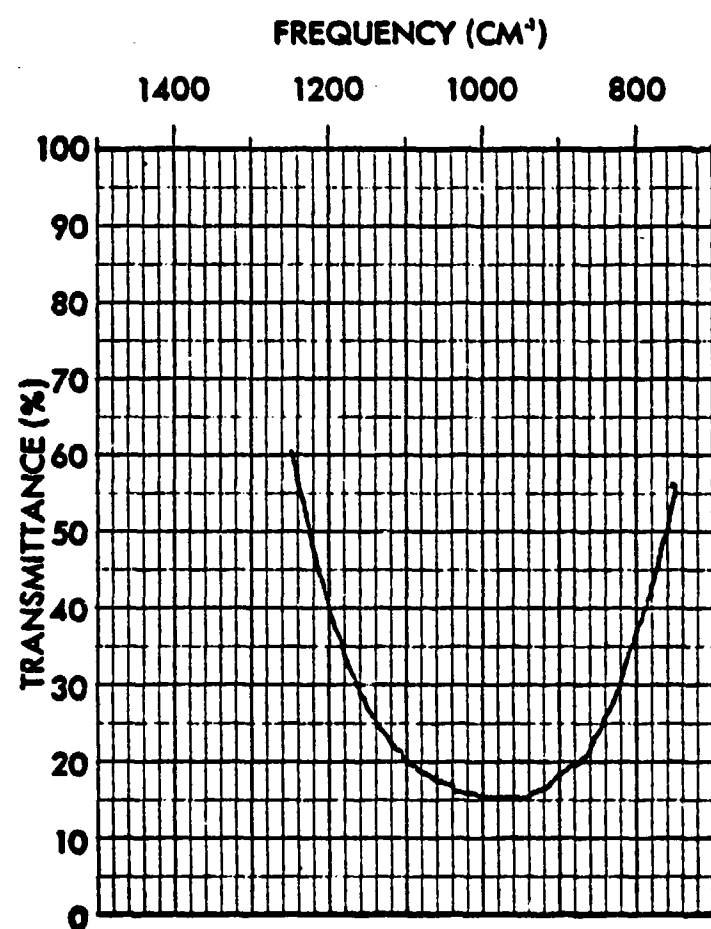


Figure II-9. Transmission vs. frequency of output coupling mirror on the Apollo laser.

One additional important feature of the laser is the external (to the power supply) control over the discharge provided by the EXT ON-OFF connector on the laser power supply. A +12 V signal applied to this connector turns the discharge off. This feature facilitates control of pulse widths, dead times, etc., by means of an external pulse generator. The importance of this feature will be more obvious later in the thesis.

2. CW and Pulsed Optical Characteristics

The modified Apollo laser is a line tunable TEM_{00q} single frequency laser. Figures II-10 to II-12 show the power outputs of the modified laser in the cw, chopped (10% duty cycle), and pulsed (1% duty cycle) modes of operation respectively. Seventy-two lines lase in cw operation with 52 lines stronger than 10 W. The strongest line has a power output of 27.5 W. In chopped-current operation lasing occurs on 97 lines with 91 lines having peak powers greater than 10 W. The strongest line has peak power output of 73 W. Pulsed-current operation has 90 lasing lines of which 75 have peak powers greater than 50 W. The P(20) line has a pulsed output peak power of about 170 W. It is evident that the efficiency and output power of the laser are greatly enhanced when operated in the chopped or pulsed modes. This effect is discussed in Appendix I. The additional lasing lines in chopped and pulsed operation are also noteworthy.

A photograph of the output pulse shape in the chopped mode is shown in Figure II-13. The relative heights of the main peak and the trailing shoulder can be varied by changing the discharge current. At lower currents the main peak becomes weaker and has a slower rise time. At higher currents

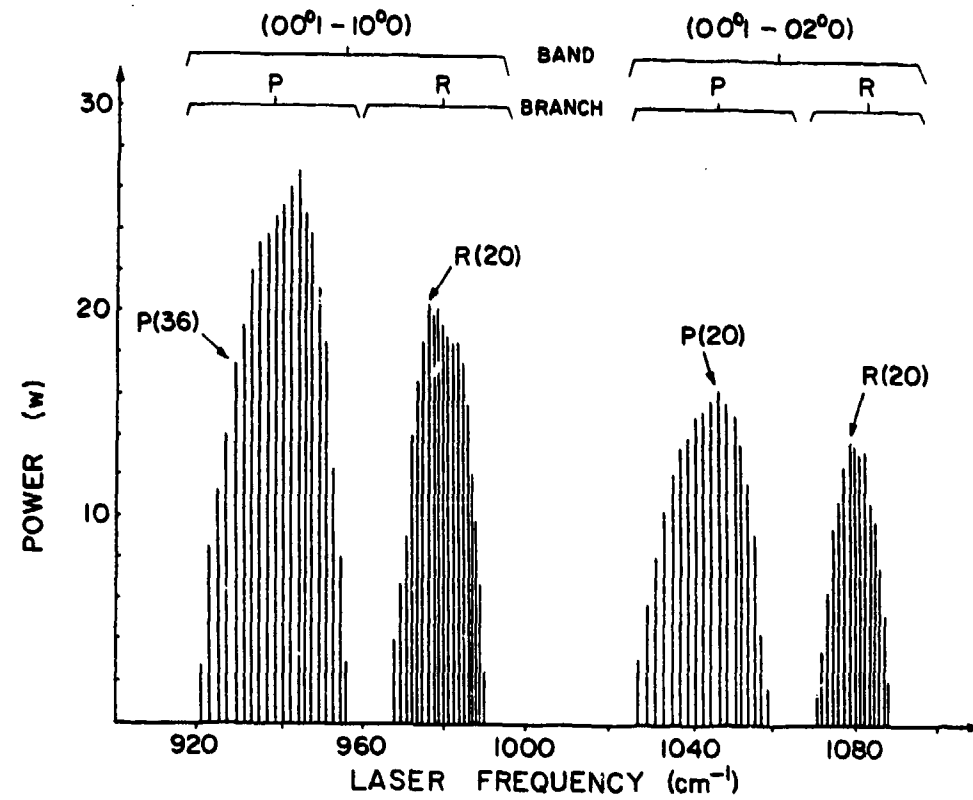


Figure II-10. Maximum cw output power of modified Apollo laser for the various CO_2 laser lines. One line in each branch is identified for reference.

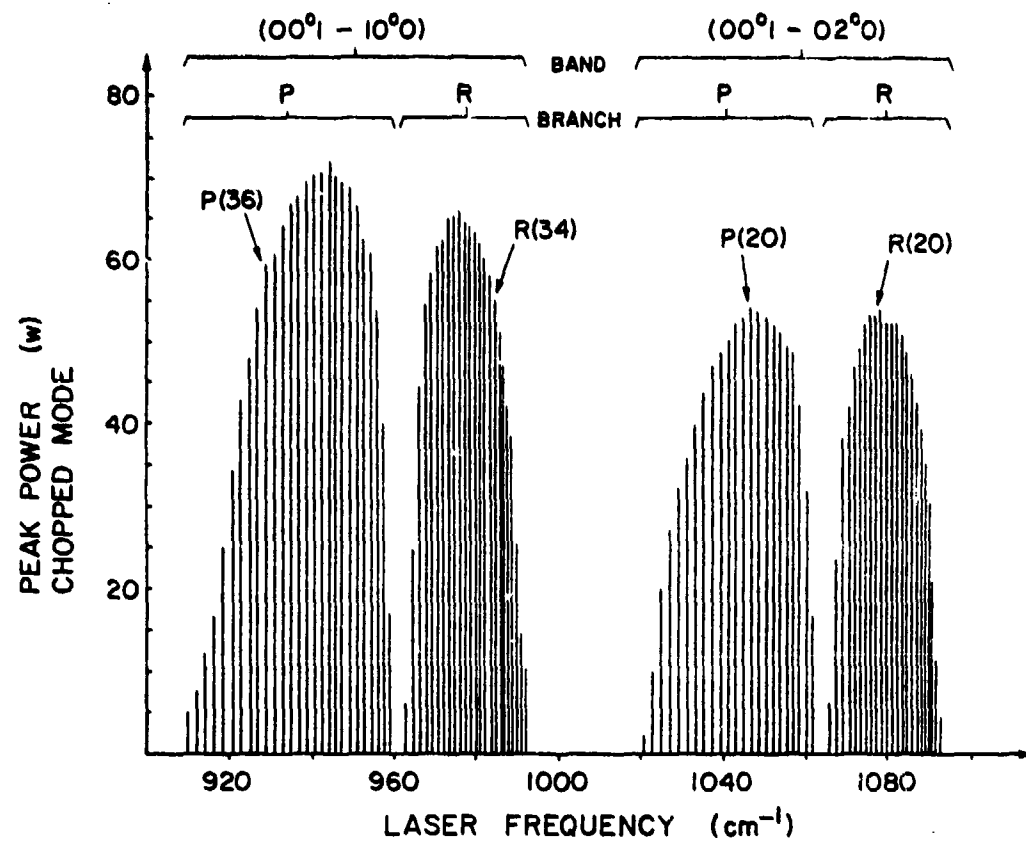


Figure II-11. Maximum output peak power of modified Apollo laser operating in the chopped mode (10% duty cycle). One line in each branch is identified for reference.

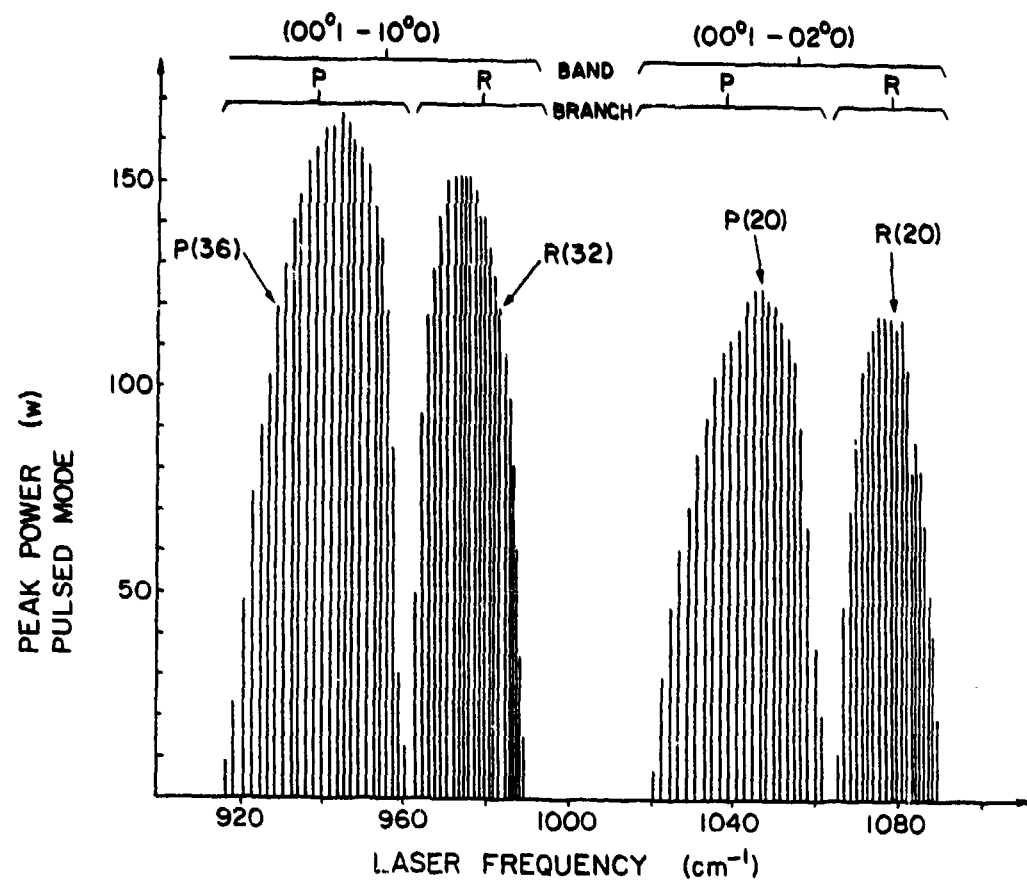


Figure II-12. Maximum output peak power of modified Apollo laser operating in the pulsed mode (1% duty cycle). One line in each branch is identified for reference.

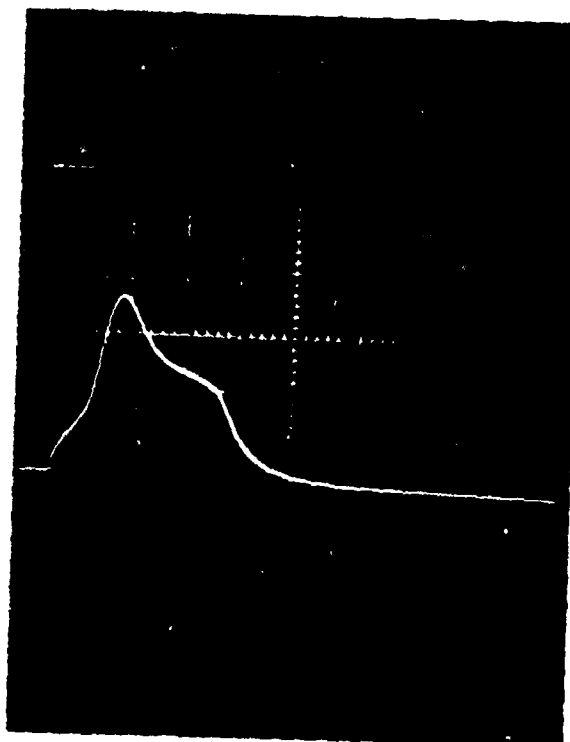


Figure II-13. Photograph of CO₂ pulse from the modified Apollo laser operating in the chopped mode (.2 msec/div).

the ratio of the peak to shoulder heights is ~2 to 1. Figure II-14 shows a photograph of the output pulse when the laser is operated in the pulsed mode. The pulse shape is much more uniform than the chopped-mode pulses.

D. Sample Preparation

Complete descriptions of the growth, purification and preparation of alkali halide crystals are given in references 34-36 and only a brief summary will be given in this section.

Two crystal growing techniques were used, the Czochralski seed-pulling method which was by far the most common, and the Bridgeman technique. Crystals oriented along [111] direction were produced by both techniques while [100]-oriented crystals were grown using the Czochralski technique. Both types of growths produced 7-10 cm-long crystals; the Czochralski-grown crystals had an approximately square cross section about 1.5 cm on a side while the Bridgeman crystals had circular cross sections 1.8 cm in diameter. Some crystals grown by the Czochralski method were doubly grown. After the first pull was completed the crystal was remelted in a new crucible and another crystal was grown from this melt. The details of this growth technique are found in reference 34.

The starting material for the KBr crystals is Merck Suprapur KBr with impurity levels as listed in reference 34. This starting material was often purified before the crystals were grown.³⁴ The most common purification method consists of melting the salt and bubbling a reactive gas, e.g. Br₂, CCl₄, etc., through the molten salt. The material is then cooled and transferred to the crystal growing furnaces.

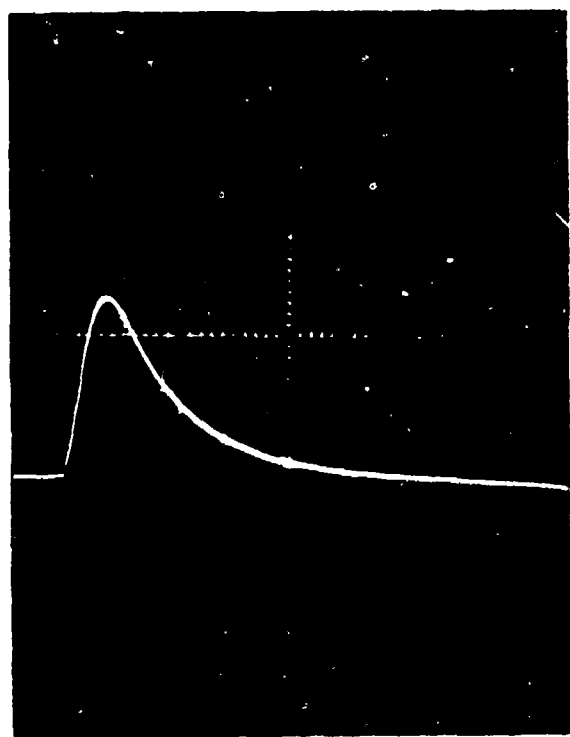


Figure II-14. Photograph of CO_2 pulse from the modified Apollo laser operating in the pulsed mode (.05 msec/div).

The surfaces of the samples used in the calorimetry experiments were either cleaved or polished. The polishing procedure is as follows. The ends of the crystal are removed by cleaving or stringsawing. The ends are then polished using a South Bay Technology Model 151 Crystal Facing Instrument³⁵ and a solvent of Fisher Absolute Methanol. After achieving a satisfactory surface finish the crystal is rinsed in anhydrous ether and then dried. The final surface finish usually had an orange-peel appearance and on occasion was milky rather than transparent. The cause of this milkiness is not known and repolishing seemed to be the only way to improve the surface finish. The effects of the orange-peel surface is not known but our results indicate that cleaved surfaces are much better than the polished one as far as scattering and surface absorption are concerned.

E. Results

The absorption coefficient as a function of frequency ($930-1050\text{ cm}^{-1}$) was measured calorimetrically for all the crystals purified and grown in the variety of ways mentioned in the previous section. Table II-3 summarizes the various results. Not all crystals that were measured are included in this table because many crystals prepared in the same way yielded similar results and therefore are omitted from this listing. The first column lists the crystal by number. The second column gives a brief description of purification techniques and surface preparation. The third and fourth columns list the minimum and maximum bulk absorption coefficients measured for each crystal between 930 cm^{-1} and 1050 cm^{-1} . The fifth and sixth columns list the minimum and maximum surface absorption coefficient

Table II-3
Summary of Absorption Coefficient Measurements

This table summarizes the results of calorimetric measurements made on a variety of alkali halides. Unless otherwise noted, the crystals are KBr crystals grown by the Czochralski method oriented along the [100] direction.

| Crystal Number | Purification; surface preparation | Minimum _o bulk (cm ⁻¹) ^x 10 ⁴ | Maximum _o bulk (cm ⁻¹) ^x 10 ⁴ | Minimum of surface (per surface) ^x 10 ⁴ | Maximum of surface (per surface) ^x 10 ⁴ |
|----------------|---|--|--|---|---|
| 7512102W | Cleaved surfaces | 2 | 13 | | |
| 7512102W | Surfaces mechanically smoothed | 1.6 | 8 | | |
| 751230W | Cleaved surfaces | 2.6 | 6 | | |
| 75123C2W | Surfaces etched in H ₂ O-alcohol solution | 3.1 | 9.2 | | |
| 7512311W | Cleaved surfaces | 2.3 | 8 | | |
| 7601062W | Double growth | 19 | 38 | | |
| 7510312W | Double growth | 22 | 36 | | |
| 7601164W | Br ₂ -treated starting material | 1 | 5.6 | | |
| 7604202W | CCl ₄ treated powder; cleaved surfaces | 4.2 | 10.6 | 1 | 22 |
| 7604202W | CCl ₄ treated powder; polished faces | 4.2 | 12 | 5 | 18 |
| 7603102W | Slow growth, Br ₂ treated melt; cleaved faces | 1.2 | 4.6 | -- | -- |
| 7603102W | Slow growth, Br ₂ treated melt; polished faces | 1.5 | 4.3 | 3 | 6 |

Table II-3 (continued)

| | | | | | |
|-----------------------------|--|-----|-----|----|-----|
| 7601302W | Double growth from left over melt; cleaved faces | 7.2 | 23 | -- | -- |
| 7601276W | +100 ppm CaBr ₂ ; cleaved faces | 4.9 | 6.5 | 21 | 30 |
| 7602122W | Br ₂ treated starting material cleaved surfaces | 3.8 | 7.8 | 5 | 8.7 |
| 7602032W | Double growth; polished faces | 4.3 | 7.3 | 17 | 70 |
| 7704262W | [111]-orientation; string-sawed; polished | 3.5 | 5 | 0 | |
| 7704261W | [100]-orientation; string-sawed; polished | 38 | 50 | | |
| 770428 Br-Au | Bridgman growth; [111]- orientation; string- sawed, polished | 1 | 1.6 | | |
| 7705052W | [111]-orientation; string-sawed; polished | 3.7 | 8 | | |
| 7705031W | [100]-orientation; string-sawed; polished | 2.5 | 9.9 | | |
| <u>Other Alkali Halides</u> | | | | | |
| KI 7603171W | Cleaved faces | 3.6 | 6 | -- | -- |
| RbCl 7601234W | Cleaved faces | 5 | 15 | | |

for each crystal. No entry in these columns indicates no available data.

Although many different types of purification and growth techniques were tried for KBr the end results were remarkably similar. Although there were large variations in the magnitude of the absorption coefficients, the shape of α vs. frequency plots was for the most part the same. A typical plot of α vs. frequency is shown in Figure II-15. The absorption coefficient increases with increasing frequency to a maximum value around 1030 cm^{-1} and then appears to decrease around 1050 cm^{-1} . This behavior is anomalous in that it does not agree with existing theories^{5,37-39} of intrinsic multiphonon absorption which predict absorption coefficients that decrease exponentially with increasing frequency. This behavior in KBr is probably not an artifact of our crystal growing and preparation techniques because an almost identical behavior was observed in KCl by Hass et al.⁶ The similarity between our KBr data superposed on Hass' KCl data (Figure II-16) is quite remarkable. At this stage the similarity in absorption coefficients must be considered coincidental but some evidence which suggests the contrary will be presented later.

One possible source of this anomalous absorption rise at higher frequency could be scattering from microscopic bubbles or defects in the samples. In order to rule out scattering which presumably exhibits $(1/\lambda)^4$ power law frequency dependence, an absorption measurement was made using a CO laser ($\sim 5.3\text{ }\mu\text{m}$). If in fact there was scattering present, the CO measurement should yield a larger value for the absorption coefficient. The result of the measurement is shown in Figure II-17. The absorption coefficient at 1896 cm^{-1} is $1.3 \times 10^{-4}\text{ cm}^{-1}$ indicating that the cause of the

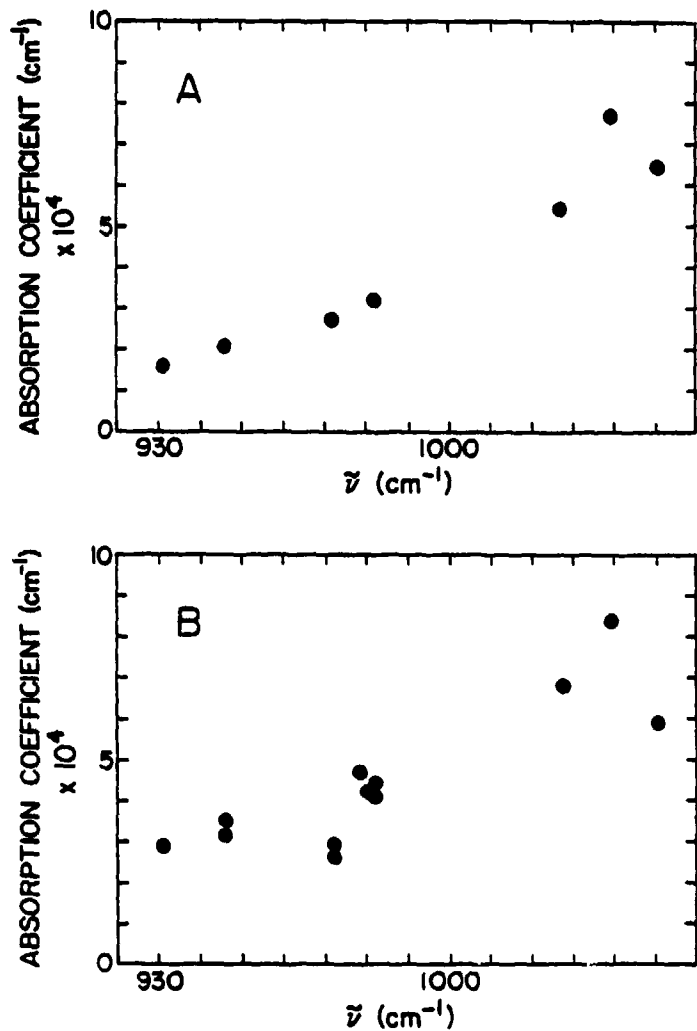


Figure II-15a,b. Absorption coefficient vs. frequency for two different KBr crystals. Although the magnitude of α changes from crystal to crystal the overall shape is the same. Note the absorption resonance near 1030 cm^{-1} . The clusters of points in Figure 15b represent multiple measurements at the particular frequency and give a good indication of the reproducibility of the calorimetric measurements.

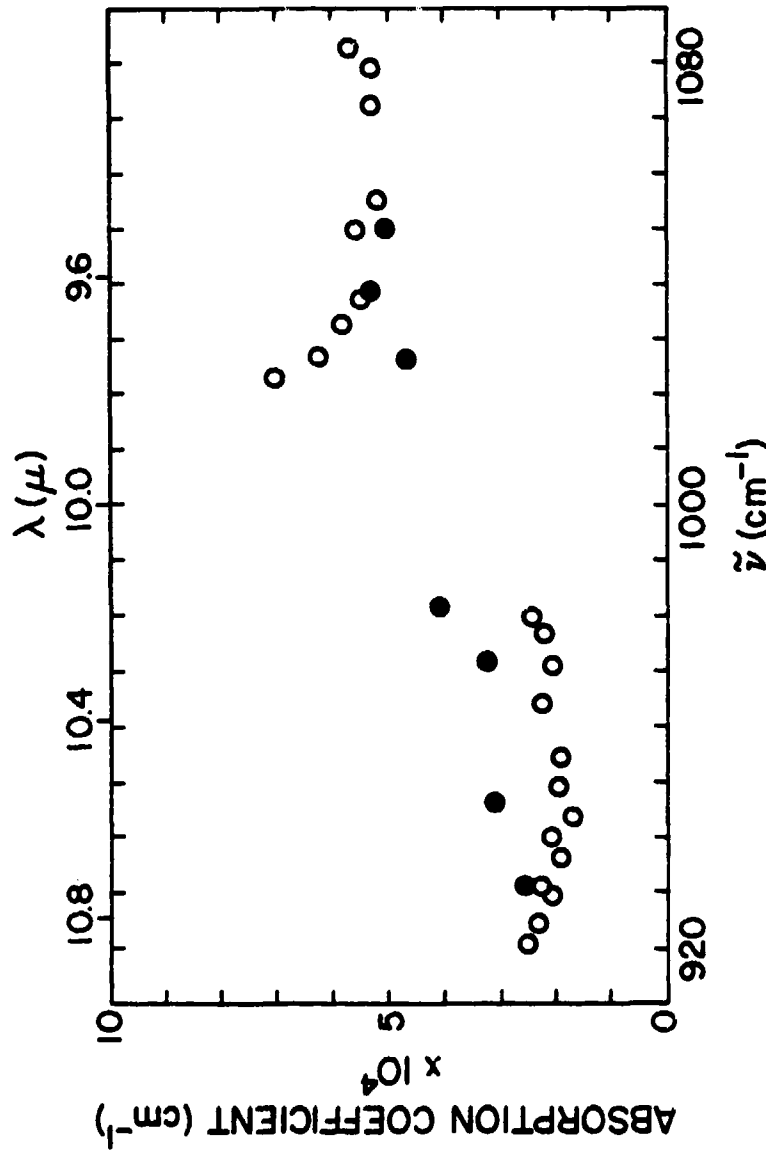


Figure 11-16. Absorption coefficient vs. frequency near $10\ \mu m$ for $10.8\ cm$ KCl crystal measured by Hass et al.⁶ (open circles) and for $9.9\ cm$ KBr crystal No. 7512302W (solid circles). Both crystals exhibit similar frequency dependences.

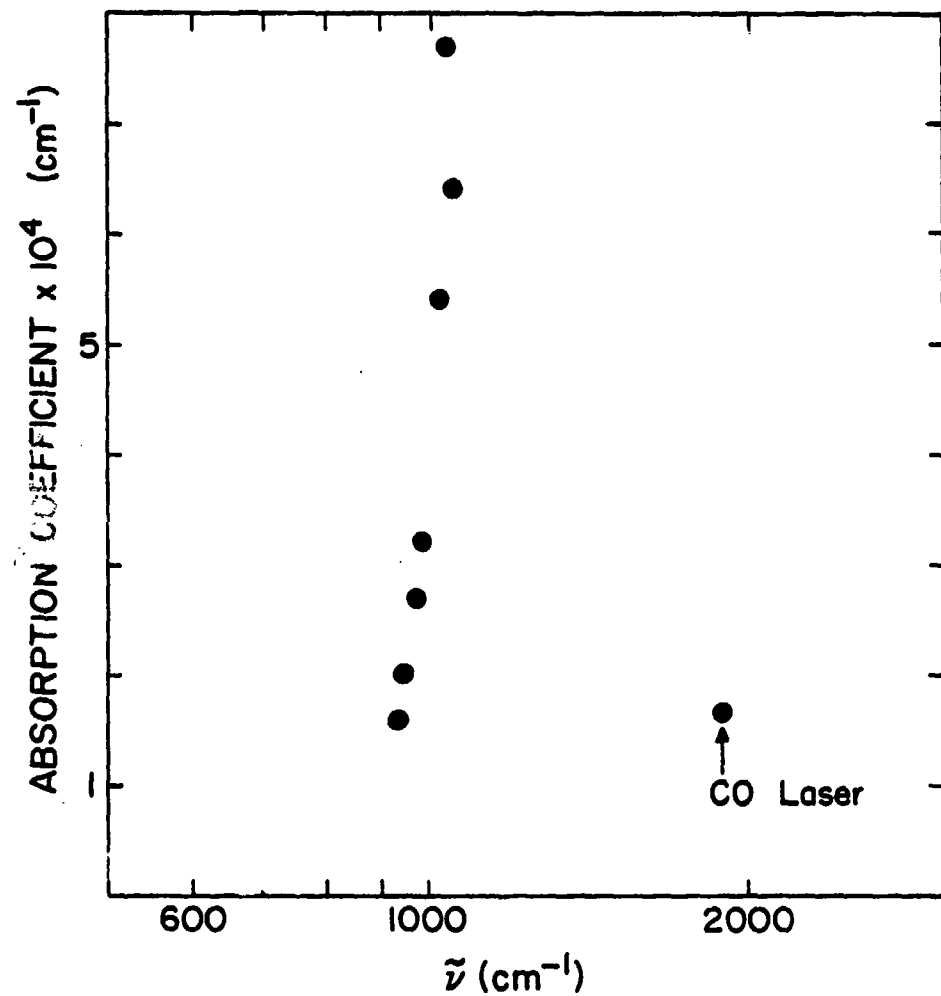


Figure II-17. Absorption coefficient vs. log frequency of crystal No. 7512102W (5.5 cm optical length) showing the absorption at 1896 cm $^{-1}$ measured with a CO laser.

frequency dependence of the absorption near $10 \mu\text{m}$ is presumably some type of resonance absorption rather than a scattering mechanism.

The nature (i.e., bulk vs. surface) of the absorption resonance near $9.8 \mu\text{m}$ was determined by length-dependent measurements of fractional power absorbed as discussed previously. Typical results are shown in Figure II-18. The open circles represent surface absorption and the closed circles represent bulk absorption. However, the bulk absorption still fails to show any significant decrease with increasing frequency indicating that some impurity absorption still exists in the bulk. In fact, in most crystals the bulk absorption exhibits a small maximum at 1030 cm^{-1} . Similar results were obtained in Hass' KCl measurements.

The anomalous frequency dependence of the bulk and surface absorption coefficients encouraged us to try double grown crystals which would hopefully reduce the impurity content of the samples. This was not to be, however; the bulk absorption coefficients ranged between $4 \times 10^{-4} \text{ cm}^{-1}$ and $7 \times 10^{-4} \text{ cm}^{-1}$ with a small resonance near 1030 cm^{-1} . The surface absorption ranged from $3 \times 10^{-4}/\text{surface}$ to $12 \times 10^{-4}/\text{surface}$ with the maximum occurring at 1030 cm^{-1} . It was then thought that perhaps impurities segregated from the melt into the crystal leaving the leftover melt from the first growth exceptionally pure. This theory was tested by growing a crystal from leftover melt material. These crystals had bulk absorption coefficients ranging between $7 \times 10^{-4} \text{ cm}^{-1}$ and $23 \times 10^{-4} \text{ cm}^{-1}$. Surface absorption if any was masked by the large bulk absorption. It is quite puzzling that both doubly grown crystals and crystals grown from leftover melt material exhibit remarkably high absorption. The only difference is in the major

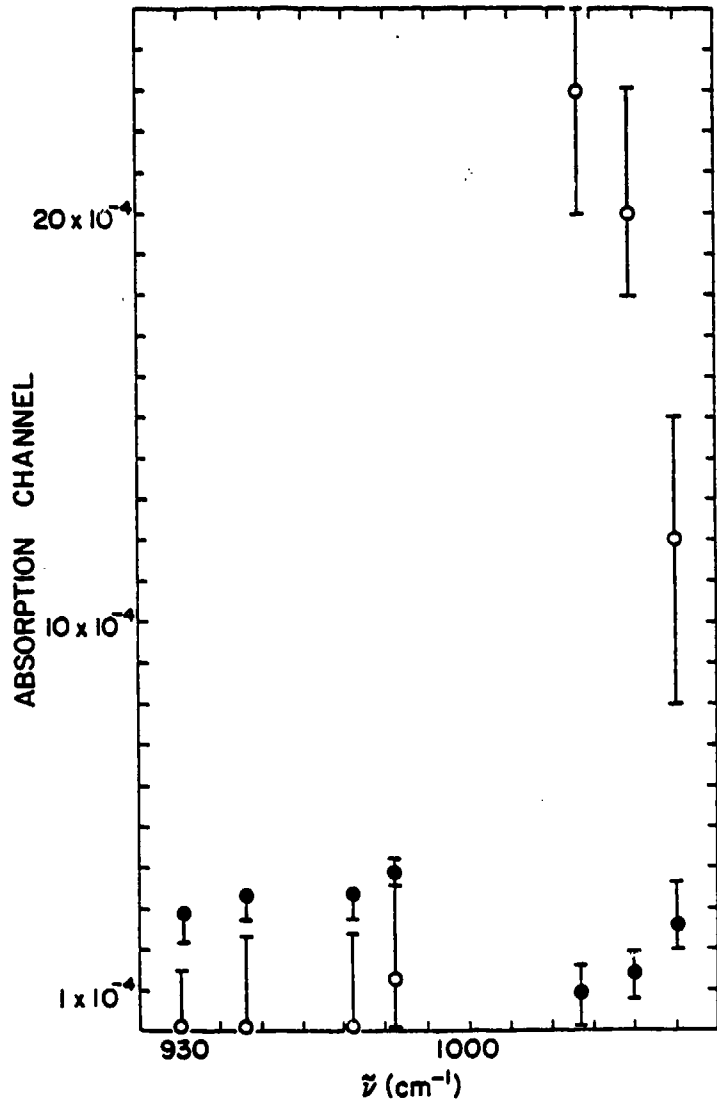


Figure II-18. Plot of absorption channel (i.e. bulk or surface) vs. frequency. Solid circles represent bulk absorption. Bars are not an indication of experimental error but rather the range of values that can be obtained depending on how the data are fitted.

source of the absorption, i.e. the absorption in the doubly grown sample is dominated by surface absorption whereas the "leftover melt" crystal absorption appears to be in the bulk. These results are left unexplained.

Reactive atmosphere processing of the starting material was tried in an attempt to remove some of the impurities from the KBr before growth of the crystals. The starting materials were treated with either CCl_4 or Br_2 in the procedure described in references 34 and 35. The crystals grown from Br_2 -treated material all had bulk absorption coefficients around $3-7 \times 10^{-4} \text{ cm}^{-1}$. The big improvement came in the surface absorption coefficient which was typically in the neighborhood of $10^{-4}/\text{surface}$. The crystals grown from CCl_4 -treated material were generally inferior to the Br_2 -treated crystals. Many of the samples had visible bubbles as well as macroscopic bits of carbon embedded randomly throughout. Those that did not possess these faults had bulk absorption coefficients slightly higher than the Br_2 -treated crystals. Unfortunately large surface absorption coefficients ($\gtrsim 5 \times 10^{-4}/\text{surface}$) were present in all of the CCl_4 -treated crystals. The CCl_4 -processing was attempted a number of times with little variation in end results.

A significant improvement in the $10 \mu\text{m}$ absorption properties of Br_2 -treated KBr came about when the Czochralski-grown crystals were pulled a factor of 3 more slowly (<1 cm/hr as opposed to the typical 2.5 cm/hr). The bulk absorption coefficient was measured to be about $1.2 \times 10^{-4} \text{ cm}^{-1}$. The absorption resonance at 1030 cm^{-1} was significantly smaller and surface absorption was also reduced to negligible levels. The only explanation for this improvement is that the slowly grown crystals are structurally better (not as many defects) than the conventionally grown

crystals. More structural perfection can explain better absorption properties in both the bulk and on the surface.

A comparison of various surface preparations was made. Samples were first cleaved and absorption measurements were made. Then the sample would be polished as described in Section D and remeasured. This procedure could be repeated a number of times on long samples and in this way the effect of various polishing solvents on the absorption can be determined. Without exception the lowest surface absorption coefficients were measured in samples with cleaved ends. Any type of surface treatment produced higher surface absorption coefficients. The effect of using different polishing solvents was minimal. The surface absorption coefficient of a polished sample can be restored to its initial "cleaved" value by cleaving the polished ends of the crystal. The HBr etching procedure suggested by us³⁴ and demonstrated by Hass et al. was attempted only once. The results were unsuccessful because the samples cracked when they were placed in fuming HBr. This procedure warrants further investigation because of its successful implementation at NRL.⁴⁰

An interesting set of experiments was performed to determine the effects of crystal orientation ([111] vs. [100]) and growth technique (Czochralski vs. Bridgeman) on absorption properties of KBr crystals at 10 μm . Crystals for the orientation test were grown by the Czochralski method. Crystals for the growth test were all grown along the [111] direction. Except for the directionality in the one case and the growth technique in the other, the crystals were treated identically. They were

grown from the same batch of starting materials and were cut and polished in the same way. In the test for optimum orientation the [111] crystals had bulk absorption coefficients between $3 \times 10^{-4} \text{ cm}^{-1}$ and $8 \times 10^{-4} \text{ cm}^{-1}$ with the characteristic rise in absorption with increasing frequency. The surface absorption coefficient is quite small ($\sim 3 \times 10^{-4}/\text{surface}$). The [100] crystals on the other hand had bulk absorption coefficients ranging between $4 \times 10^{-4} \text{ cm}^{-1}$ and $9 \times 10^{-4} \text{ cm}^{-1}$. The surface absorption coefficients were huge ($> 10-15 \times 10^{-4}/\text{surface}$).

The results of the growth-technique test were equally interesting. The Czochralski [111] crystals were described in the previous paragraph. The Bridgman [111] crystals on the other hand had bulk absorption coefficients as low as $1 \times 10^{-4} \text{ cm}^{-1}$ and no higher than $2 \times 10^{-4} \text{ cm}^{-1}$ at 1030 cm^{-1} . These crystals also had no detectable surface absorption.

The results of these two tests are very instructive and, in hindsight, exactly what one would expect. The [111] direction should be better than the [100] direction because the density of atoms looking down a [111] direction is greater than down a [100] direction. This should presumably yield better surface properties. The Bridgman technique is a 24-hr growth and it was already demonstrated that slow growths produce better crystals than fast growths. In addition to this, the crystals in the Bridgman furnace are more-or-less annealed as they are grown. The effects of annealing on $10 \mu\text{m}$ absorption in KBr are not known but the absorption properties are most likely improved if a crystal is annealed.

The $10 \mu\text{m}$ absorption properties of several crystals of KI were

investigated. The starting material from which the KI crystals were grown was not pretreated nor were any special growth techniques (e.g. slow growth) used. The absorption coefficients were surprisingly low and comparable to KBr grown from Br₂-treated starting material. The bulk absorption coefficient increased from $3.6 \times 10^{-4} \text{ cm}^{-1}$ at 931 cm^{-1} to $6 \times 10^{-4} \text{ cm}^{-1}$ at 1050 cm^{-1} . The surface absorption was small but did exhibit the 9.8 μm resonance.

The absorption resonance in the vicinity of 9.8 μm has now been observed in three potassium halides: KCl⁶, KBr, and KI. To investigate whether this effect might be due to the potassium ions (e.g. impurity-potassium complexes) a pure RbCl crystal was investigated. If the absorption resonance at 9.8 μm is due to the potassium ions, then in RbCl the effect should presumably be shifted or nonexistent. However, this is not the case. The sample exhibited an increasing bulk absorption coefficient ($5 \times 10^{-4} \text{ cm}^{-1}$ at 931 cm^{-1} to $15 \times 10^{-4} \text{ cm}^{-1}$ at 1050 cm^{-1}) as well as a dramatic resonance in the surface absorption coefficient. This behavior seems to exclude a potassium complex as the obvious culprit and indicates that this absorption resonance might be common to all alkali halides. This point needs further study.

It is well known that divalent alkaline earth impurities structurally strengthens alkali halide crystals. However, the effect of such impurities on the absorption coefficients at 10 μm is not well known. Thus far we have investigated two Czochralski-grown CaBr₂-doped KBr crystals, one with 50 ppm CaBr₂ and the other with 100 ppm CaBr₂. Both crystals exhibited similar absorption properties. The bulk absorption coefficients

were the same as those of pure KBr crystals. However, the surface absorption was slightly higher in the doped samples than in the pure crystals. No experiments were done on slowly grown or Bridgman CaBr_2 -doped KBr crystals. Higher doping levels should also be tried.

F. Conclusions

In summary, all KBr crystals exhibit anomalous bulk and surface absorptions. An extrinsic absorption resonance near $9.8 \mu\text{m}$ exists in all samples investigated thus far. Reactive atmosphere processing of the starting material improves the absorption properties of the samples. The best crystals with respect to $10 \mu\text{m}$ absorption are grown slowly, either by slow-pull Czochralski method or by 24-hr. Bridgman growths. Bulk absorptions as low as 10^{-4} cm^{-1} were measured in these crystals with no detectable surface absorption. Polishing crystals has thus far degraded the surface absorption coefficient. Doubly grown crystals and crystals grown from leftover melt material have absorption coefficients several times higher than singly grown crystals. Bridgman growth produces better crystals than the Czochralski method. The [111] direction is superior to the [100] direction especially in surface properties. Addition of 100 ppm CaBr_2 to a KBr crystal does not degrade the bulk absorption coefficient but there is a slight increase in the surface absorption. Untreated KI has a bulk absorption coefficient as low as $3.5 \times 10^{-4} \text{ cm}^{-1}$ with little surface absorption. As in KCl, KBr the $9.8 \mu\text{m}$ absorption resonance is present in KI. A RbCl crystal showed the same resonance behavior as KCl, KBr, and KI eliminating potassium as the source of the anomalous absorptions.

Chapter III

ABSORPTION, SATURATION AND EXCITED STATE LIFETIMES OF IMPURITIES IN ALKALI HALIDES

A. Introduction

Eight years ago Geller and Sievers⁴¹ studied the infrared absorption properties of ReO_4^- * impurities in alkali halide lattices in the vicinity of 920 cm^{-1} using a grating monochromator. The absorption of the ν_3 internal mode was found to be extremely narrow even at room temperatures. Many of the measured widths, especially at low temperatures were instrument limited ($\sim 1 \text{ cm}^{-1}$). This narrow resonance is reminiscent of even narrower infrared absorptions in gases which in many cases can be easily saturated (i.e., the effective absorption coefficient decreases with increasing power) at modest levels of infrared laser radiation. On the basis of these observations one might anticipate that the ν_3 vibrational mode of ReO_4^- molecules in alkali halide matrices could be saturated at some level of CO_2 laser radiation. Such saturation measurements would provide means for determining an otherwise unmeasurable quantity, namely the excited state lifetime T_1 of the internal vibrational mode of the impurity molecule in the solid matrix.

*The ReO_4^- molecule has four normal modes of vibration⁴², all of which are Raman active and two of which are infrared active. The two infrared active modes are $\nu_3 (918 \text{ cm}^{-1})$ and $\nu_4 (343 \text{ cm}^{-1})$, and the Raman modes are ν_1 and ν_2 (971 cm^{-1}) and ν_4 (331 cm^{-1}). The ν_3 mode falls in the tuning range of a CO_2 laser making laser studies feasible.

This chapter describes the efforts leading up to and the results of saturation measurements of ReO_4^- impurities in KI and KBr matrices. Numerous difficulties impeded progress in this work. A special pulsed-discharge Q-switched laser had to be constructed to obtain Q-switched laser pulses on weak high-J lines. Low-temperature 10 μm window seals had to be developed to make measurements at cryogenic temperatures possible. Temperature dependent measurements were complicated by changing absorption coefficients (due to the fact that not only does the overall absorption strength change with temperature but also the center frequency of the absorption resonance is dependent on the host lattice constant which, in turn, changes with temperature). The excited state lifetime T_1 of the ReO_4^- molecule in KI is determined as a function of temperature between 300 K and 1.3 K. As expected, the lifetime increases as temperature is decreased. T_1 for ReO_4^- in KBr at 100 K is also determined.

Section B describes the Q-switched CO_2 laser and the pulsed-discharge techniques used to obtain Q-switched radiation on weak laser lines. Section C describes the cryostats and detectors used in the various experiments leading up to and including the saturation measurements. Section D contains descriptions of the near infrared absorption measurements and Raman scattering experiments on alkali halides doped with ReO_4^- . The theory by which the excited-state lifetime is computed from saturation data for both homogeneously and inhomogeneously broadened absorbers is found in Section E. Section F describes the experimental arrangement of the absorption and saturation measurements.

Section G contains the results and discussion of the saturation measurements and Section H discusses the peculiar pulse attenuation and reshaping phenomena observed in $KI + ReO_4^-$ samples at low temperatures.

B. Microsecond CO₂ Laser Pulses

Methods for extracting intense laser pulses less than 2 μ sec in duration from the Apollo laser and their optical characteristics are described in this section. The bulk of the section is devoted to Q-switching techniques. Both cw discharge and pulsed discharge Q-switching are described. The final part of this section describes an alternate source of short pulses called precursor pulses which occur when the laser is operated in the chopped or pulsed mode. It should be noted that all the characteristics of the microsecond pulses were investigated for two mixtures of laser gas. This section contains all the information relevant to mixture I (to be described shortly) which is the normal Apollo laser gas mixture while Appendix IV contains the pulse characteristics of mixture II.

1. Q-Switched CO₂ Laser (cw Discharge)

A homemade Q-switcher mechanically Q-switches the modified Apollo laser to obtain very high peak powers (\sim 10 kW). The schematic diagram of the tunable Q-switched laser is shown in Figure III-1. The grating configuration remains unchanged from the cw mode of operation but the output mirror is mounted at 90° to the laser cavity. A .75" gold mirror is mounted on a 2½" diameter rotating shaft and is rotated at frequencies between 75 Hz and 250 Hz. The optical cavity is aligned only when the rotating mirror is in the 45° orientation shown in Figure III-1. Otherwise, the cavity is misaligned and no lasing action can occur. When the mirror comes into alignment an intense burst of CO₂ laser radiation is emitted in a pulse similar to the one shown in Figure III-2. The leading

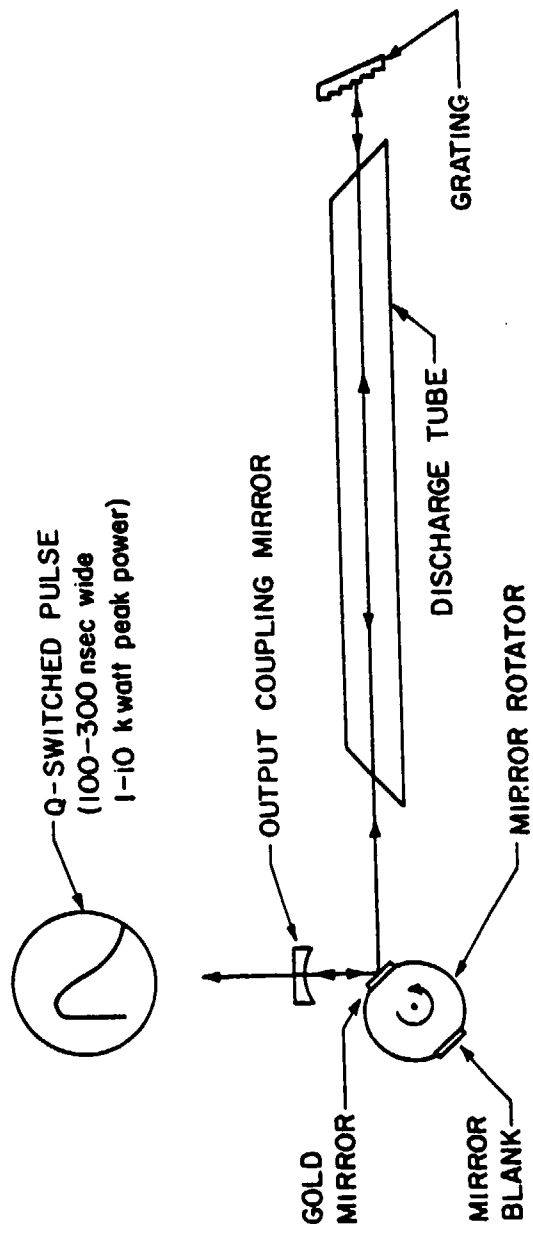


Figure III-1. Schematic diagram of tunable Q-switched CO_2 laser.

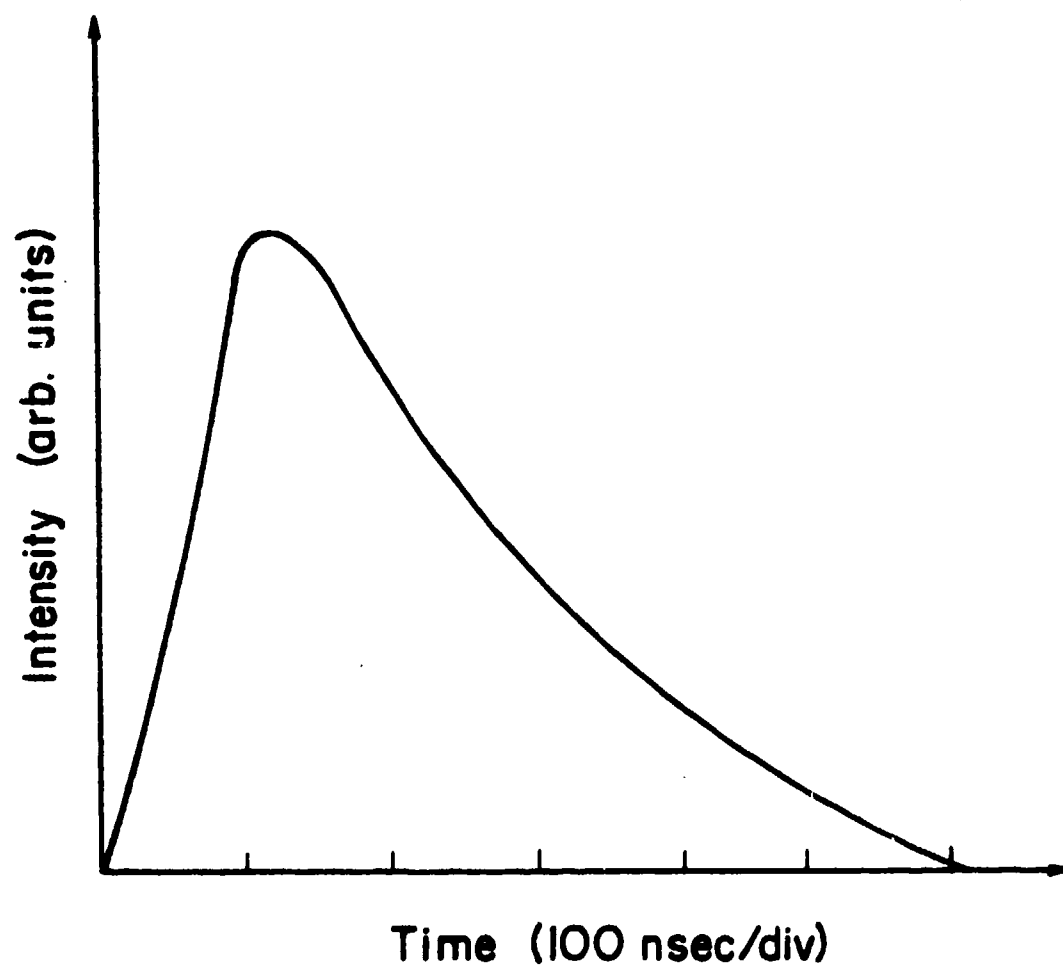


Figure III-2. Shape (intensity vs. time) of typical Q-switched CO₂ laser pulse.

edge of the pulse is extremely sharp (the rise time shown in the figure is detector limited) whereas the shape and duration of the trailing edge are critically dependent on numerous laser parameters.

The purpose of this section is to catalogue and explain some of the various dependences of pulse height, duration, and shape on such parameters as laser gas pressure and mixture, discharge current, mirror rotational frequency, and position of the CO₂ line in the band (i.e. weak laser lines as opposed to strong lines). Not only are there numerous parameters which affect the Q-switched pulses but many of the parameters are intimately tied together so that a change in one parameter may produce the same or opposite effect on the laser pulses that a change in one or more of the other parameters would produce. Therefore, it is impossible to list a unique set of conditions which produce the optimum output pulses. It is much easier to specify the general conditions needed to optimize a particular feature in the pulses--for example, peak power, pulse width, pulse energy, etc. To be able to explain the changes in Q-switched pulses as a function of the various parameters requires an exhaustive knowledge of laser gas kinetics which is beyond the scope of this work. Therefore, many "effects" will be left unexplained while some of the more obvious ones will be treated briefly.

Q-switched laser operation was investigated for two different gas mixtures. One mixture contained 18% N₂, 6% CO₂, 76% He (henceforth referred to as mixture I); the other mixture contained 18% N₂, 16% CO₂, 66% He (mixture II). The results of investigations using mixture I are presented here while those for mixture II are catalogued in Appendix IV.

It should be noted that cw and chopped operation using mixture I

provided output powers up to 75% higher than those obtained using mixture II.

Figures III-3 and III-4 show the peak power dependence on the rotating mirror frequency for the P(8), P(20), P(36) and R(8), R(22), R(30) lines of the (00^01-10^00) band using mixture I laser gas. Discharge current and gas pressure were "optimized" for the individual lines. In addition, the small numbers along the curves represent the total pulse duration in microseconds for various frequencies. Total pulse lengths are measured rather than halfwidths for two reasons. First of all, halfwidth measurements are inaccurate because they depend on the speed of the detector and, as mentioned before, the true leading edge of the pulse cannot be resolved by our Ge:Cu detectors. Secondly, certain variation in laser parameters produce distorted multiply-peaked Q-switched pulses. In these cases it is not clear exactly how to measure the halfwidth. Figures III-5 and III-6 plot peak output power vs. discharge current for mixture I. Again, pulse duration is indicated by the numbers along the curves. Although the discharge currents in Figures III-5,6 are listed in arbitrary units, these numbers in fact correspond to the number on the MAGNITUDE dial of the laser power supply. Figures III-7 and III-8 plot peak power vs. laser gas pressure for mixture I. Plots similar to those in Figure III-3 to III-8 can be drawn for lines in the (00^01-02^00) band but the behavior of these lines is similar to the (00^01-10^00) lines and therefore these plots will be omitted. In the following discussion the various lines will be grouped into three classes: a) strong lines, P(20) and R(22); b) high-J lines, P(36) and R(30); c) low-J lines, P(8) and R(8).

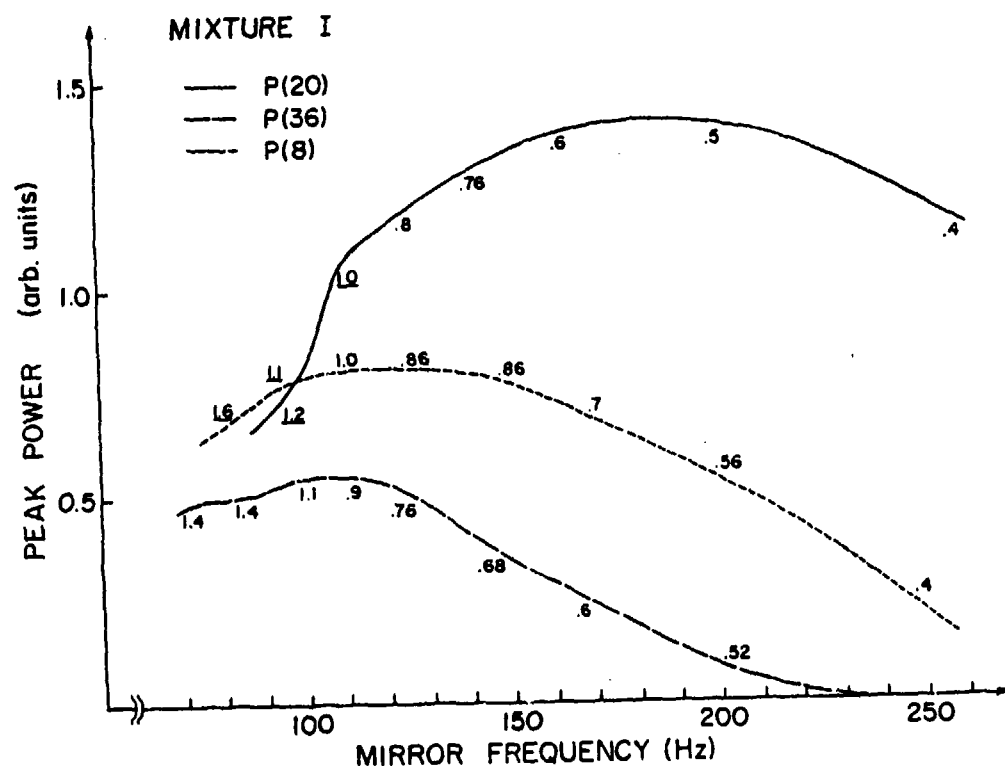


Figure III-3, III-4. Peak Q-switched power vs. mirror frequency for P(8), P(20), P(36) and R(8), R(22), R(32) lines of the (00^01-10^00) band using Mixture I. The numbers alongside the curve represent the full pulse width in μ sec for particular values of mirror frequency. Underlined numbers indicate distorted or multiply-peaked pulses. The pressure and current settings are as follows:

| | Pressure (torr) | Discharge current |
|-------|-----------------|-------------------|
| P(8) | 17 | 4.5 |
| P(20) | 23 | 3.5 |
| P(36) | 17 | 4.0 |
| R(8) | 23 | 5.0 |
| R(22) | 23 | 4.0 |
| R(32) | 17 | 5.5 |

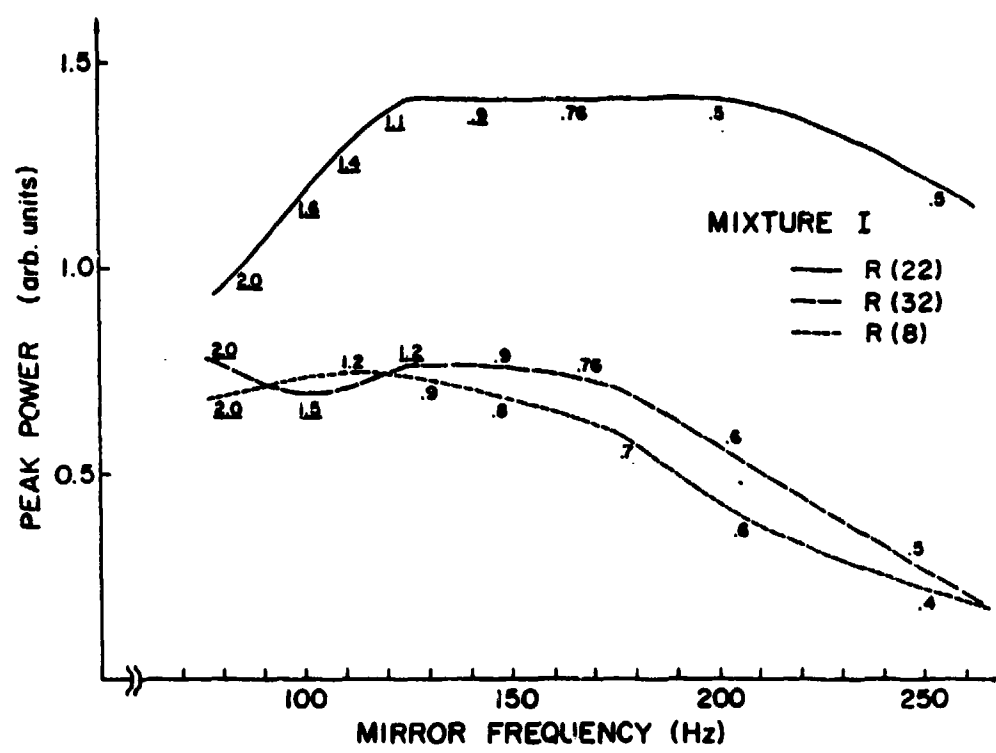


Figure III-4. See figure caption on previous page.

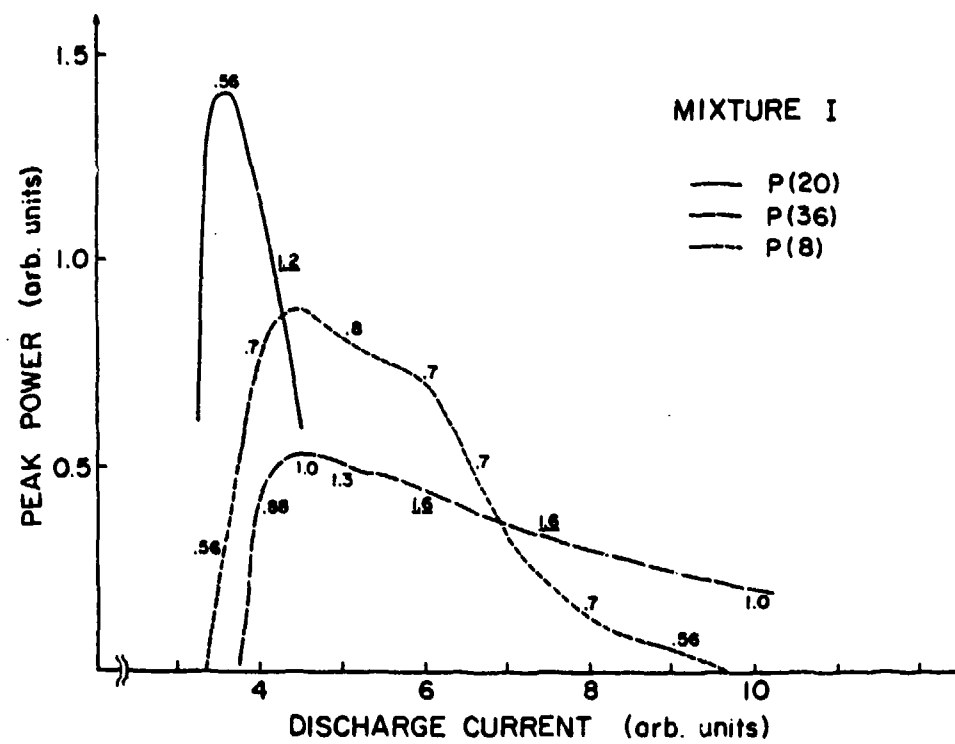


Figure III-5, III-6. Peak Q-switched power vs. discharge current for P(8), P(20), P(36) and R(8), R(22), R(32) lines of the (00^01-10^00) band using mixture I. The units of current correspond to the numbered scale on the laser power supply. The numbers alongside the curve represent the full pulse width in μ sec for particular values of discharge current. Underlined numbers indicate distorted or multiply-peaked pulses. The pressure and mirror frequencies for the various lines are as follows:

| | Pressure (torr) | Mirror frequency (Hz) |
|-------|-----------------|-----------------------|
| P(8) | 17 | 143 |
| P(20) | 23 | 167 |
| P(36) | 17 | 111 |
| R(8) | 23 | 143 |
| R(22) | 23 | 167 |
| R(32) | 17 | 143 |

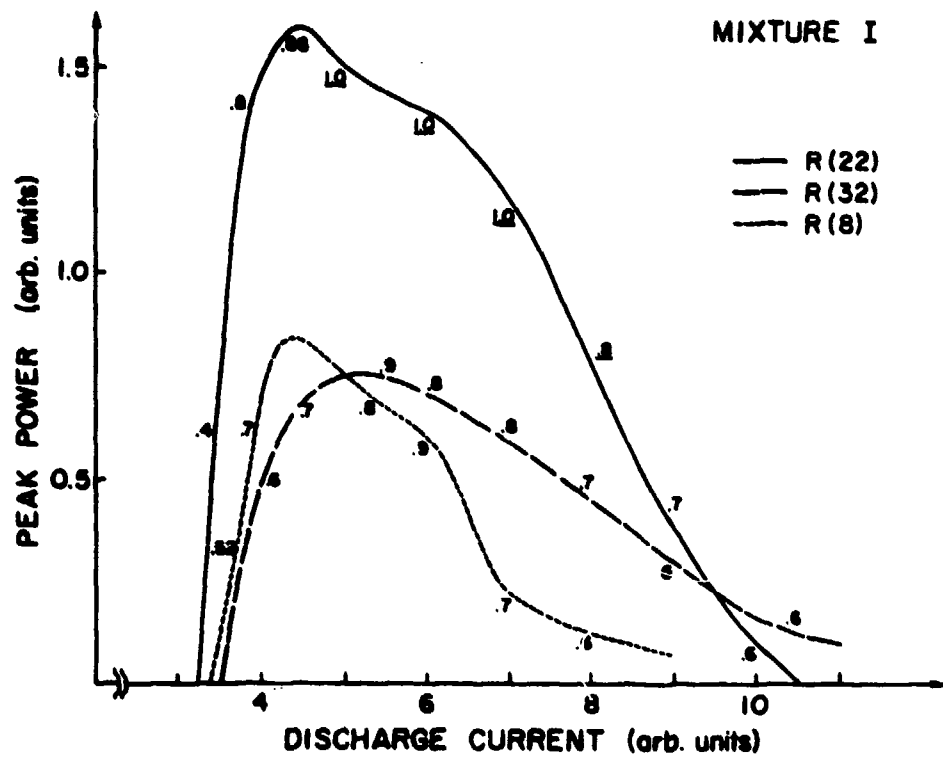


Figure III-6. See figure caption on previous page.

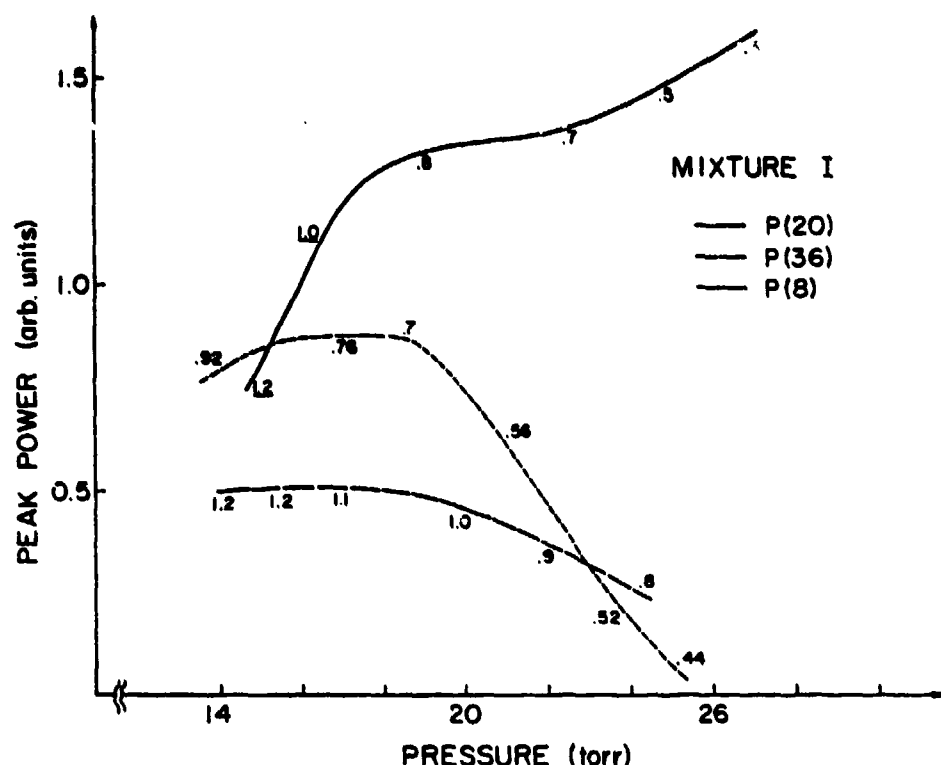


Figure III-7, III-8. Peak Q-switched power vs. laser gas pressure for P(8), P(20), P(36) and R(8), R(22), R(32) lines of the (00⁰1-10⁰0) band using mixture I. The numbers alongside the curves represent the full pulse width in usec for particular values of pressure. Underlined numbers indicate distorted or multiply-peaked pulses. The mirror frequency and discharge current for the various lines are as follows:

| | Mirror frequency (Hz) | Discharge current |
|-------|-----------------------|-------------------|
| P(8) | 143 | 4.5 |
| P(20) | 167 | 3.5 |
| P(36) | 111 | 4.5 |
| R(8) | 143 | 5.0 |
| R(22) | 167 | 4.5 |
| R(32) | 143 | 5.5 |

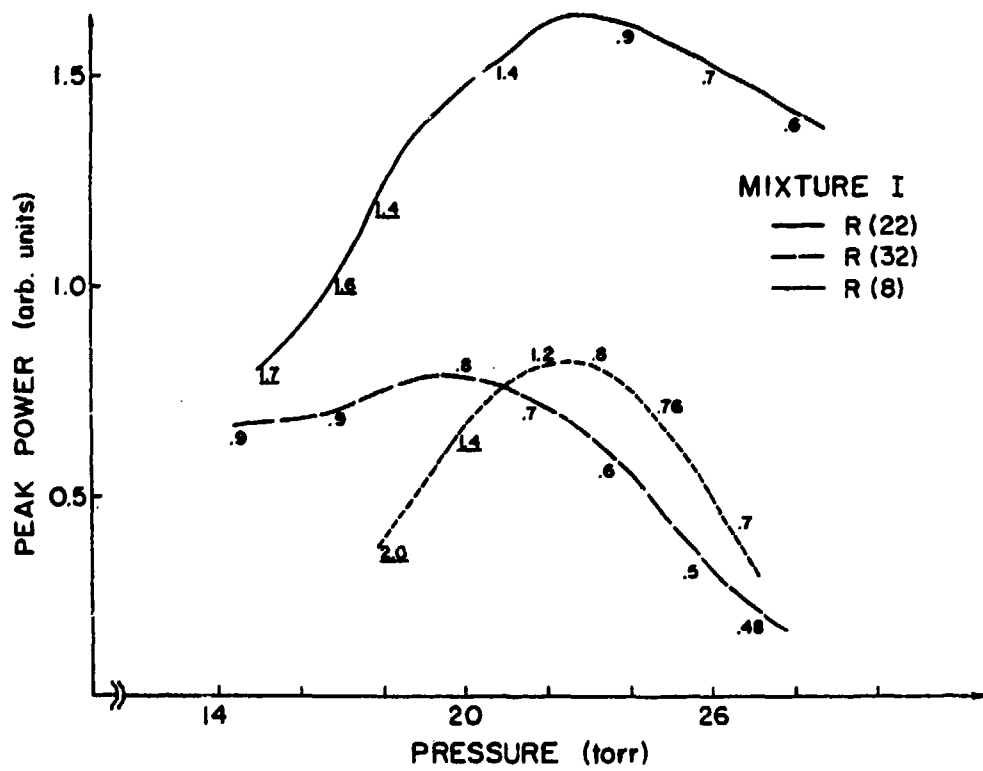


Figure III-8. See figure caption on previous page.

Mirror Speed

Optimum mirror frequencies for strong CO₂ lines are typically considerably higher than those for low- or high-J lines. The lower gain of the high- and low-J lines give rise to slower buildup of laser oscillation and therefore require longer "dwell" times (time during which the cavity is aligned). These long dwell times exist at lower mirror speeds. When mirror speeds become too low, however, the switch-on time becomes longer and the output pulses lose some of their sharpness in the leading edge (most of the time this loss in sharpness is still undetectable with our Ge:Cu detectors). This is accompanied by a decrease in peak power as expected. For even lower mirror frequencies the CO₂ pulses become distorted as shown in Figure III-9. The primary and secondary peaks can be understood as follows. The energy in the initial peak comes from CO₂ molecules lasing from the upper to the lower laser level. When the upper laser level becomes partially empty the power in the pulse begins to decrease (this defines the first peak). Before the power can decay to zero, however, the upper laser level is repopulated by means of CO₂-N₂ collisions and this gives rise to the second peak. The fact that at typical gas pressures CO₂-N₂ energy-transfer collisions have a time constant longer than the "lasing lifetime" of the upper level gives rise to the doubly-peaked Q-switched pulse. At very high mirror frequencies the dwell times become too short and peak powers begin to decrease. For all laser lines the pulse widths decrease with higher mirror speeds because of the short alignment time.

Discharge Current

All Q-switched CO₂ laser lines have well defined discharge currents

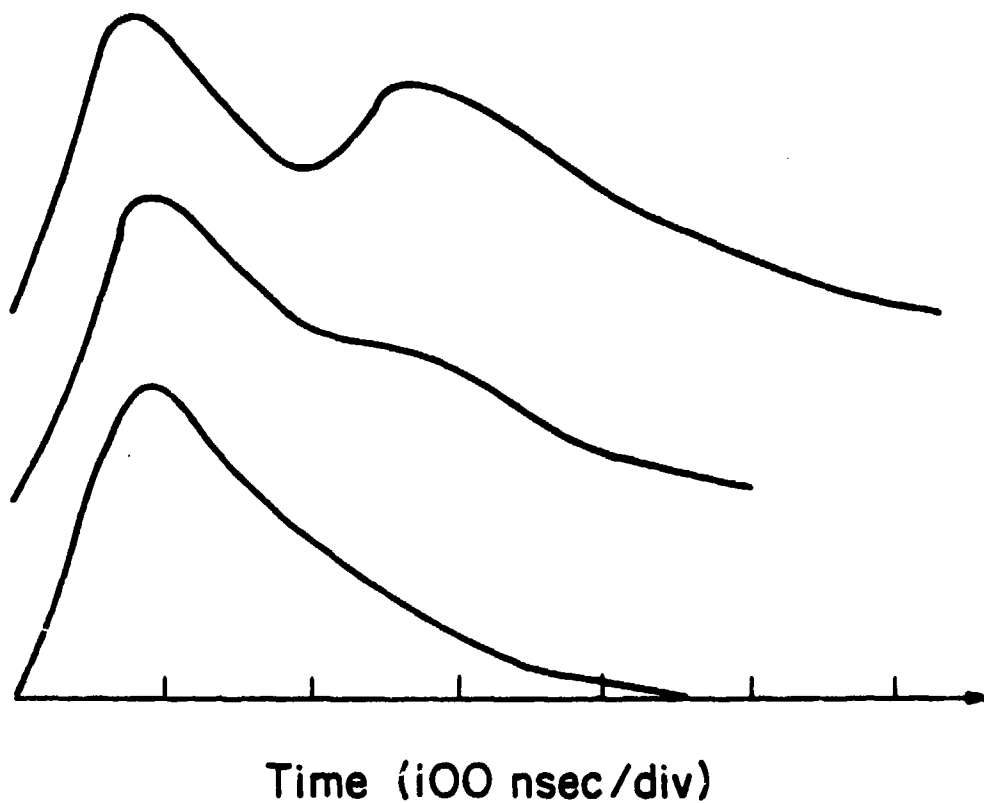


Figure III-9. Intensity vs. time plots of various Q-switched pulses. The lowest pulse is undistorted. The middle pulse exhibits a shoulder on the trailing edge of the pulse. The top pulse is a double-peaked pulse.

for which the peak power is optimized (Figures III-5,6). Such well defined optimum discharge currents exist because of the critical dependence of upper laser level population on electron energies in the discharge. If the current (which is proportional to the voltage across the laser tube) is too low, the electrons in the discharge will have energies insufficient to excite CO_2 molecules (or N_2 molecules) to the upper laser level. If the energy of the electrons is too high (high discharge current), the excitation process will be inefficient, i.e., higher vibrational states of the CO_2 molecule will be excited. The energy transfer process of CO_2 -electron impacts is a fairly selective excitation mechanism and therefore there are very distinct optimum currents for Q-switched operation. Note that the optimum discharge current varies only slightly for the various Q-switched lines.

The Q-switched pulse widths are typically maximum at the optimum operating current and become narrower for lower and higher discharge currents. This is easily explained by noting that the gain in the laser is highest at the optimum discharge current. At these high gains more misalignment of the rotating mirror can be tolerated without complete suppression of lasing. This gives rise to laser action for longer time, i.e. larger pulse widths, when the current is optimized.

Pressure

The pressure dependence of peak Q-switched pulse powers is fairly similar to the current dependence. For the most part each CO_2 line has a fairly well defined optimum gas pressure. The similarity between pressure and current dependent curves is not coincidental because the physical processes that determine these curves are basically the same.

As explained in the previous section, upper laser level excitation is critically dependent on electron energies. Two things determine the electron energies. One is the voltage across the tube; the other is the acceleration time of the electrons (i.e., the time between electron-molecule collisions). The voltage (current) effect is discussed in the previous section. The second effect is simply a pressure effect. For higher pressures the electron acceleration time is short, so the electron energy upon impact with a gas molecule is low. The converse is true for low pressures. Therefore, there should be an optimum pressure for which the electron energies are optimized.

2. Pulsed-Discharge Q-Switched CO₂ Laser

The advantages of pulsed-discharge operation of Q-switched CO₂ laser over cw-discharge operation is discussed in Appendix I. Enhancement in peak power in the pulsed-discharge mode is expected because of the cooler laser gas tempearture. A schematic diagram of a pulsed-discharge Q-switched CO₂ laser is shown in Figure III-10a-c. A helium-neon laser beam is reflected by the rotating mirror onto a photodiode (the photodiode circuitry is shown in Figure III-11). The output of the photodiode triggers a variable pulse width (2 msec-200 msec), variable-delay (.8-14 msec) pulsing circuit (Figure III-12). The output of this pulser is always +12.5 V except when triggered by the photodiode in which case the output drops to 0V after a delay time determined by a ten-turn pot and remains zero for .6-14 msec as determined by another ten-turn pot. The output of the pulser is connected to the EXT ON-OFF connector on the laser power supply. As mentioned in Chapter II-C, +12 V applied to the

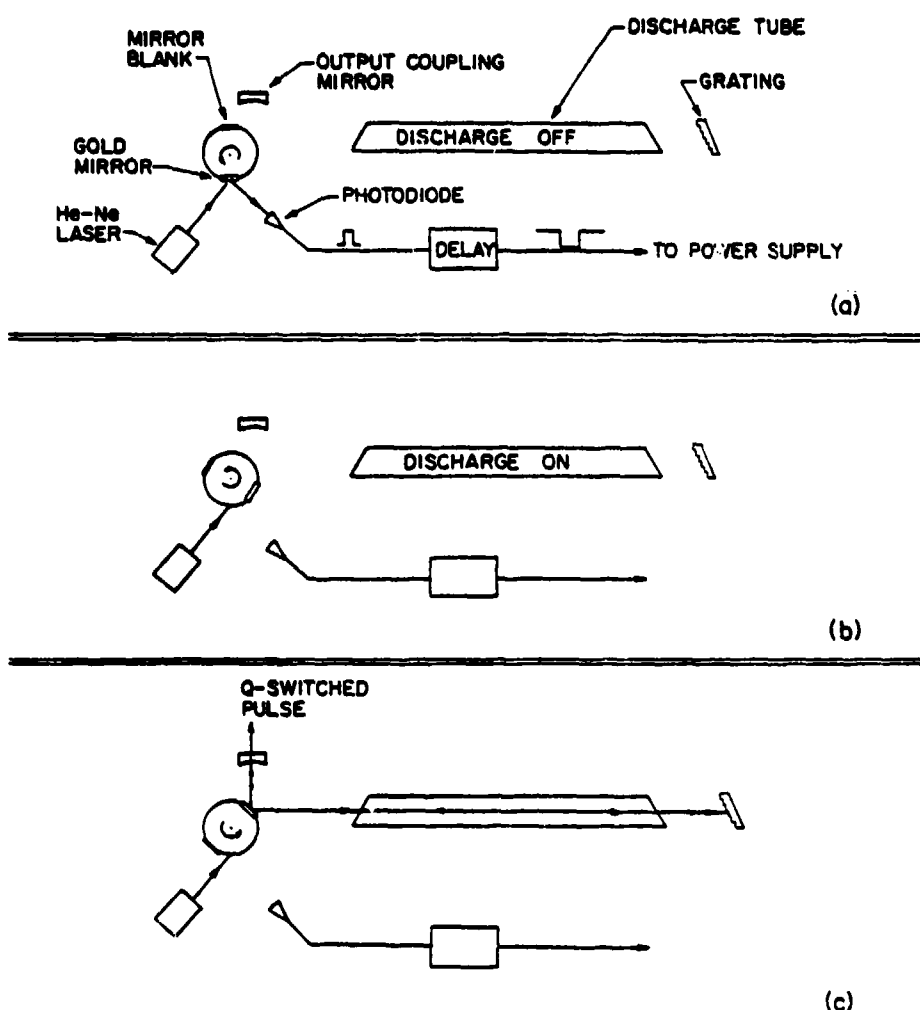


Figure III-10. Schematic diagram of the pulsed-discharge Q-switched CO₂ laser. a) The discharge is off during the dead time of the laser. A He-Ne laser and a photodiode trigger a delay circuit which turns the discharge on several milliseconds before the mirror comes into alignment as shown in (b). c) The mirror completes the optical cavity and a Q-switched CO₂ pulse is emitted. The laser discharge turns off and the cycle is repeated.

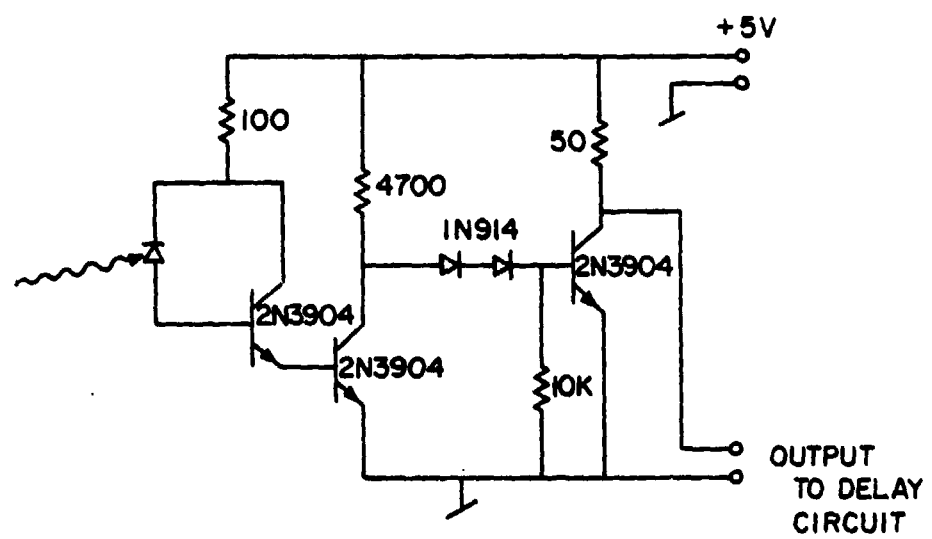


PHOTO DIODE TRIGGER CIRCUIT

Figure III-11. Schematic diagram of photo diode trigger circuit.

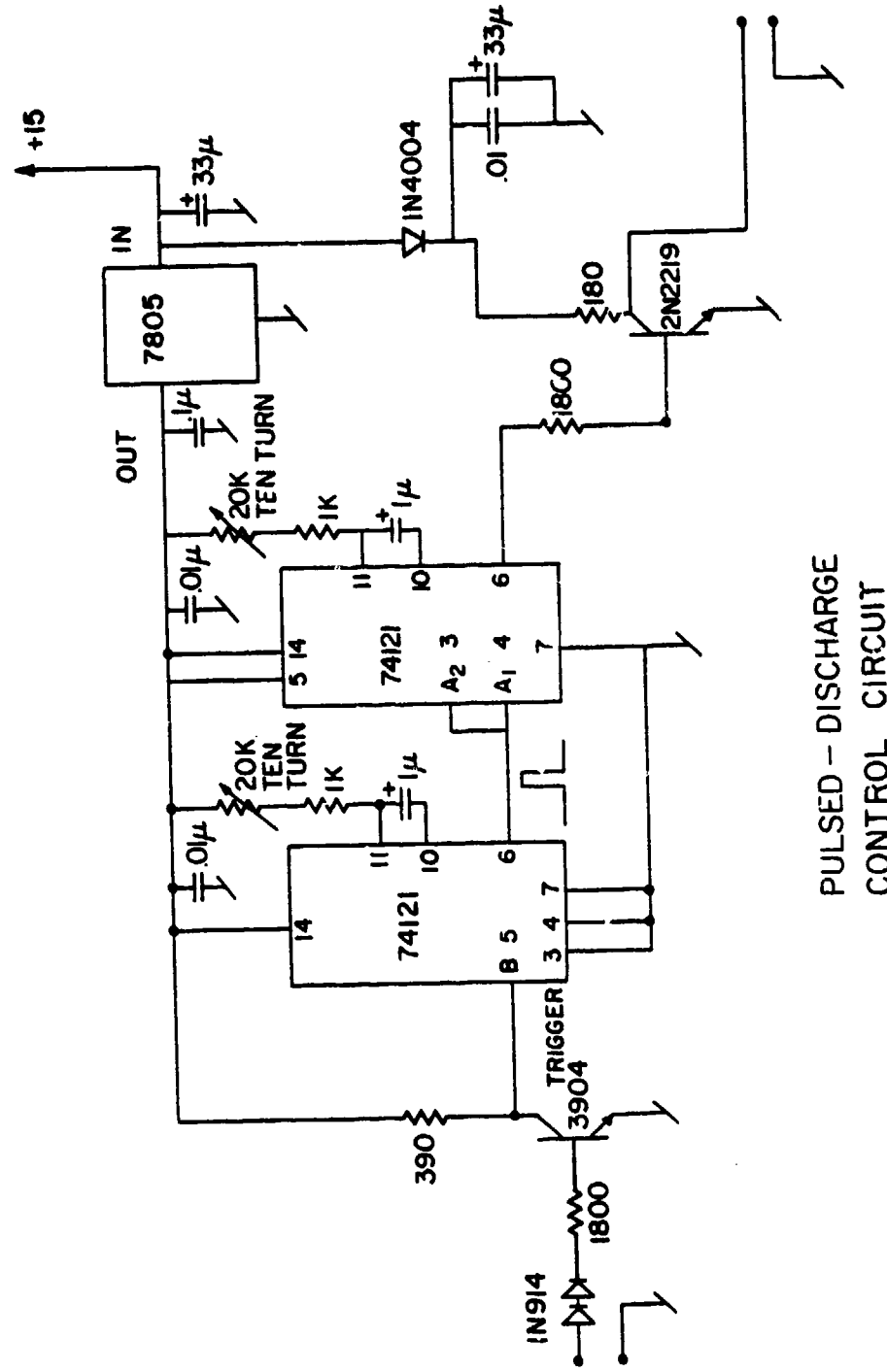


Figure III-12. Schematic diagram of variable pulse width, variable delay circuit which controls the laser discharge during pulsed-discharge Q-switching.

EXT ON-OFF connector turns the laser discharge off. When triggered by the photodiode the pulser voltage drops to zero and the discharge turns on. When the voltage returns to 12.5 V, the discharge is once again turned off.

The various laser parameters such as current, pressure, and mirror frequency for the most part do not need to be changed when Q-switched operation is changed from cw-discharge to pulsed-discharge. The optimum discharge pulse width varies from 1 to 2 msec and the optimum position of the discharge pulse relative to the optical pulse is shown in Figure III-13.

Table III-1 lists the (00^01 - 10^01) band tuning range of the Q-switched CO_2 laser in both the cw-discharge and pulsed-discharge modes of operation using gas mixture I. The peak power enhancement of pulsed discharge operation was measured for several lines and is also shown in the table. The enhancement in the pulsed-discharge mode is not the same for all the CO_2 laser lines. The strongest lines are enhanced only slightly whereas the low- and high-J lines have much higher enhancement ratios. In addition, the pulsed discharge increases the tuning range of the Q-switched CO_2 laser. This additional tuning is extremely important for the saturation experiments described later in this chapter. For example, one set of experiments required Q-switched operation on the P(42) line which lases only in the pulsed-discharge mode. These experiments would have been impossible with the cw-discharge Q-switched laser.

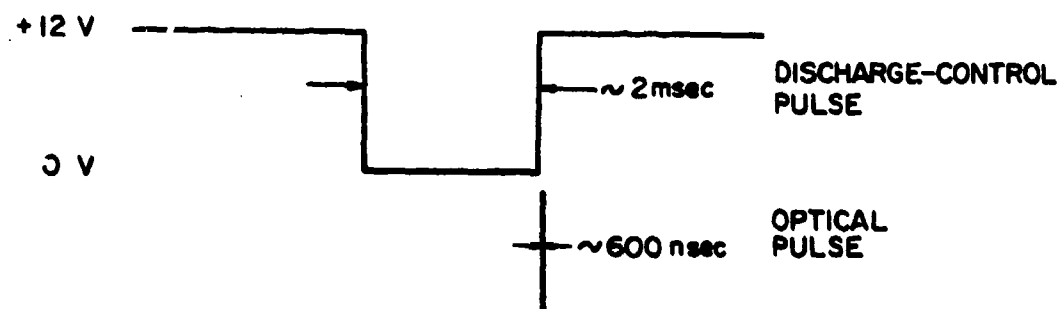


Figure III-13. Optimum relative temporal orientation of discharge pulse with respect to optical (Q-switched) pulse.

Table III-1
TUNING RANGE OF Q-SWITCHED CO₂ LASER
MIXTURE I

| cw Discharge | Pulsed Discharge | Power Ratio ($\frac{\text{Pulsed}}{\text{cw}}$) |
|--------------|------------------|---|
| — | P(2) | ∞ |
| — | P(4) | ∞ |
| P(6) | P(6) | 8 |
| P(8) | P(8) | 1.5 |
| ↓ | ↓ | |
| P(20) | P(20) | 1.1 |
| ↓ | ↓ | |
| P(36) | P(36) | 1.2 |
| P(38) | P(38) | 5 |
| — | P(40) | ∞ |
| — | P(42) | ∞ |
| — | R(2) | ∞ |
| — | R(4) | ∞ |
| R(6) | R(6) | 8 |
| R(8) | R(8) | 2 |
| ↓ | ↓ | |
| R(22) | R(22) | 1.1 |
| ↓ | ↓ | |
| R(32) | R(32) | 2 |
| R(34) | R(34) | 8 |
| — | R(36) | ∞ |
| — | R(38) | ∞ |

3. Precursor Pulses

In the chopped and pulsed modes in addition to the main pulse there is a pulse much narrower than the main pulse. Evidence of this are the discontinuities at the beginning of the pulses shown in Figures II-13 and II-14. By using a Ge:Cu detector and magnifying the region of discontinuities very narrow pulses are observed as shown in Figure III-14. These precursor pulses have rise times of about 250 nsec, are about 600 nsec wide FWHM, and have peak powers comparable to or greater than the main pulse. The peak power fluctuations of these pulses are less than 10%. In about 2 μ sec the pulse decays to a value 20% of the peak value and after another 2 μ sec the onset of the main pulse occurs. The precursor pulses probably arise from the direct excitation of CO_2 by the discharge electrons while the main pulse draws its energy from CO_2 molecules excited by vibrational energy transfer from N_2 . The reason for the occurrence of two distinct pulses is twofold. First of all, the direct excitation of CO_2 by electrons is a much faster process than vibrational-energy transfer. Secondly, as discussed previously, the gain at the beginning of the current pulse is extremely high because of the cold gas and the empty lower laser level. After several hundred nanoseconds the gain drops to a lower value because the lower laser level is now no longer empty. These sudden changes in gain can be thought of as "quasi Q-switching". The combination of the two effects gives rise to the two distinct pulses, the first about 600 nsec FWHM and the second $\geq .2$ msec FWHM.

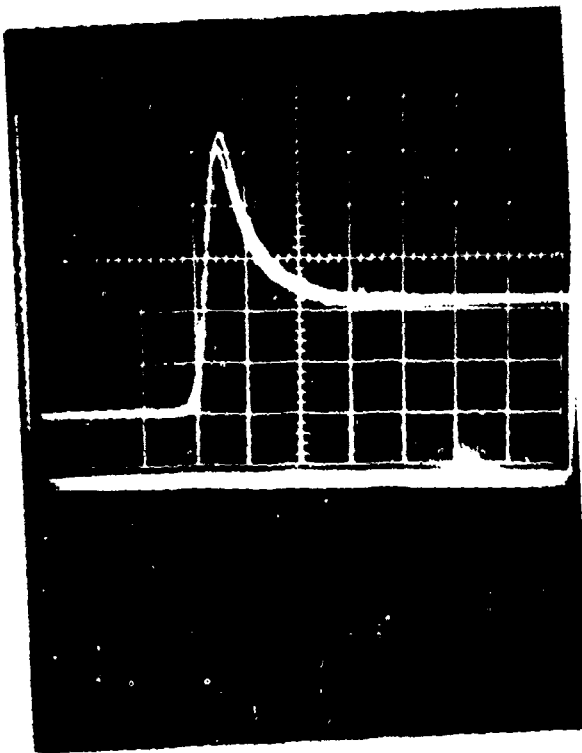


Figure III-14. Photograph of precursor pulse preceding the main pulse in the chopped or pulsed modes of the Apollo laser (2 μ sec/div).

C. Detectors and Cryostats

The various optical measurements using interferometric and laser sources required a variety of detectors and sample cryostats each of which will be described in this section. The detectors can be divided into two categories, namely room temperature detectors and cryogenic detectors. With the exception of the Molelectron Detector, the room temperature detectors are slow devices (<1000 Hz). Except for the 1.2 K germanium bolometer, the cryogenic detectors are very fast detectors (>1 MHz). The cryostats can also be divided into two classes. The ones used for near infrared and CO₂ laser spectroscopy are based on geometric optics while light pipe optics are necessary for far infrared ($\lesssim 500$ cm⁻¹) spectroscopy.

1. Room Temperature Detectors

a. Thermopile

A Coherent Radiation 201 thermopile is used to measure average infrared powers between 100 mW and 100 W. The detector time constant is very long, i.e. on the order of 1 sec.

b. Molelectron Pyroelectric Detector

A Molelectron P3-01 pyroelectric detector is used to make ac measurements as well as pulse shape analysis. The detector element is 1 mm in diameter and bias circuitry housed in the same module as the detector provides good noise immunity. The spectral response is fairly uniform from the visible to about 40 μm . Three different load resistors provide three different overall detector sensitivities and response times. The highest sensitivity at 10.6 μm is 30 V/W with a 1 msec

risetime and $\text{NEP} = 3 \times 10^{-8} \text{ W/Hz}^{\frac{1}{2}}$. Intermediate sensitivity is 350 mV/W with 10 μsec risetime and $\text{NEP} = 3 \times 10^{-7} \text{ W/Hz}^{\frac{1}{2}}$. The high speed setting gives a 100 nsec risetime with a 3.5 mV/W sensitivity and an $\text{NEP} = 3 \times 10^{-6} \text{ W/Hz}^{\frac{1}{2}}$. Other characteristics of the detector can be found in the Molelectron instruction manual.

c. Laser Precision Pyroelectric Detector

A Laser Precision pyroelectric detector is used to make low-signal ac measurements. The detector has two different load resistor modules. The E-9 module provides a sensitivity of 800 V/W with a high frequency roll off of about 1 kHz. The E-11 load resistor module has a sensitivity of 8×10^4 V/W with a high frequency roll off of about 10 Hz. The biasing of this detector is external to the detector module and this makes the detector somewhat susceptible to pickup. The detector also suffers from microphonic noise problems. When operating in the 10 μm region this problem is partially remedied by a ZnS window which covers the element.

d. Japanese Pyroelectric Detector.

Near infrared as well as far infrared ac measurements can be made using a Japanese PbTiO_3 pyroelectric detector. The responsivity to 10 μm radiation at 20 Hz is 3.5×10^4 V/W with a signal to noise ratio ~ 250 . The detector is also sensitive to radiation beyond 100 μm as evidenced by an interferogram taken on the lamellar grating interferometer.

2. Cryogenic Detectors

a. Santa Barbara Ge:Cu Detector I

High speed measurements were made with a helium temperature Ge:Cu detector which is described in detail elsewhere.⁴³ The spectral range of the detector is 2-30 μm and the risetime of the detector and amplifier is approximately 100 nsec.

b. Santa Barbara Ge:Cu Detector II

A second Ge:Cu detector belonging to T. Cool was used in the two-detector experiments. The external bias box for this detector contains a series of load resistors which determine the speed and sensitivity of the detector. A 50Ω load resistor corresponds to a risetime of about 30 nsec whereas with a 200Ω load resistor this detector has a risetime almost identical to that of the Ge:Cu detector described in the previous section.

c. 1.2 K Ge Bolometer

Far infrared interferometric and laser measurements were made with a 1.2 K Ge bolometer which is described in 3c. The sensitivity of this detector is about 10^4 V/W with an NEP of about 10^{-12} W/Hz $^{1/2}$.

3. Cryostats

a. Near Infrared Helium Immersion Cryostat

Figure III-15 shows a schematic diagram of the high frequency immersion cryostat. The sample chamber is immersed in a pumped liquid helium bath. The helium chamber is surrounded by a liquid-nitrogen-cooled shield. The room temperature windows are polished KBr windows which can be oriented normal to the incoming beam or at Brewster's angle

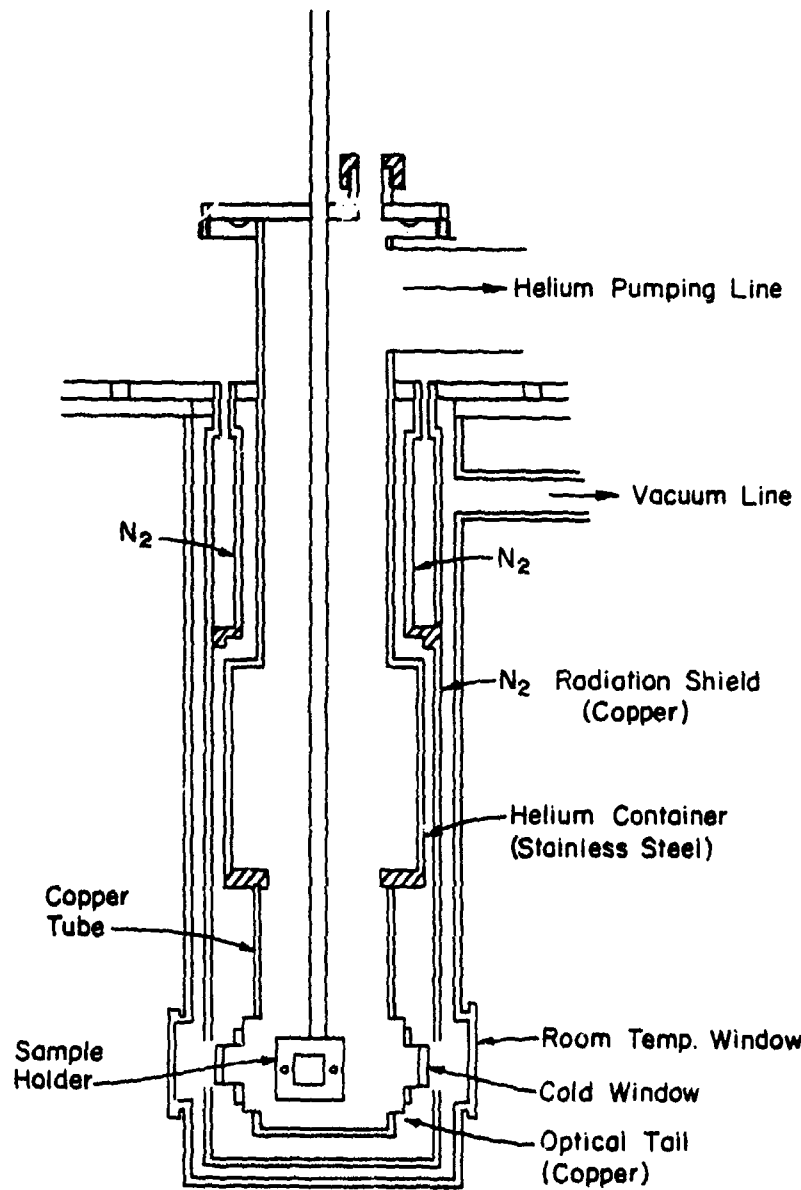


Figure III-15. Immersion cryostat. The sample holder is immersed in the refrigerant which is pumped liquid helium at 1.2K.

for laser applications. The cold windows are polished ZnSe flats mounted in annealed copper holders using Crest 7410 A and B adhesive. A great deal of effort went into obtaining an acceptable window mount which would not crack the window during repeated temperature cycling. The design which has proven to be the best is shown in Figure III-16. The holders are then soldered (Cerrolow) or epoxied (Stycast 1266) to the optical tail. However, it has been observed that even the moderate heating required to solder the window holders to the optical tail is enough to change the properties of the Crest 7410 adhesive from a soft rubbery substance to a hard glassy one. This causes leaks to occur in the adhesive after 8-10 temperature cyclings between 300 K and cryogenic temperatures. Therefore, it is advisable to epoxy the window holders to the optical tail rather than soldering them in place.

By using a two-inch pump line to pump the helium bath the minimum temperature obtainable in this cryostat is 1.25 K. Super insulation wrapped around both the helium bath and nitrogen chambers increases the hold time from about $\frac{1}{2}$ hour to over $1\frac{1}{2}$ hours. A 1000- Ω Allen-Bradley resistor attached to the sample holder is used to measure the temperature of the bath.

b. Liquid Nitrogen Cryostat

Figure III-17 shows a schematic diagram of the cold-finger cryostat used for saturation measurements above 90 K. A heater coil attached to the cold-finger sample holder provides variable temperatures. As in the case of the immersion cryostat the room temperature windows are polished KBr flats which can be mounted either normal to the optical beam or at

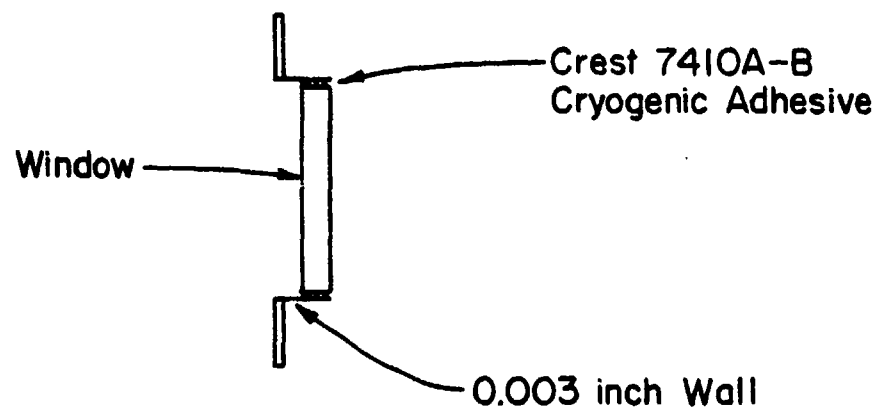


Figure III-16. Cold window for the immersion cryostat. The windows (typically ZnSe) is sealed to an annealed OFHC copper ring by means of a cryogenic adhesive.

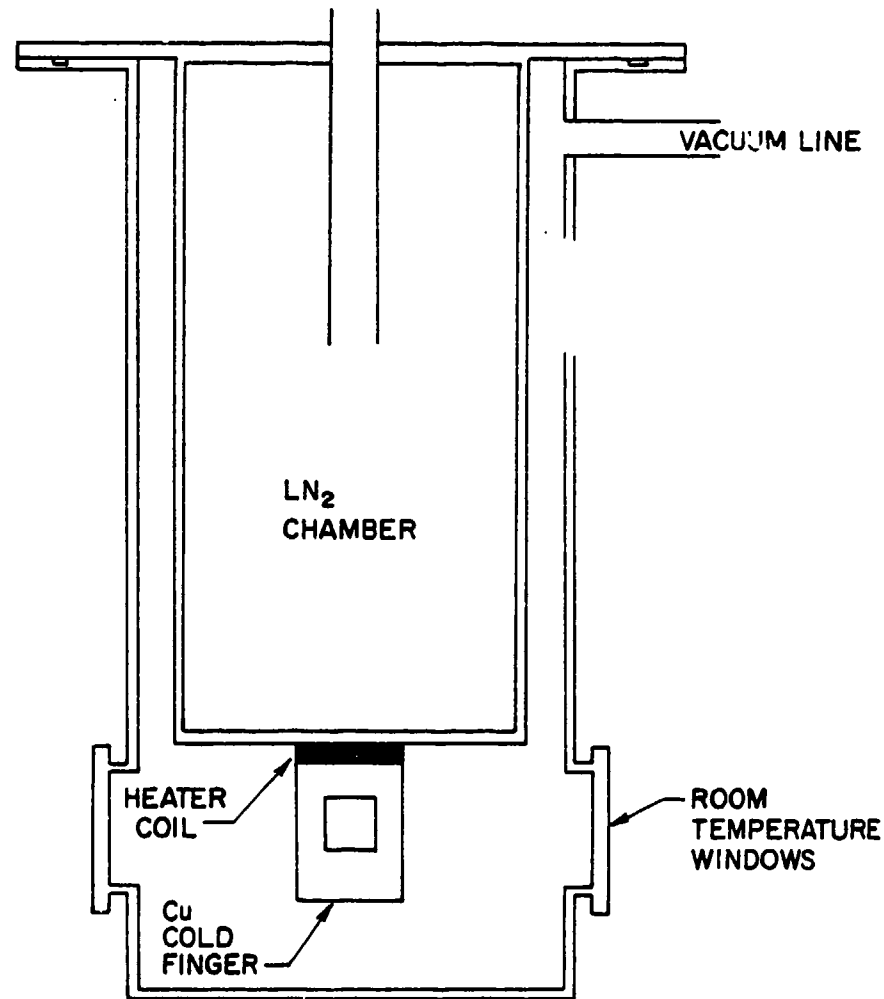
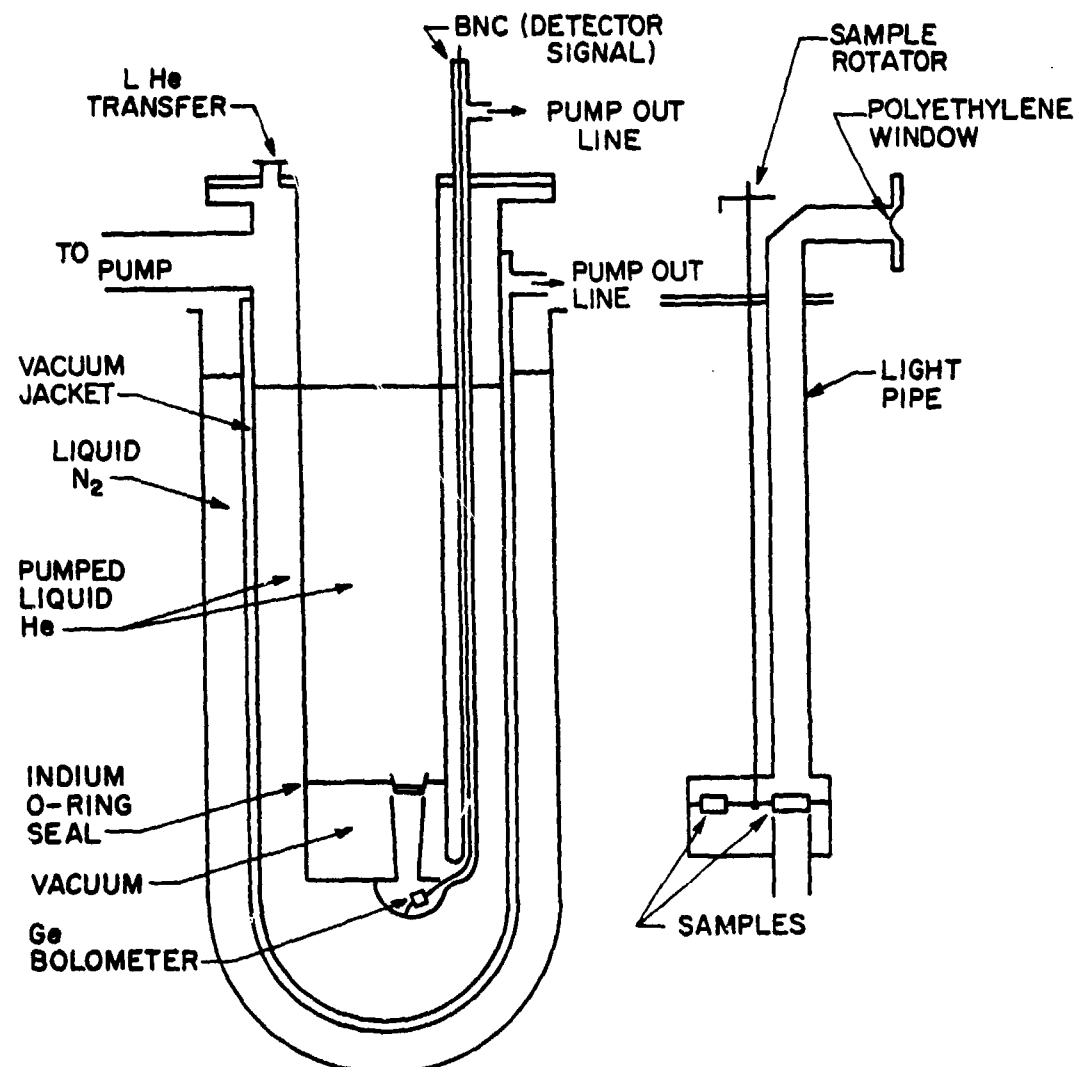


Figure III-17. Cold finger cryostat. The sample is mounted on a copper cold finger which is attached to a LN₂ bath.

Brewster's angle. No cold windows are required in this type of cryostat. A 1000- Ω Allen-Bradley resistor attached to the cold finger measures the temperature of the sample holder. Another resistor can be attached directly to the sample if necessary. Two additional ports oriented at right angles to the other two windows can be used to do crossed-beam experiments as well as scattering experiments.

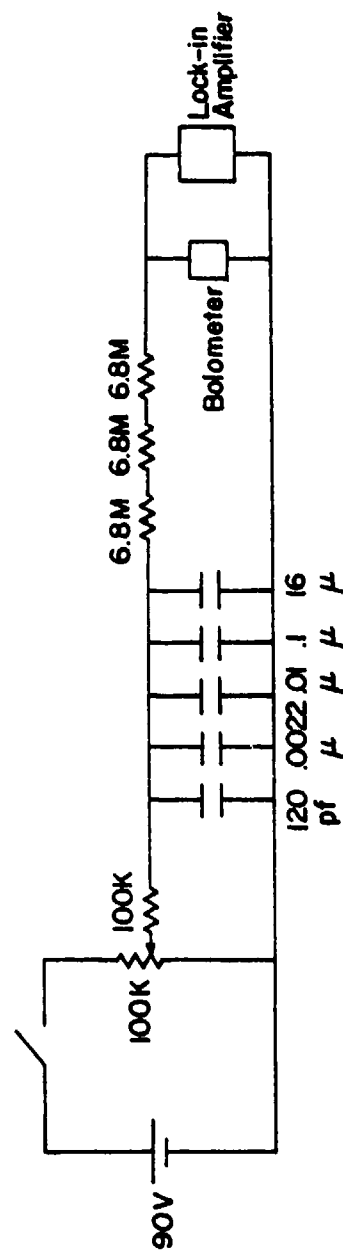
c. Far Infrared Cryostat

A 1.2K detector-cryostat system with light pipe optics is used to make transmission measurements in the far infrared. Figure III-18 shows a schematic diagram of the cryostat and sample holder. Far infrared radiation from a Michelson interferometer or from a far infrared laser travels along the light pipe, through the sample, through a Ge vacuum window and into the detector chamber where it is absorbed by a 1.2K Ge bolometer. The detector has a resistance of about 1 M Ω at 1.2K and has a sensitivity of approximately 10^4 V/W with an NEP of about 10^{-12} W/Hz. The detector bias circuit schematic is shown in Figure III-19. Slits cut in the walls between the sample chamber and the liquid He bath can be left open or soldered closed, thereby allowing the samples to be immersed in pumped liquid He for 1.2K measurements or run in He exchange gas for temperature dependent measurements. The 4-position sample rotator ring has a heater and a 1000- Ω Allen-Bradley resistor for temperature dependent measurements.



1.2 K BOLOMETER CRYOSTAT AND SAMPLE INSERT

Figure III-18. 1.2K Bolometer cryostat and sample insert. A four-opening sample wheel inserts into a helium bath. The FIR radiation passes through the samples and into the detector chamber where it is absorbed by a Ge bolometer.



BIAS CIRCUIT FOR 1.2K Ge BOLOMETER

Figure III-19. Bias circuit for 1.2K Ge bolometer.

D. Interferometry and Raman Spectroscopy

1. Apparatus

The internal modes of vibration of ReO_4^- impurity molecules in alkali were studied by means of infrared absorption spectroscopy and Raman scattering. The infrared active modes near 340 cm^{-1} and 920 cm^{-1} were probed using Fourier-transform Michelson interferometers and helium-cooled detectors. The low frequency mode was studied using the Michelson interferometer described in reference 44 and a 1.2 K Ge bolometer detector described in the previous section. The high frequency mode was studied using the IF-3 Michelson interferometer^{34,35} and a Ge:Cu detector.

All four internal modes of ReO_4^- are Raman active which makes Raman scattering especially useful. The Raman scattering data were gathered in a conventional Raman spectrometer as shown in Figure III-20. A Coherent Radiation-CR3 argon ion laser irradiates the sample. The right-angle scattered radiation passes through a double monochromator and photon-counting techniques are used to detect the transmitted radiation. The data is digitized and is stored on paper tape. Data processing is done on a PDP 11 mini-computer. The dark noise level is approximately 2-3 counts/sec while signal levels are typically greater than several hundred counts/sec on the Raman active lines of our samples.

2. Results

a. Infrared Absorption

The infrared absorption of ReO_4^- molecules in three different host crystals (KI, RbI, and KBr) was studied. Thick samples with fairly high dopant concentrations were studied to enhance any potential weak structure that otherwise might go unnoticed. The infrared absorption spectra of the

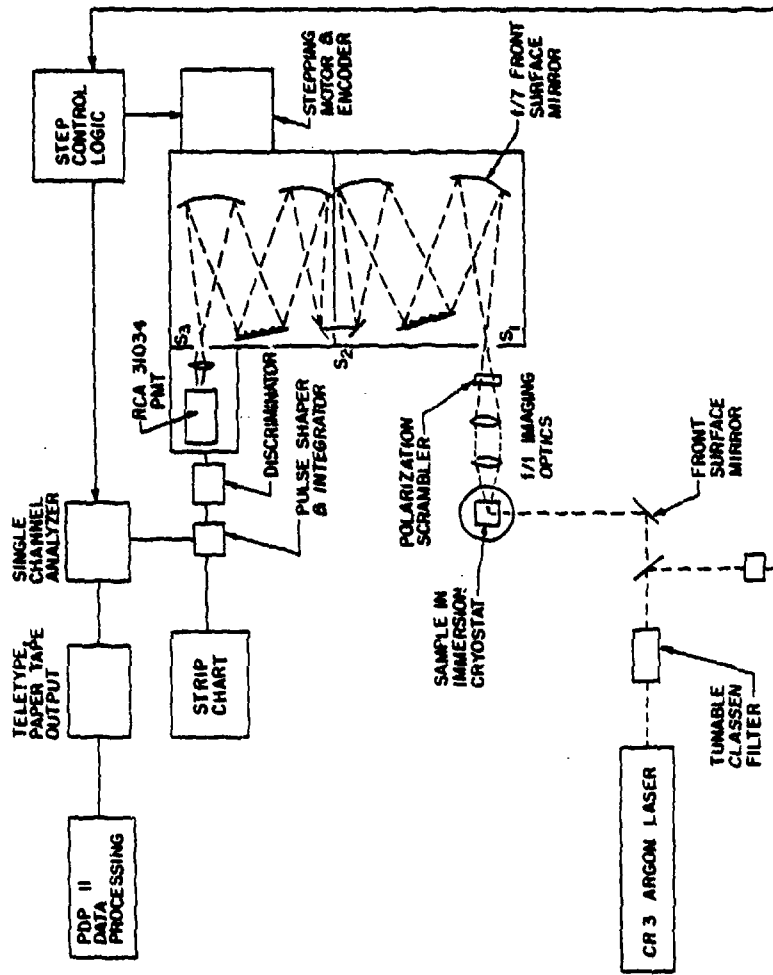


Figure III-20. Schematic diagram of Raman spectrometer in D. Fitchen's laboratory.

ν_4 internal mode of ReO_4^- in KBr, KI, and RbI hosts at 1.2 K are shown in Figures III-21 - III-23 respectively. The most striking similarities and differences in these spectra are the abundance of absorption lines in the KI and RbI samples and the total absence of such structure in the KBr sample. The ν_3 internal mode absorptions display similar behavior as shown in Figures III-24 - III-26. This type of absorption behavior indicates that the ReO_4^- has some motional degrees of freedom (e.g. libration) in the large KI and RbI lattice sites whereas in the smaller KBr lattice the ReO_4^- impurities are locked in one position with very little motional deviation. Direct low frequency (down to $\sim 5 \text{ cm}^{-1}$) infrared absorption by the KI and RbI samples was not observed but this is not such a surprising results when one remembers that the ReO_4^- molecule does not possess a permanent dipole moment. Therefore, if the librations (or any other motion the molecule might undergo) do not change the dipole moment of the ReO_4^- molecules they will not give rise to any infrared absorption.

Both $\text{KI} + \text{ReO}_4^-$ and $\text{RbI} + \text{ReO}_4^-$ have unidentified absorptions near their ν_3 absorptions. $\text{KI} + \text{ReO}_4^-$ has an absorption 82.4 cm^{-1} above the ν_3 absorption and $\text{RbI} + \text{ReO}_4^-$ has an absorption 93.9 cm^{-1} above the main line. Both these absorptions are sum processes* but, unfortunately, we have as yet not determined what gives rise to these resonances. None of the phonon energies match these values** and we have not observed any

* At room temperatures the difference processes were observed 82.4 cm^{-1} and 93.9 cm^{-1} below the main peak. These absorptions were obviously frozen out at 1.3 K.

** The transverse and longitudinal optic phonons in KI have frequencies $\nu_t = 101 \text{ cm}^{-1}$ and $\nu_l = 139 \text{ cm}^{-1}$ and in RbI their values are $\nu_t = 75 \text{ cm}^{-1}$ and $\nu_l = 103 \text{ cm}^{-1}$ respectively.⁴

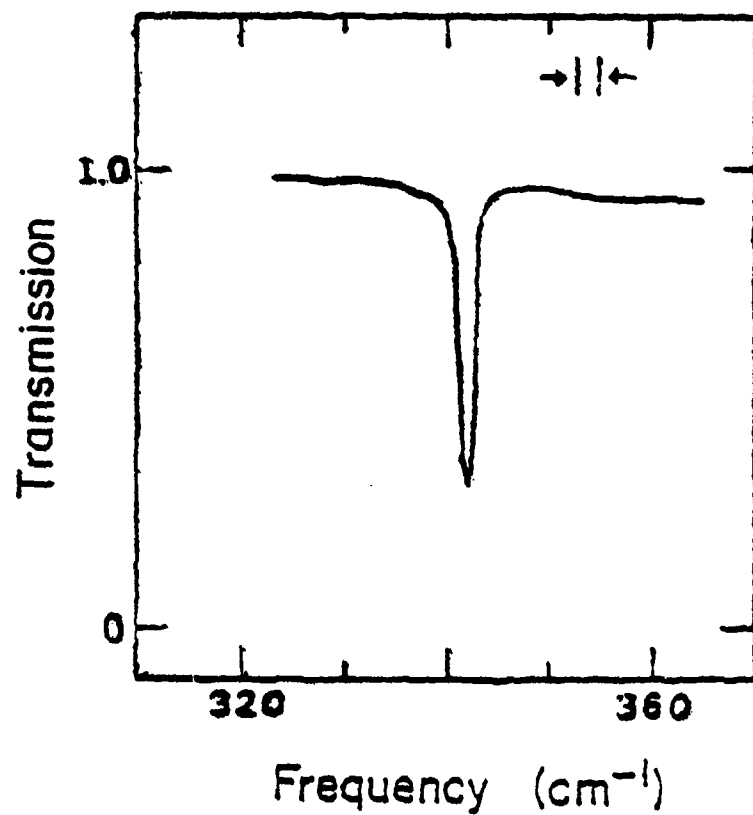


Figure III-21. Transmission spectrum of 1-inch KBr + .6% KReO₄ sample at 1.2 K in the region of the ν_2 vibration of ReO₄⁻. The resolution of the spectrum is shown by the arrows.

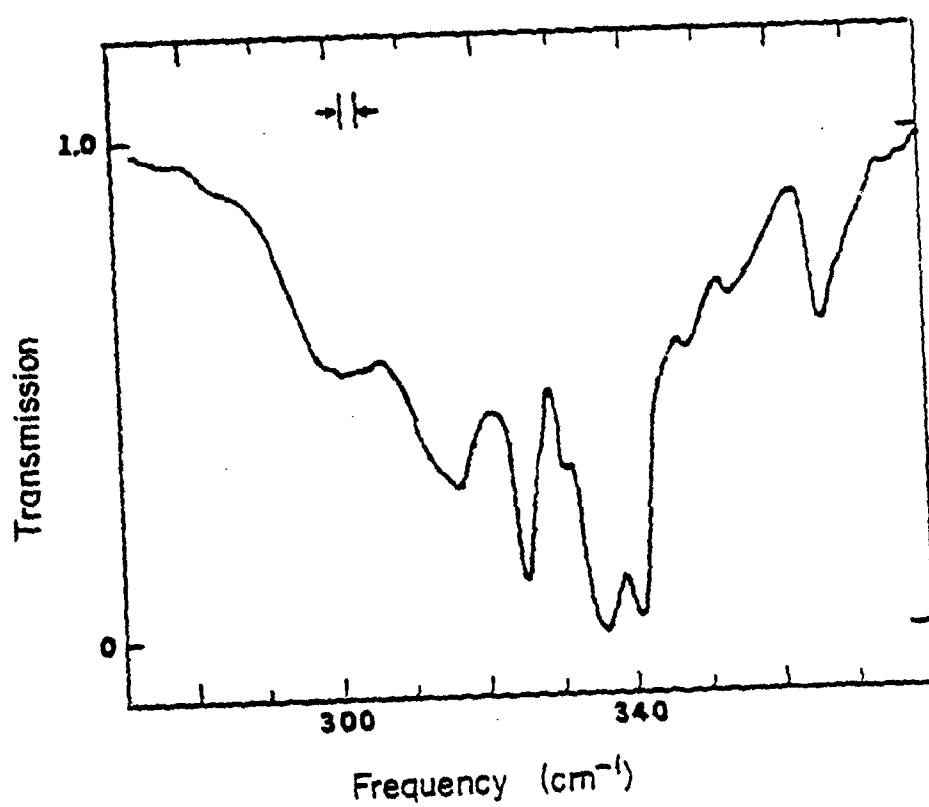


Figure III-22. Transmission spectrum of .74-inch KI + .4% KReO₄ sample at 1.2 K in the region of the ν_2 vibration of ReO₄⁻. The resolution of the spectrum is shown by the arrows.

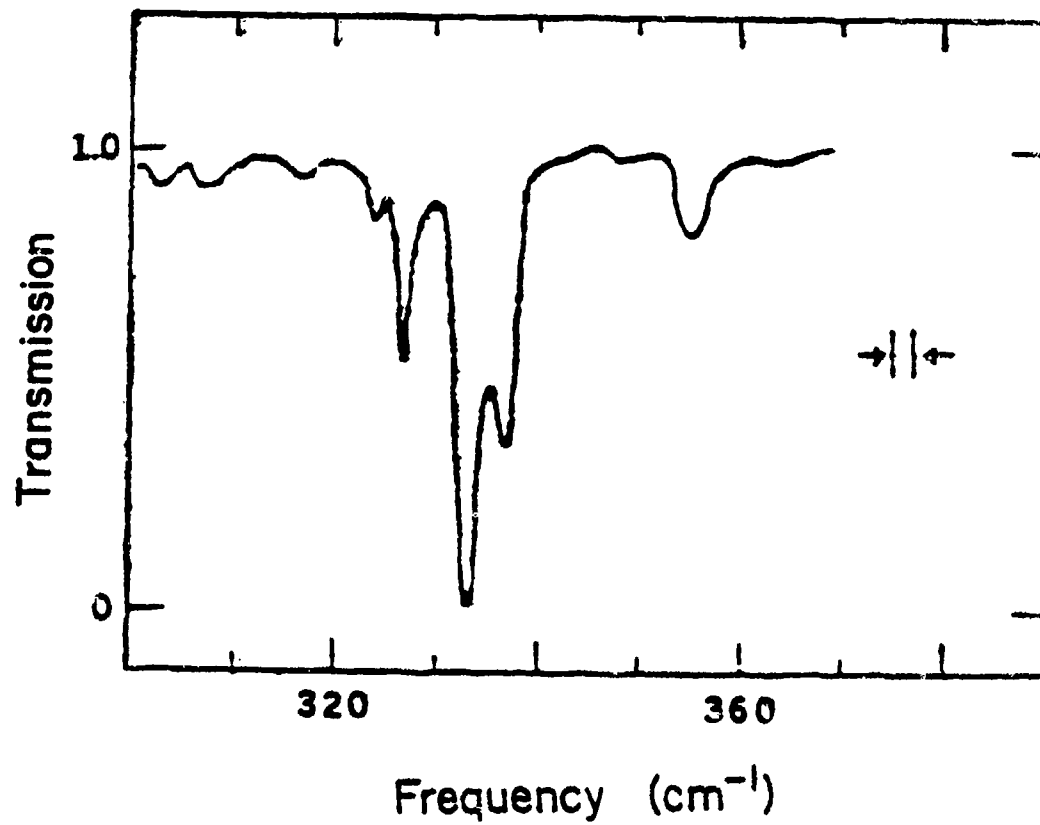


Figure III-23. Transmission spectrum of .66-inch RbI + .8% KReO₄ sample at 1.2 K in the region of the ν_2 vibration of ReO₄⁻. The resolution of the spectrum is shown by the arrows.

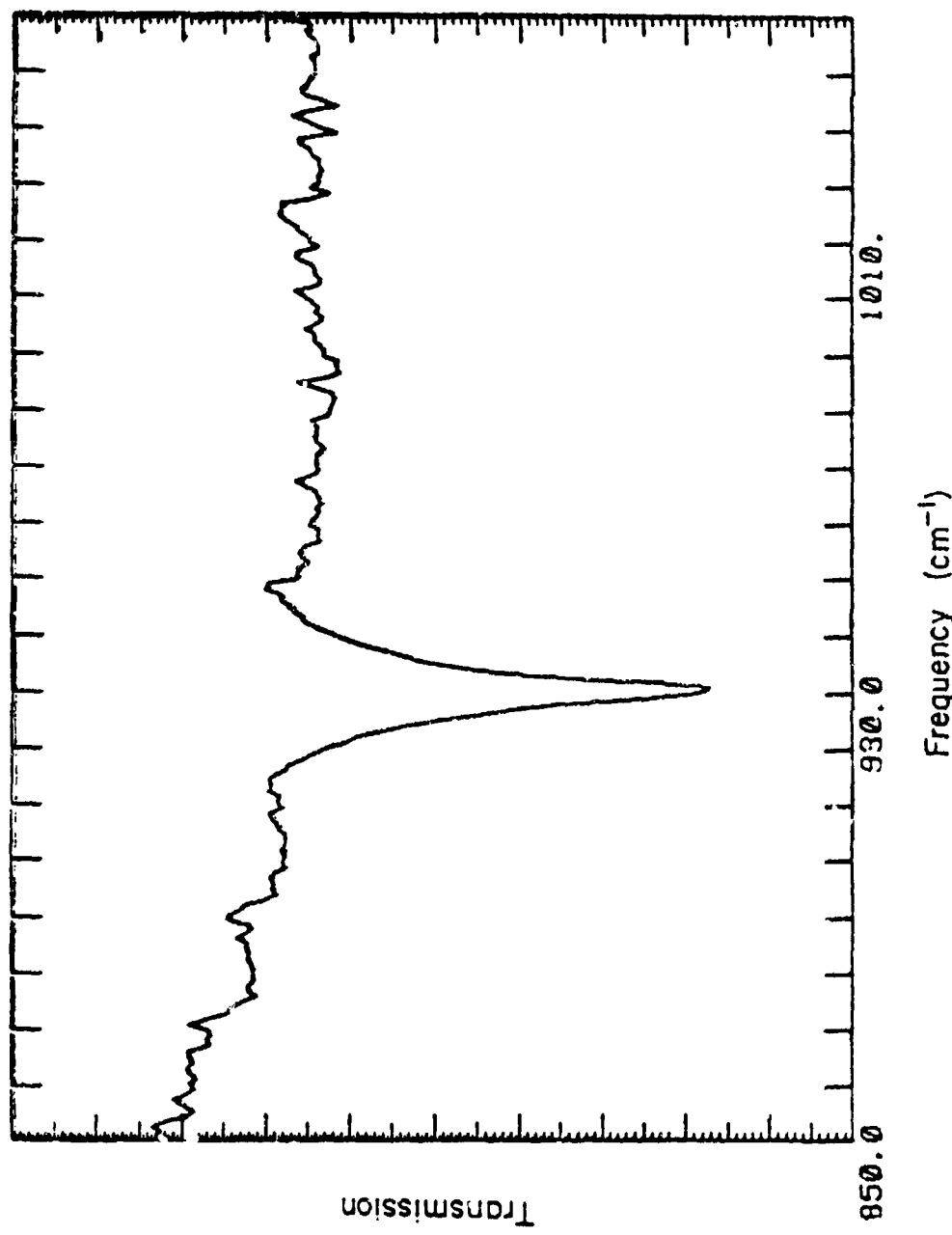


Figure III-24. Transmission spectrum of .5-inch KBr + .4₁₀ KReO₄ sample at 1.3 K in the region of the ν_3 vibration of ReO₄⁻.

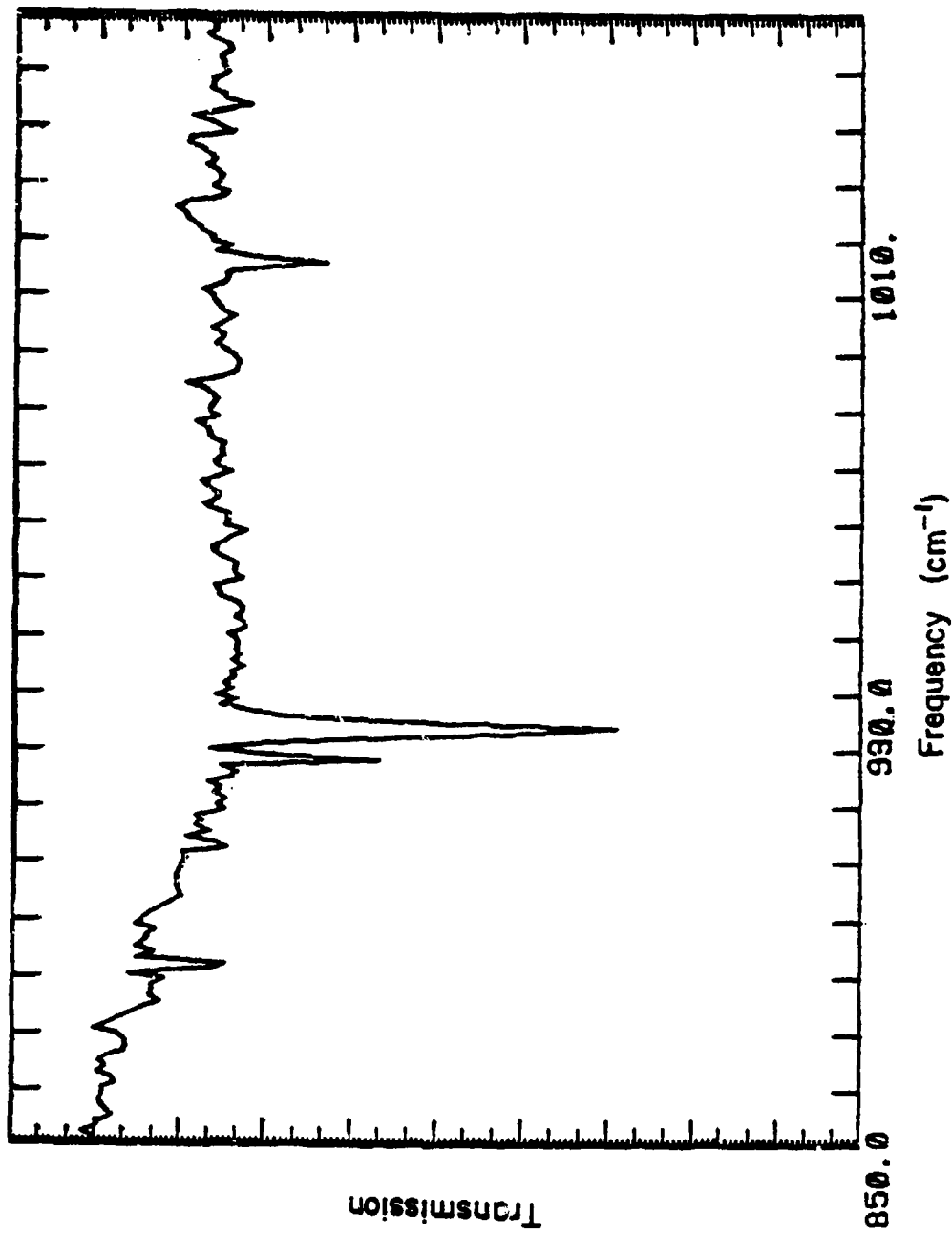


Figure III-25. Transmission spectrum of .7-inch KI + .3% KReO₄ sample at 1.3 K in the region of the ν_3 vibration of ReO₄⁻.

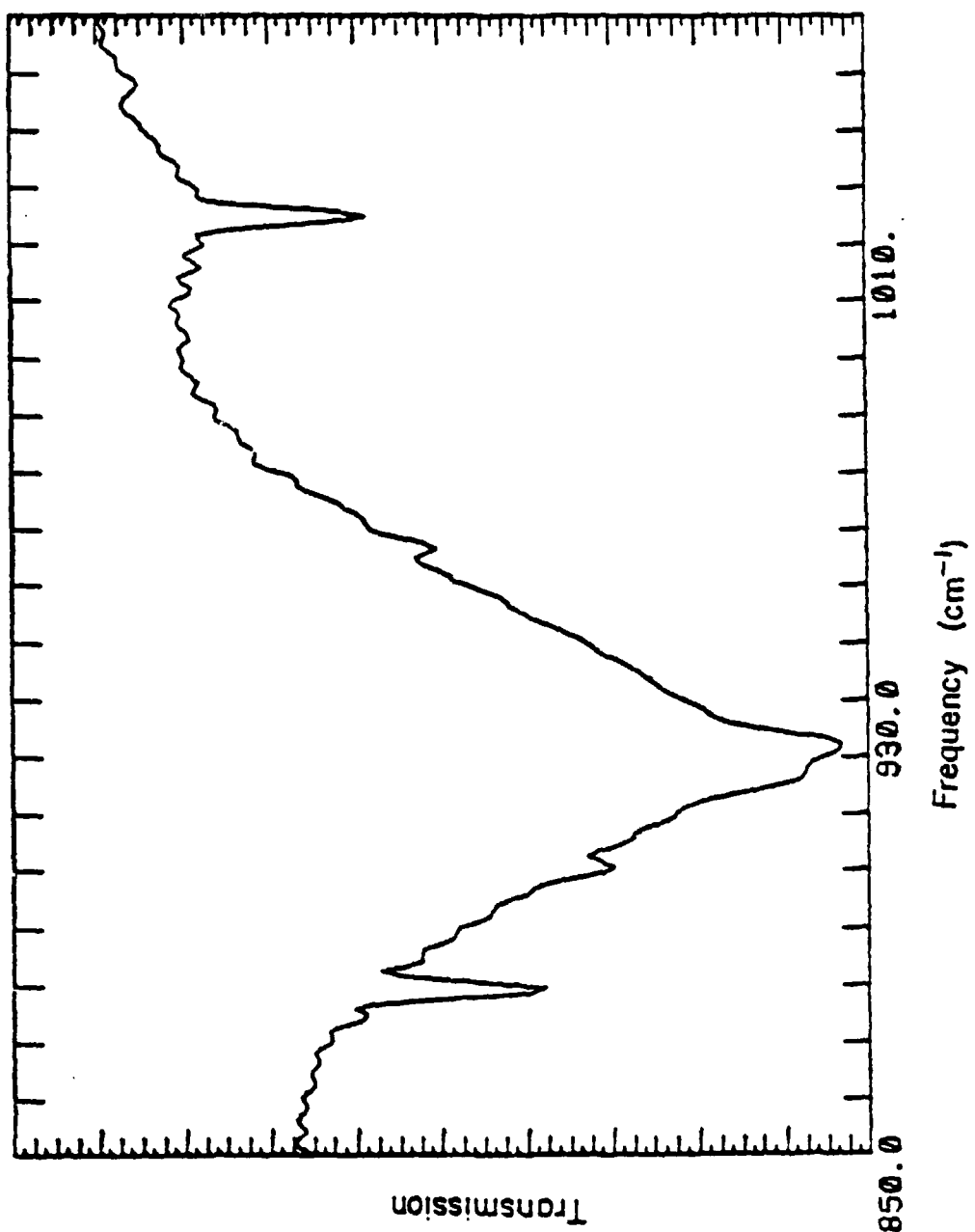


Figure III-26. Transmission spectrum of .7-inch RbI + .8% K ReO_4^- sample at 1.3 K in the region of the ν_3 vibration of ReO_4^- .

resonances at 82.4 cm^{-1} or 93.9 cm^{-1} in either infrared absorption or Raman scattering.

Another prominent resonance in both KI and RbI spectra that has not been identified appears 41.6 cm^{-1} below the main ν_3 line in KI and 40.3 cm^{-1} below the ν_3 resonance in Rb. The strength of these lines as well as their shift from the main peak cannot be explained by isotope effects. Obviously there are some quite complicated absorption mechanisms still to be understood.

b. Raman Scattering

The Raman scattering experiments were started in hope of clarifying some of the infrared measurements. It was conjectured that the various "extra" absorptions in the vicinity of the ν_3 and ν_4 modes were not observed directly in the far infrared because they were not infrared active but were perhaps Raman active.

Unfortunately additional Raman resonances besides the four internal modes were not observed. This does not preclude the existence of such resonances for the following reasons. Extremely low frequency resonances would be well into the Rayleigh tail and hence unobservable (perhaps with a triple monochromator such features would be observable). Weak higher frequency structure ($\approx 240 \text{ cm}^{-1}$) would be masked by the sizeable two-phonon signal from the host lattice. Therefore, these experiments do not rule out the existence of Raman active resonant modes and they have not shed any light on the extra absorption observed in the infrared experiments.

The Raman scattering experiments did produce two interesting pieces

of data. First of all, the position of all the internal modes of the ReO_4^- molecule in KI and RbI were measured (these will be tabulated later in this section). Perhaps even more interesting is the information obtained about the ν_2 and ν_4 modes of ReO_4^- (Figure III-27). In 1953 Claassen and Zielen⁴⁵ measured the Raman spectrum of essentially free ReO_4^- molecules and observed only one low frequency mode at 331 cm^{-1} . This led them to conjecture that the ν_2 and ν_4 modes were accidentally degenerate. Our measurements indicate that the ν_2 and ν_4 modes of ReO_4^- molecules in solid matrices are not degenerate. In KI at room temperature ν_2 occurs at 341.2 cm^{-1} and ν_4 at 335 cm^{-1} . In RbI ν_2 is at 336.2 cm^{-1} and ν_4 at 330 cm^{-1} . An attempt to repeat these measurements in solution failed because of high fluorescence levels. It should be pointed out that ν_2 and ν_3 have opposite temperature behaviors: the frequency of ν_4 increases. In KI at 8 K the two modes are separated by only 1.8 cm^{-1} . The signal-to-noise in these experiments was not high enough to enable us to study any interaction between the two modes as they moved toward each other at low temperatures.

Summary

The infrared and Raman lines of ReO_4^- in KI, RbI, and KBr lattices were studied and the positions of these lines are listed in Table III-2. The infrared spectrum of KBr + ReO_4^- has two sharp absorptions corresponding to the ν_3 and ν_4 internal modes of ReO_4^- . The KI + ReO_4^- and RbI + ReO_4^- samples have complicated infrared spectra in the vicinity of the ν_3 and ν_4 absorptions of ReO_4^- . Many of these additional features (some of which are sidebands of the main absorption lines) have not been

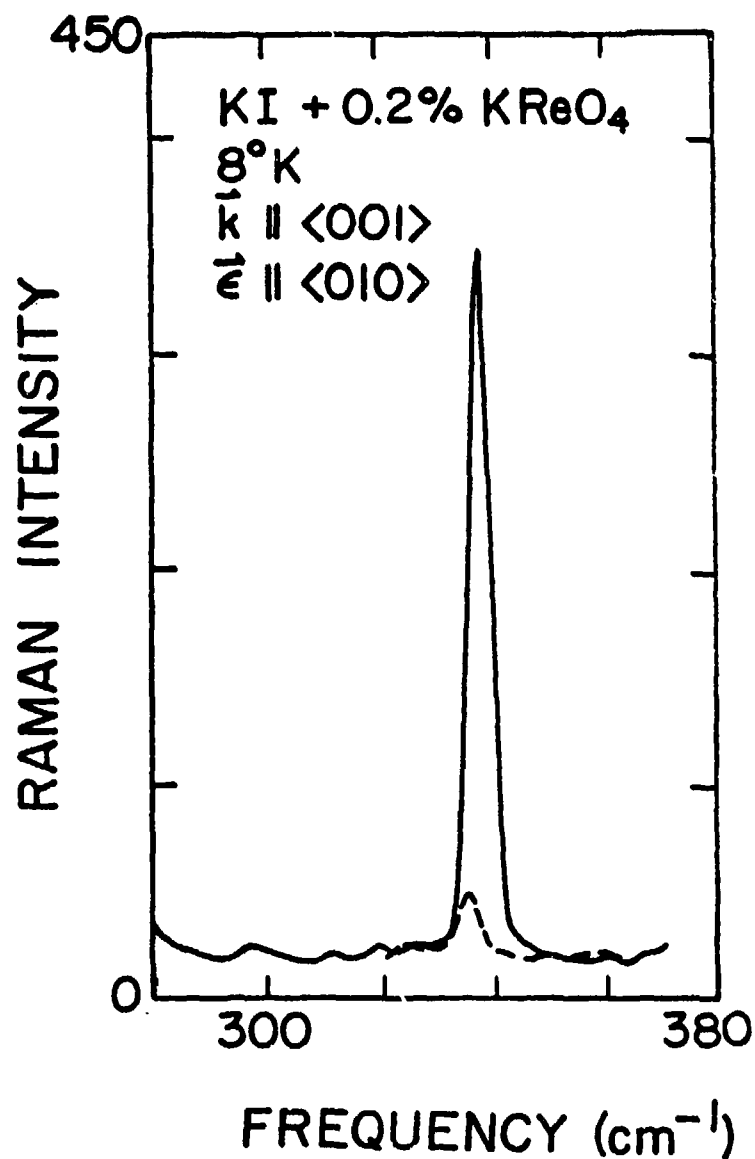


Figure III-27. Raman spectrum of KI + .2% ReO₄⁻ at 8 K. The incident beam is polarized along the <010> direction. The right-angle-scattered beam is analyzed by a polarizer set parallel to the <010> direction (solid curve) to detect the even-symmetry mode ν_2 . To detect the odd-symmetry mode ν_4 the polarizer is set parallel to the <001> direction.

Table III-2

Infrared and Raman Lines of ReU_4^- in KBr, KI, and Kbl
 The center frequency of each line is followed by an (R) if observed in Raman scattering and by an (I) if observed by infrared absorption.

| Host Lattice | Vibrational Mode | Center Frequency (cm^{-1}) | | |
|--------------|------------------|---------------------------------------|----------|----------|
| | | 300 K | 77 K | 8 K |
| KBr | ν_3 | | | 931.4(I) |
| | ν_4 | | | 342.1(I) |
| KI | ν_1 | 966.8(R) | 964.3(R) | 964.4(R) |
| | ν_2 | 341.2(R) | 337.6(R) | 337.4(R) |
| | ν_3 | 922 (R) | 922.5(R) | 922.8(R) |
| | | 922 (I) | | 923.7(I) |
| Unidentified | | 881.4(I) | | 918.4(I) |
| | ν_4 | 334.4(R) | 334.5(R) | 335.6(R) |
| Unidentified | | | | 335.2(I) |
| | | | | 325.3(I) |
| | | | | 300 (I) |
| | | | | 313.3(I) |
| | | | | 331.6(I) |
| | | | | 340.7(I) |
| | | | | 367.6(I) |
| | | | | 420.5(I) |

Table III-2 (continued)

| Host Lattice | Vibrational Mode | Center Frequency (cm^{-1}) | | |
|--------------|------------------|---------------------------------------|----------|-----------|
| | | 300 K | 77 K | 8 K |
| RbI | ν_1 | 967 (R) | 965 (R) | |
| | ν_2 | 336.2(R) | 338 (R) | |
| | ν_3 | 921.4(R) | 922.1(R) | |
| | | 919.3(1) | | 920.5(1) |
| | Unidentified | 830.1(1) | | |
| | | 1008.5(1) | | 1014.4(1) |
| | | 978.4(1) | | 879.2(1) |
| | | | | 956.3(1) |
| | | | | 900.7(1) |
| | | | | 720 (1) |
| | | | | 568.5(1) |
| | ν_4 | 330 (R) | 334.6(R) | |
| | Unidentified | | | 333.5(1) |
| | | | | 327.3(1) |
| | | | | 333.5(1) |

identified. None of the sideband absorptions were observed directly in the far infrared region. Raman scattering also showed no additional absorptions besides the four internal modes absorptions, but did show conclusively that the ν_2 and ν_4 modes of ReO_4^- in alkali halides are not degenerate.

E. Theory of Incoherent Saturation

Saturation effects can be divided into two distinct classes: coherent saturation and incoherent saturation or incoherent bleaching. Coherent saturation effects include optical nutation, self-induced transparency, and photon echoes and can be observed only if the interaction time between the resonant radiation field and absorbers is less than both T_1 and T_2 (the various relaxation times will be explained shortly). The theoretical treatment of coherent saturation phenomena involves solutions of the optical Bloch equations which are merely extensions of the Bloch spin vector formalism used in NMR. A comprehensive treatment of the optical Bloch equations and their solutions is given by Allen and Eberly.⁴⁶

Incoherent saturation effects in general are much more easily observed because there is no restriction on interaction times and, in fact, many incoherent bleaching phenomena occur over times much longer than both T_1 and T_2 . The theory of incoherent saturation is simpler than the Bloch theory because coherence in the interaction between radiation and absorber can be ignored. The propagation of radiation through a saturable absorber can be described by means of rate equations which can be solved numerically or analytically depending on the conditions of the absorber and the radiation. A steady state solution exists in closed form for cases in which τ (laser pulse width) is much longer than both T_1 and T_2 . The solution differs for homogeneously and inhomogeneously broadened lines. A "dynamic" solution to the rate equations can be obtained numerically. Such solutions are not based on any assumptions

regarding laser pulse widths and decay times within the sample. The price of such a general solution is the numerical analysis as opposed to closed form solutions. Both types of solutions will be discussed in the following sections.

1. Phenomenological Decay Constants

In the discussion of problems associated with resonant interactions between fields and matter (whether it be NMR or optical interactions of laser radiation with an absorbing medium) there are several decay times that are important. Assume for simplicity that the system under consideration consists of two levels, a ground state and an excited state, separated by energy E , and that "absorbers" in the ground state can be excited to the upper level by means of an external radiation field (e.g. laser radiation). After the absorbers are coherently excited to the upper level there are several possible "decay mechanisms". The absorbers can decay back to the ground state by giving up energy E . The decay time associated with this is T_1 . However, before decaying to the ground state the coherence of the upper level can be destroyed by collisions (in a gas) or phonon scattering (in a solid). These interruptions in phase can occur without disturbing the energy of the absorbers in the upper level. The decay time of the coherence of the upper level is T_2' . There are two contributions to T_2' , a homogeneous decay time T_2 and an inhomogeneous time T_2^* . T_2 is associated with interactions that affect all atoms homogeneously such as collisions (phonon scattering), radiative decay, impurity-impurity interaction. T_2^* is most commonly associated with the Doppler effect in gases or random local strain fields

in solids. The relation between T_2' , T_2 , and T_2^* is

$$\frac{1}{T_2'} = \frac{1}{T_2} + \frac{1}{T_2^*} .$$

2. Rate Equation Theory of Saturation

a. Steady State Solution for Homogeneously Broadened Lines

Assume molecular impurity absorption in a lattice can be approximated by a two-level system consisting of a ground state $|0\rangle$ with degeneracy g_0 separated by $\hbar\omega_0$ from an excited state $|1\rangle$ with degeneracy g_1 . The system is irradiated by a pulsed laser source of photons of frequency ω and pulse width τ . The rate equations describing this situation are

$$\frac{dN_0}{dt} = W_{10}N_1 - W_{01}N_0 + N_1/T_1 \quad (1)$$

$$\frac{dN_1}{dt} = -W_{10}N_1 + W_{01}N_0 - N_1/T_1 \quad (2)$$

$$\frac{dI(z,t)}{dt} = (W_{10}N_1 - W_{01}N_0)\hbar\omega \quad (3)$$

where

N_0 = concentration of absorbers in the ground state

N_1 = concentration of absorbers in the excited state

$N_{tot} = N_0 + N_1$ = total concentration of absorbers (4)

T_1 = decay time of absorbers from state $|1\rangle$ to state $|0\rangle$

$I(z,t)$ = laser intensity at position z in sample (energy/sec-cm²)

$W_{01} = g_1 \frac{4\pi^2}{\hbar c} |\mu_{01}|^2 I g(\omega - \omega_0)$ = induced transition rate from $|0\rangle$ to $|1\rangle$

$W_{10} = g_0 \frac{4\pi^2}{\hbar c} |\mu_{01}|^2 I g(\omega - \omega_0)$ = induced transition rate from $|1\rangle$ to $|0\rangle$

μ_{01} = transition dipole moment

$$g(\omega - \omega_0) = \frac{T_2^{-1}}{\pi[(\omega - \omega_0)^2 + T_2^{-2}]} = \text{normalized Lorentz lineshape function}$$

T_2 = homogeneous coherence time of excited state.

If $T_1 \ll \tau$ we can assume that the system is in steady state during the laser pulse. This assumption is equivalent to

$$\frac{dN_0}{dt} = \frac{dN_1}{dt} = 0 .$$

Then Eqs. (1) and (4) imply that

$$N_1 = \frac{W_{01} T_1 N_{\text{tot}}}{1 + W_{01} T_1 (1 + g_0/g_1)} \quad (5)$$

Using Eqs. (4) and (5) to eliminate N_0 and N_1 from Eq. (3) yields

$$\frac{dI}{dz} = \frac{-\hbar\omega W_{01} N_{\text{tot}}}{1 + W_{01} T_1 (1 + g_0/g_1)} \quad (6)$$

Eq. (6) may be rewritten

$$\frac{dI}{dz} = \frac{-\alpha I}{1 + WI} \quad (7)$$

where

$$\alpha = \hbar\omega W_{01} N_{\text{tot}}/I = \text{low intensity absorption coefficient due to impurities} \quad (8)$$

$$W = \frac{W_{01} T_1 (1 + g_0/g_1)}{I} = \frac{T_1 \sigma (1 + g_0/g_1)}{\hbar\omega} = \text{saturation parameter}$$

(sometimes referred to as $1/I_s$, where I_s = saturation intensity) (9)

$$\sigma = \alpha/N_{\text{tot}} = \text{cross section of impurity to laser radiation.} \quad (10)$$

Eq. (9) yields

$$T_1 = \frac{W \tau_w}{\sigma(1 + g_0/g_1)} \quad (11)$$

Therefore, by determining σ and W we can calculate the excited state lifetime of the impurities. Note that if the impurities were embedded in a lattice which had an appreciable absorption coefficient α_L at the laser frequency, then Eq. (6) would be changed to

$$\frac{dI}{dz} = -(\alpha_L + \frac{\alpha}{1 + WI})$$

However, the host lattices used in our experiments are all alkali halides which have negligible absorption coefficients ($\alpha_L < 10^{-3} \text{ cm}^{-1}$) at CO_2 laser frequencies and therefore Eq. (6) need not be modified.

There are two ways to determine W . One involves measuring the threshold saturation intensity and setting

$$WI_{th} \sim 1 .$$

Then

$$W \sim 1/I_{th} .$$

The other technique is perhaps more accurate and involves making a measurement of sample transmissivity at some intensity greater than the threshold intensity. Eq. (7) can be integrated to give

$$\ln \frac{I_{out}}{I_{in}} + W(I_{out} - I_{in}) = -\alpha L$$

where

I_{in} = input laser intensity

I_{out} = transmitted laser intensity

L = length of sample.

Let $T = I_{out}/I_{in}$ = intensity-dependent transmission through the sample and $T_0 = e^{-\alpha L}$ = low intensity transmission through the sample. Then

$$W = \frac{\ln T/T_0}{I_{in}(1 - T)} \quad (12)$$

W can be determined by measuring T_0 , T , I_{in} and using Eq. (12). Once the saturation parameter is known, the excited state lifetime T_1 can be determined from Eq. (11).

b. Steady State Solution for Inhomogeneously Broadened Lines

The derivation of the functional form of $\frac{dI}{dz}$ for an inhomogeneously broadened absorber is slightly more complicated than for a homogeneously broadened system because there are two lineshape functions to take into account. In the case of inhomogeneous broadening we consider the inhomogeneous line (with center frequency $= \omega_0$) as made up of various classes of absorbers labelled by the index ϵ . Each class is homogeneously broadened and has a normalized lineshape function $g(\omega - \omega_\epsilon)$ centered at ω_ϵ where

$$g(\omega - \omega_\epsilon) = \frac{T_2^{-1}}{\pi[(\omega - \omega_\epsilon)^2 + T_2^{-2}]}$$

The inhomogeneous lineshape function is denoted by $h(\omega - \omega_0)$ and is normalized in the conventional manner,

$$\int_{-\infty}^{\infty} h(\omega - \omega_0) d\omega = 1$$

The probability that an impurity molecule has a center frequency ω_ϵ is just $h(\omega_\epsilon - \omega_0)$. As in the homogeneous case (Eq. 6) we can write the attenuation of laser intensity with distance through the sample due to absorbers in class ϵ as

$$\left. \frac{dI}{dz} \right|_\epsilon = - \frac{\pi \omega W_{01}^\epsilon N_\text{tot}^\epsilon}{1 + (1 + g_0/g_1) W_0^\epsilon T_1} \quad (13)$$

But

$$N_{\text{tot}}^{\epsilon} = N_{\text{tot}} h(\omega_{\epsilon} - \omega_0)$$

and the total attenuation of laser radiation due to absorbers in all classes is

$$\frac{dI}{dz} = -\hbar\omega N_{\text{tot}} \int_{-\infty}^{\infty} \frac{w_{01}^{\epsilon} h(\omega_{\epsilon} - \omega_0) d\omega_{\epsilon}}{1 + (1 + g_0/g_1) w_{01}^{\epsilon} T_1} \quad (14)$$

w_{01}^{ϵ} can be written as

$$w_{01}^{\epsilon} = g_1 \frac{4\pi^2}{\hbar^2 c} |\mu_{01}|^2 I \frac{1}{\pi T_2 [(\omega - \omega_{\epsilon})^2 + T_2^2]} \quad (15)$$

Substituting Eq. (15) into Eq. (14) gives

$$\frac{dI}{dz} = -\hbar\omega N_{\text{tot}} g_1 \frac{4\pi^2}{\hbar^2 c} |\mu_{01}|^2 \frac{I}{\pi T_2} \int_{-\infty}^{\infty} \frac{h(\omega_{\epsilon} - \omega_0) d\omega_{\epsilon}}{(\omega - \omega_{\epsilon})^2 + \frac{1}{T_2^2} + g_1 \frac{4\pi |\mu_{01}|^2}{\hbar^2 c T_2} I T_1 (1 + g_0/g_1)} \quad (16)$$

In the case of extreme inhomogeneous broadening $h(\omega_{\epsilon} - \omega_0)$ is essentially constant over the region near $\omega_{\epsilon} = \omega$ where the integrand goes through a maximum. For this case we can pull $h(\omega - \omega_0)$ through the integral.

The remaining integral has the form

$$\int_{-\infty}^{\infty} \frac{dx}{x^2 + a^2} = \frac{\pi}{a}$$

Performing the integration we have

$$\frac{dI}{dz} = -\hbar\omega N_{\text{tot}} g_1 \frac{4\pi^2}{\hbar^2 c} |\mu|^2 I h(\omega - \omega_0) \sqrt{\frac{1}{1 + g_1 \frac{4\pi |\mu|^2 I (1 + g_0/g_1) T_1 T_2}{\hbar^2 c}}} \quad (17)$$

$$\frac{dI}{dz} = \frac{-\alpha I}{\sqrt{1 + WI}} \quad (18)$$

where

$$\alpha = -\pi \omega N_{tot} W_{01}^i / I \quad (19)$$

$$W = g_1 \frac{4\pi |\mu_{01}|^2}{\pi c^2} (1 + g_0/g_1) T_1 T_2 \quad (20)$$

$$W_{01}^i = g_1 \frac{4\pi^2}{\pi c^2} |\mu_{01}|^2 I h(\omega - \omega_0) \quad (21)$$

It is instructive to compare the functional forms of $\frac{dI}{dz}$ for homogeneously and inhomogeneously broadened absorbers (Eq. 18 and Eq. 7). Note that an inhomogeneous line saturates more slowly than a homogeneous line because although individual classes of absorbers saturate as $(1 + WI)^{-1}$ the number of classes which are affected (or, in other words, the "hole" width) is proportional to $(1 + WI)^{\frac{1}{2}}$. For more in-depth discussion of this point, see reference 47.

Notice from Eq. (20) that even if W is determined experimentally we need to know T_2 as well as $|\mu|^2$ to determine T_1 . As in the case of homogeneously broadened lines W can be determined from the threshold saturation intensity

$$W \sim 1/I_{th} .$$

The second technique for determining W (integration of the expression for $\frac{dI}{dz}$) is less satisfactory for inhomogeneous lines.

$$\int_{I_{in}}^{I_{out}} \frac{\sqrt{1 + WI}}{I} dI = - \int_0^L \alpha dz$$

$$-2(\tanh^{-1} \sqrt{1 + WI}_{out} - \tanh^{-1} \sqrt{1 + WI}_{in}) = -\alpha L$$

This gives a transcendental equation for W with no closed form solution and therefore numerical analysis is needed to solve for W .

c. Dynamic Solution

Using Eqs. (8) and (10) we can rewrite Eqs. (2) and (3) as

$$\frac{dN_1}{dt} = \frac{I\sigma}{\hbar\omega} (N_{\text{tot}} - [1 + g_0/g_1]N_1) - N_1/T_1 \quad (22)$$

$$\frac{dI}{dz} = -\sigma I(N_{\text{tot}} - [1 + g_0/g_1]N_1) \quad (23)$$

Eliminating N_1 from these equations yields

$$\frac{d^2(\ln I)}{dt dz} + \left(\frac{g_0+g_1}{g_1}\right) \frac{\sigma}{\hbar\omega} \frac{dI}{dz} + \frac{1}{T_1} \frac{d(\ln I)}{dz} + \frac{\sigma N_{\text{tot}}}{T_1} = 0 \quad (24)$$

Assuming that the operators $\frac{d}{dt}$ and $\frac{d}{dz}$ commute Eq. (24) can be integrated with respect to z

$$\frac{d(\ln I)}{dt} + \left(\frac{g_0+g_1}{g_1}\right) \frac{\sigma}{\hbar\omega} I + \frac{\ln I}{T_1} + \frac{\sigma N_{\text{tot}} z}{T_1} = c_0 + c_1(t) \quad (25)$$

The constants of integration $c_0 + c_1(t)$ can be evaluated by applying boundary conditions at the input face of the sample. If the laser produces pulses $L(t)$ then

$$I(z=0, t) = L(t)$$

and Eq. (25) becomes

$$\frac{d(\ln L)}{dt} + \left(\frac{g_0+g_1}{g_1}\right) \frac{\sigma}{\hbar\omega} L + \frac{\ln L}{T_1} = c_0 + c_1(t) \quad (26)$$

Eq. (25) may then be rewritten as

$$\frac{d(\ln I/L)}{dt} + \left(\frac{g_0+g_1}{g_1}\right) \frac{\sigma}{\hbar\omega} (I-L) + \frac{\ln I/L}{T_1} + \frac{\sigma N_{\text{tot}} z}{T_1} = 0 \quad (27)$$

We are interested in the radiation that is transmitted through the sample. Therefore in Eq. (27) set $z = l$ = length of sample and make the substitution

$$\sigma N_{\text{tot}} l = -\ln T_0$$

where T_0 is the low-power transmittance of the sample. Using

$$I/L = T(t)$$

where T is the time varying transmittance of the sample, Eq. (27) now reads

$$\frac{d \ln T}{dt} + \frac{\ln T}{T_1} = \left[\frac{g_0 + g_1}{g_1} \right] \frac{\sigma L(t)}{\hbar\omega} (1 - T) + \frac{\ln T_0}{T_1} \quad (28)$$

This equation can be solved numerically using the Runge-Kutta fourth-order rule provided σ is known. The Q-switched laser pulse shape $L(t)$ can be approximated by the function

$$L(t) = \frac{1}{2}L_0(1 - \cos Ct)$$

where

L_0 = peak intensity

$C = 2\pi/\text{full width of laser pulse}$

This is a reasonable approximation of a Q-switched pulse especially for laser lines far from the band centers. Experimental pulses transmitted through the sample are then compared to the computer generated pulses and a value of T_1 is obtained from the pulse that most closely resembles the experimental pulse (in magnitude, shape, and peak delay).

F. Absorption and Saturation Measurements

1. Experimental

A schematic diagram of the absorption and saturation experiments is shown in Figure III-28. The Apollo CO₂ laser is operated in the chopped, pulsed, Q-switched, or pulsed Q-switched mode depending on the experiment. A KCl beam splitter sends 10% of the beam to a reference detector which is either the Santa Barbara Ge:Cu detector or the Molelectron pyroelectric detector. The remaining 90% of the radiation passes through a (optional) PTR Optics polarizer which can be rotated to give a 130:1 variability in intensity at the sample. A 5-inch focal-length meniscus lens from II-VI Inc. focuses the radiation onto the sample to a spot approximately .02 cm in diameter with a depth of field of 7 mm (see Appendix V). For intrinsically low-intensity experiments such as absorption measurements the lens is removed and replaced by an iris. The sample is mounted in either the LN₂ cold-finger cryostat or the He immersion cryostat. The transmitted intensity is gathered by a 2.5-inch focal-length lens and softly focused onto T. Cool's Ge:Cu detector. The reference detector output was used to trigger a Tektronix 7704 oscilloscope and both the reference detector and the signal detector output could be displayed simultaneously.

The KBr measurements were made using the LN₂ cryostat and the KI measurements were made on samples mounted in the He cryostat. A 1000- Ω Allen-Bradley resistor was pressed against the sample to measure sample temperatures. A thin layer of Apiezon Z grease established thermal contact between resistor and sample. No temperature controller was used to change and maintain sample temperatures. We found that the sample

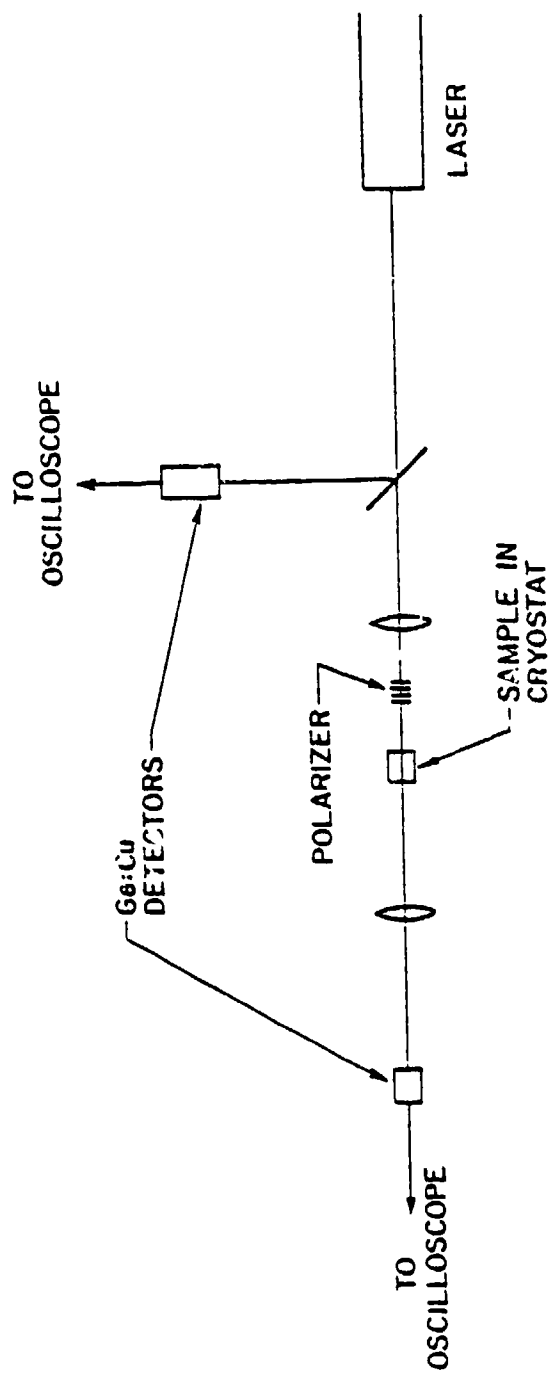


Figure III-28. Experimental arrangement for absorption and saturation measurements.

temperature (especially at temperatures above 20 K) changed very slowly and therefore it was possible to make the various measurements "on the fly". Laser intensities were always adjusted so that no sample heating could be observed (as measured by the 1000Ω resistor).

2. Sample Preparation

All the doped samples were taken from crystals grown by the Czochralski method. Samples greater than 1.5 mm thick were simply cleaved from the boules. Thinner samples could be obtained by cleaving but these samples tended to bend in the cleaving process. Therefore, samples thinner than 1.5 mm were prepared from thick pieces (1.5-2 mm). The samples were gently sanded on moist No. 600 sandpaper to the appropriate thickness and then were "etched" in distilled water for a second or two and then quickly dried. The surface thus obtained was smooth with a slight orange-peel finish similar to that described in Section II-D.

G. Results of Saturation and Excited State Lifetime Measurements

The ν_3 absorption of ReO_4^- impurities in two different lattices was measured using low laser powers and then saturated using Q-switched laser pulses and from these data the excited state lifetimes T_1 of the ν_3 vibration were determined. ReO_4^- molecules in a KBr matrix were studied at 100 K using the P(34) line (931 cm^{-1}) of the Apollo CO₂ laser. In a KI + .2% Cs⁺ matrix* the ReO_4^- transition was partially

*Cs⁺ ions were added to the crystal in order to increase the average lattice spacing which, in turn, displaces the center frequency of the ν_3 absorption to slightly lower frequency. This provided some overlap between the absorption resonance and the P(42) (00⁰1-10⁰0) line of a CO₂ laser even at 1.3 K.

or totally saturated between 300 K and 1.3 K using the P(42) (922.9 cm^{-1}) CO_2 laser line. The excited state lifetimes were determined in the following way. The low intensity transmission T_0 , the saturated transmission T , and the incident intensity I_{in} were measured and the saturation parameter W was calculated from Eq. (12) of Section E. The cross section σ was determined from α (which is determined from $\alpha = -(1/l)\ln T_0$ where l = sample thickness) and N_{tot} (which was determined by the Analytic Facility by means of neutron activation studies of the Re in the sample) using Eq. (10). Eq. (11) was then used to calculate T_1 ($g_0 = 1$, $g_1 = 3$ for the ground and v_3 excited state of ReO_4^- respectively). T_1 was also computed by numerically solving Eq. (28). For T_1 values much less than the width τ of the input laser pulses ($\sim 1 \mu\text{sec}$) the two calculations produced identical results. If T_1 , as calculated by Eq. (11), was comparable to or greater than τ this value was discarded (because this calculation technique assumes that $T_1 \ll \tau$) and T_1 was computed using Eq. (28). All the computed values of T_1 were calculated assuming the v_3 absorption was homogeneously broadened. This, however, is not the case at all temperatures; the effects of inhomogeneous broadening will be discussed shortly.

KBr Matrix

The absorption coefficient at 100 K of a KBr sample containing $5.7 \times 10^{19} \text{ ReO}_4^-$ molecules/cc is 36 cm^{-1} . Therefore, $\sigma = 6.4 \times 10^{-19} \text{ cm}^2$. A 1 mm-thick sample was used in the measurements. The value of T_0 is then .026. The input intensity at the sample is $I_{in} = 2.2 \times 10^6 \text{ W/cm}^2$. The transmission T was measured to be .127. Therefore

$$W = 8.3 \times 10^{-7} \text{ cm}^2/\text{W}.$$

Substituting into Eq. (11) yields an excited state lifetime of

$$T_1 = 16 \times 10^{-9} \text{ sec.}$$

This lifetime is many orders of magnitude smaller than typical excited state lifetimes of gas molecules (~ 1 msec-torr). This comparison indicates that the coupling of ReO_4^- molecules to the KBr lattice is much stronger than the relaxation mechanisms (collisions) in gases. On the other hand, the ReO_4^- lifetime of 16 nsec is much longer than the 11 psec lifetime measured for the U-center (H^+ ion) local mode in CaF_2 at similar temperatures.⁸ This large difference in lifetimes might be a consequence of the fact that internal modes of molecules can exist without a lattice whereas local modes of monatomic impurities depend on the surrounding lattice for their very existence and hence are more strongly coupled to the lattice. The lifetime of ReO_4^- in KBr will be discussed further after the KI data are presented.

KI Matrix

Since the strength and position of the v_3 absorption of ReO_4^- in KI (and in all alkali halides for that matter) change as a function of temperature, the value of σ will also be temperature dependent. The cross section was measured as a function of temperature between 1.3 K and 300 K and is plotted in Figure III-29. P(42) Q-switched pulses were extracted from the CO_2 laser by means of pulsed-discharge Q-switching described in Section B with typical intensities incident on the sample of $7.3 \times 10^5 \text{ W/cm}^2$. The saturation parameter W was determined from T_0 , T , I_{in} as before and the data is summarized in Table III-3. The results are plotted in Figure III-30a. The result of the KBr + ReO_4^- measurement is indicated by a "+".

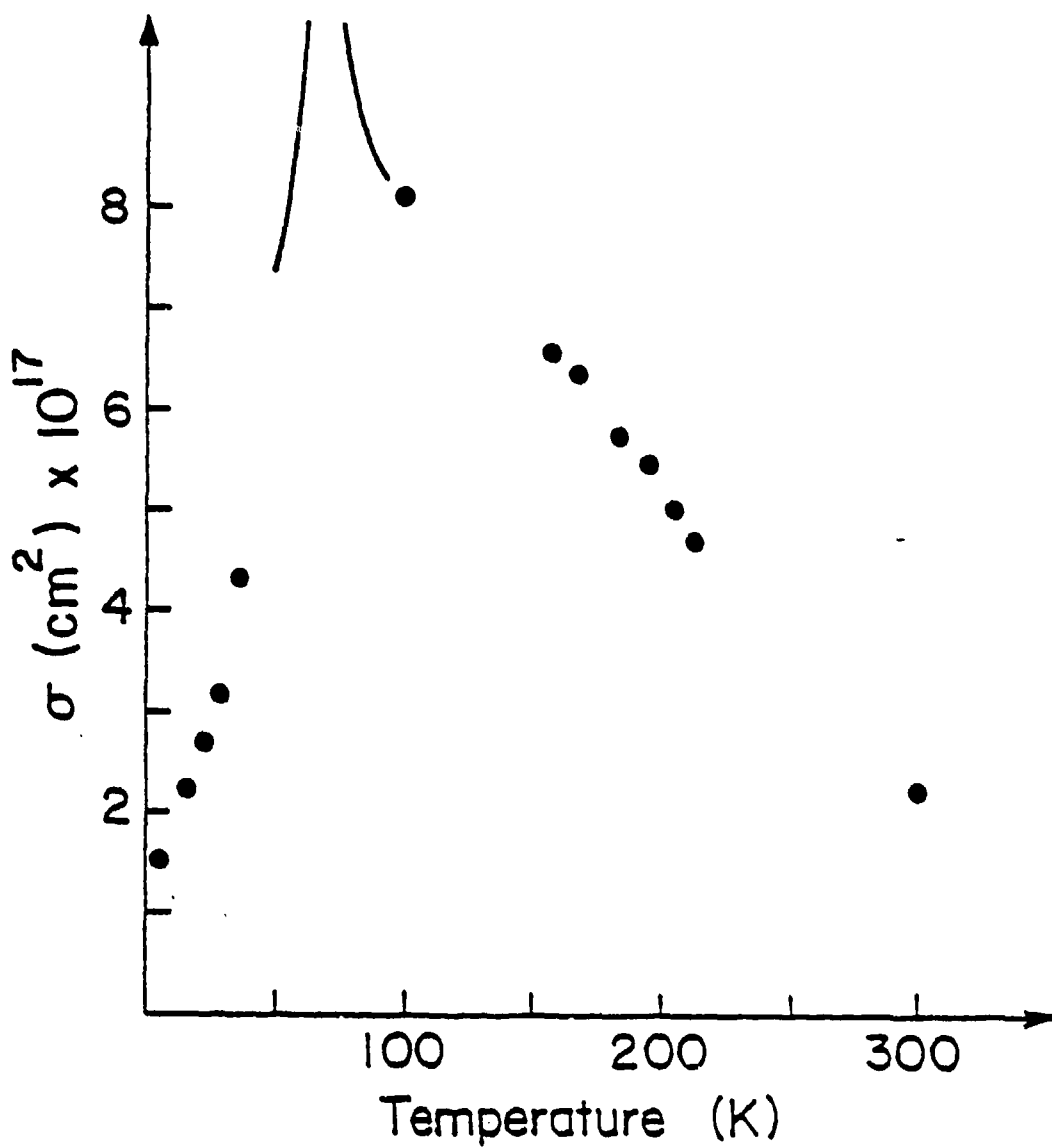


Figure III-29. Cross section of ReO_4^- impurity molecules in KI as a function of temperature. Near 70 K the cross section becomes larger than can be measured using .020-inch thick samples. This is indicated by the two solid curves in the plot.

Table III-3
Partial Summary of Saturation Data for $KI + ReO_4^-$ and $KBr + ReO_4^-$

| <u>KI</u> | | | | | | | <u>KBr</u> | | |
|-----------------|----------------------------------|------------------|--------|-----------|-------------------------------|-------|----------------------|---------|--|
| Temperature (K) | Incident Intensity (MW/cm^2) | $\times 10^{17}$ | T_0 | T_{max} | $W \times 10^6$ (cm^2/W)* | T_1 | $\times 10^{-12}$ | (sec) | |
| 300 | 5.2 | 2.2 | .025 | .05 | .15 | 80 | $\times 10^{-12}$ | | |
| 213 | .73 | 4.7 | .004 | .022 | 2.5 | | $.65 \times 10^{-9}$ | | |
| 205 | .73 | 5 | .0026 | .02 | 2.8 | | $.69 \times 10^{-9}$ | | |
| 194 | .73 | 5.5 | .0014 | .017 | 3.4 | | $.78 \times 10^{-9}$ | | |
| 184 | .73 | 5.7 | .0011 | .012 | 3.4 | | $.74 \times 10^{-9}$ | | |
| 168 | .73 | 6.3 | .0005 | .01 | 4.1 | | $.81 \times 10^{-9}$ | | |
| 159 | .73 | 6.5 | .00044 | .01 | 4.2 | | $.83 \times 10^{-9}$ | | |
| 120 | .73 | 8.1 | .00006 | .05 | 5.8 | | 1.1×10^{-9} | | |
| 35 | .73 | 4.3 | .006 | .43 | 10 | | 3×10^{-9} | | |
| 29 | .73 | 3.2 | .022 | .52 | 9 | | 3.4×10^{-9} | | |
| 1.3 | .0056 | 1.5 | .026 | .36 | 730 | | 1×10^{-6} | | |
| 100 | 2.2 | | .064 | .026 | .13 | .83 | 16×10^{-9} | | |

*The saturation parameter W was calculated assuming a homogeneously broadened line. The validity of this assumption is discussed in the text.

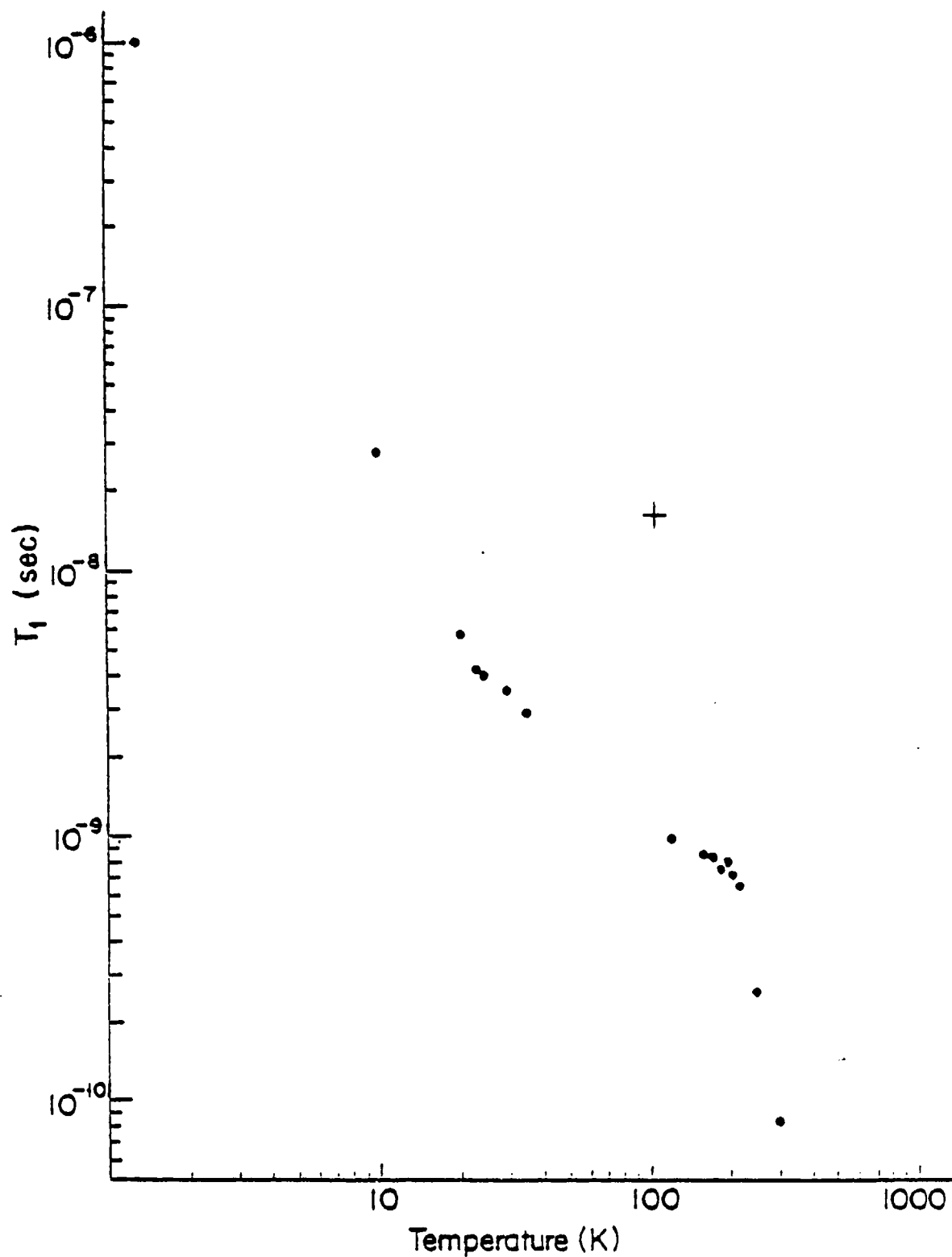


Figure III-30a. Excited state lifetime T_1 of v_3 internal mode of ReO_4^- impurities in KI (solid circles) and KBr (+) as a function of temperature assuming a homogeneously broadened absorption line. The KI lifetimes vary from 80 psec at room temperature to 1 μ sec at 1.3 K.

No data points were obtained between 50 K and 100 K because of the huge absorption by the samples. Even for the thinnest samples used (.05 cm thick) the absorption was too great to permit measurement of T_0 or α (this fact is denoted by solid curves in Figure III-29). It should be pointed out that saturation was easily observed in the 50 K - 100 K region and values for the saturated transmission T were measured and are listed in Table III-3.

The low temperature results in Figure III-30a are not strictly correct because they were calculated using Eqs. (11) and (12) which were derived under the assumption that the absorption line is homogeneously broadened. At low temperatures the line is inhomogeneously broadened and the treatment found in Section E2b should be used. However, due to the sharp absorption line and the limited resolution of the near infrared interferometer the absorption resonance cannot be resolved below 100 K and hence it is impossible to determine at what point the line becomes inhomogeneously broadened. Even if this crossover point were known, there is another obstacle that would impede calculation of T_1 . As was pointed out in Section E, in the case of inhomogeneously broadened absorbers if one determines the saturation parameter W one still needs to know T_2 in order to determine T_1 (see Eq. (20)) and there is no direct way of measuring T_2 . However, in spite of these difficulties, one fairly meaningful calculation can still be made for the 1.3 K data.

In the case of inhomogeneous broadening the onset of saturation occurs when the second term under the radical in Eq. (17) becomes comparable to 1, i.e.

$$\frac{g_1 4\pi|\mu|^2 I_{th}(1 + g_0/g_1) T_1 T_2}{\pi^2 c} \sim 1.$$

Inverting this formula gives

$$T_1 T_2 \sim \frac{\pi^2 c}{g_1 4\pi|\mu|^2 I_{th}(1 + g_0/g_1)}.$$

Here I_{th} is the threshold intensity for onset of saturation, $g_0 = 1$ and $g_1 = 3$. The transition dipole moment can be determined from the sum rule⁴⁸

$$\int ad\tilde{v} = \frac{4\pi^2 \tilde{v}}{(\epsilon)^2 \pi c} \left(\frac{\epsilon+2}{3} \right)^2 N_{tot} |\mu|^2$$

where ϵ is the dielectric constant. The integrated line strength was measured from interferometric data for a number of temperatures between 100 K and 300 K (the absorption line was fully resolved at these temperatures). The measured values were all within 10% of each other with the average being

$$\int ad\tilde{v} = 110 \text{ cm}^{-2}.$$

Then $|\mu|^2 = 3.9 \times 10^{-38}$ (cgs). The threshold saturating power at 1.3 K is 27 W/cm². Therefore

$$T_1 T_2 \sim 5.7 \times 10^{-17} \text{ sec}^2.$$

From the definitions of T_1 and T_2 it is obvious that $T_1 \geq T_2$. If we assume that $T_1 = T_2$ at 1.3 K, then

$$T_1 = 7.5 \times 10^{-9} \text{ sec.}$$

Figure III-30b shows a plot of T_1 vs. temperature using the above value of T_1 at 1.3 K and the high temperature data (>100 K) from Figure III-30a.

Since at finite temperatures $T_2 \leq T_1$ the 1.3 K value of T_1 just

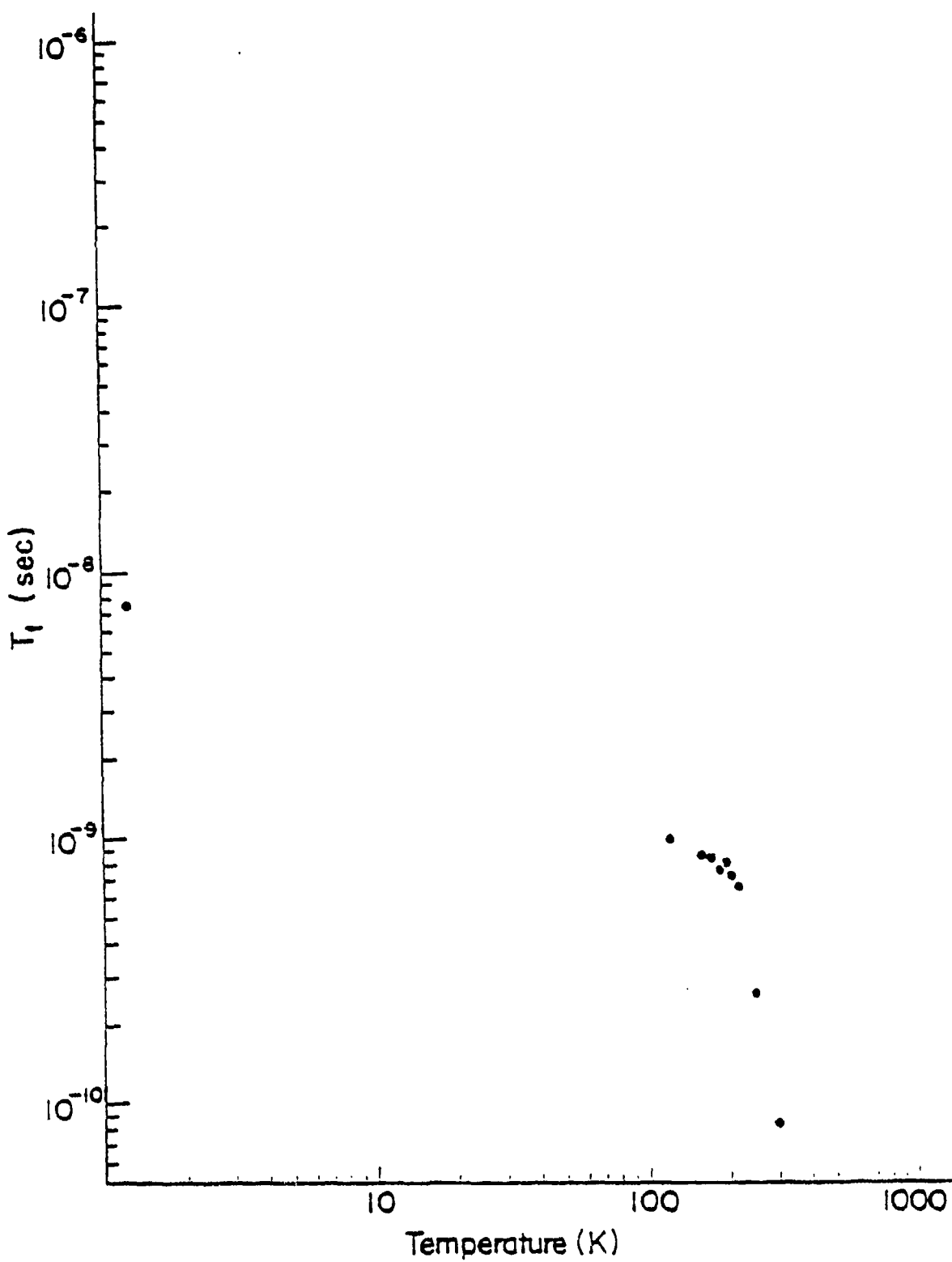


Figure III-30b. Excited state lifetime T_1 of the v_3 vibrational mode of ReO_4^- impurities in KI as a function of temperature assuming homogeneous broadening above 100 K and extreme inhomogeneous broadening at 1.3 K.

calculated represents a lower bound for T_1 (and an upper bound for T_2). The upper bound for T_1 at 1.3 K is the value computed assuming homogeneous broadening. Figure III-30c combines the data in Figures III-30a and III-30b and the shaded area represents the possible range of T_1 values. Thus far there is no theoretical explanation for the shape of the ReO_4^- lifetime data in KI.

The value of T_1 in KBr at 100 K is an order of magnitude greater than T_1 in KI at the same temperature. This result indicates that the relaxation mechanism of the ReO_4^- vibrations is more complicated than simple multiphonon relaxation. A multiphonon relaxation model would predict shorter lifetimes in KBr lattices than in KI lattices because the KBr lattice phonons have higher frequencies than the KI phonons and consequently it would take fewer phonons to couple the excited vibrational state to the ground state in KBr than in KI. The fact that KI lifetimes are shorter than KBr lifetimes might be a consequence of the qualitatively different absorption behavior of $\text{KI} + \text{ReO}_4^-$ and $\text{KBr} + \text{ReO}_4^-$ in the region of the v_3 resonance. The KI samples exhibit additional nearby absorptions and at high temperatures have much broader v_3 absorption lines than the KBr samples (indicating motion of the ReO_4^- molecules. It is possible that the ReO_4^- molecules in the v_3 excited state in KI relax to the nearby states and then relax to the ground state. This additional relaxation mechanism to nearby states would greatly shorten the v_3 excited state lifetime of ReO_4^- .

A second possible explanation might lie in the fact that in the smaller KBr lattice the ReO_4^- impurities because of their size

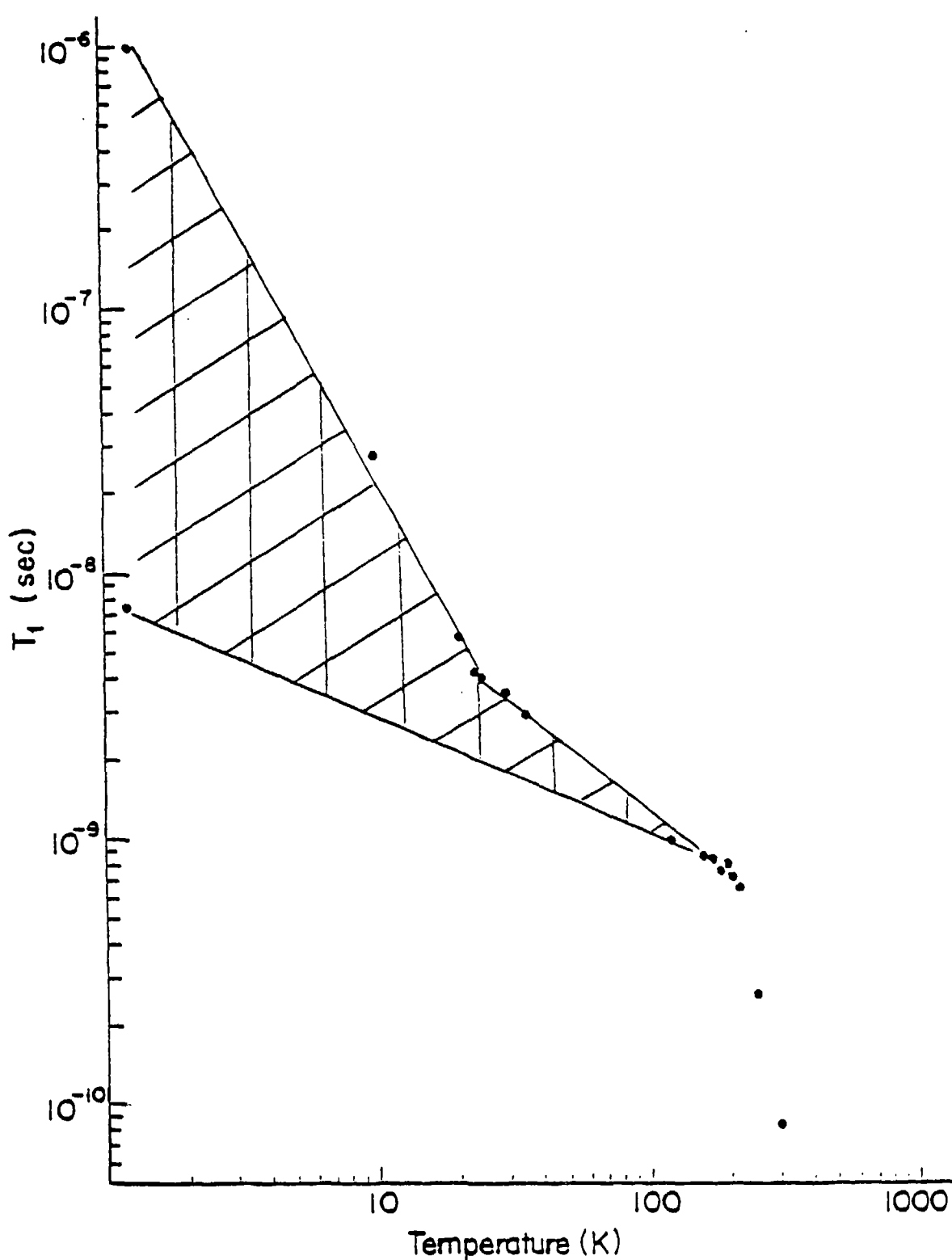


Figure III-30c. Range of possible excited state lifetimes (shaded region) of v_3 vibrational mode of ReO_4^- impurities in KI as a function of temperature.

(tetrahedrons $\sim 1.7 \text{ \AA}$ on a side) displace more than one ion (i.e. 2 Br⁻ ions and 1 K⁺ ion) in the host lattice. If this happened, then the KBr + ReO₄⁻ system would be intrinsically different from the KI + ReO₄⁻ system and no comparison between the excited state lifetimes could be made.

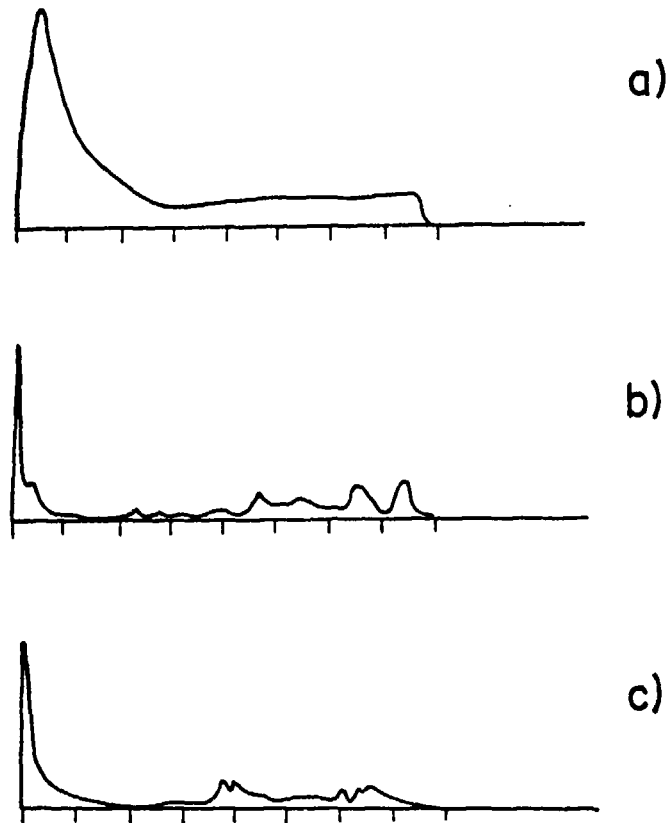
Although this section has discussed incoherent saturation, one comment should be made about coherent optical processes. Although no coherent optical effects can be observed with the Q-switched laser (because $T_2 < \text{laser pulse width } \tau$), it is conceivable that with a mode-locked CO₂ laser with pulse widths $\sim 1 \text{ nsec}$ coherent optical effects such as photon echoes could be observed in KI + Cs⁺ + ReO₄⁻ samples at 1.3 K (at this temperature $T_1 \sim T_2 \sim 7.5 \text{ nsec} < \tau$). This would represent the first observations of coherent optical effects in solids in the infrared. Such experiments would also provide direct means for measuring T_2 .

H. Pulse Distortion and Attenuation

In the process of studying the saturation and lifetime properties of ReO₄⁻ in KI a number of peculiar effects were observed. Laser pulses ($P(42) 922.9 \text{ cm}^{-1}$) transmitted through the sample below 10 K were not only attenuated but also distorted. The pulse attenuation and distortion has two rather remarkable properties. First of all, the reshaping is not the pulse narrowing which is commonly observed in saturable absorbers. Instead, multiply-peaked pulses are observed and in some cases bizarre oscillations in the transmitted pulses have been recorded. Secondly, this pulse reshaping occurs in two totally different time regimes.

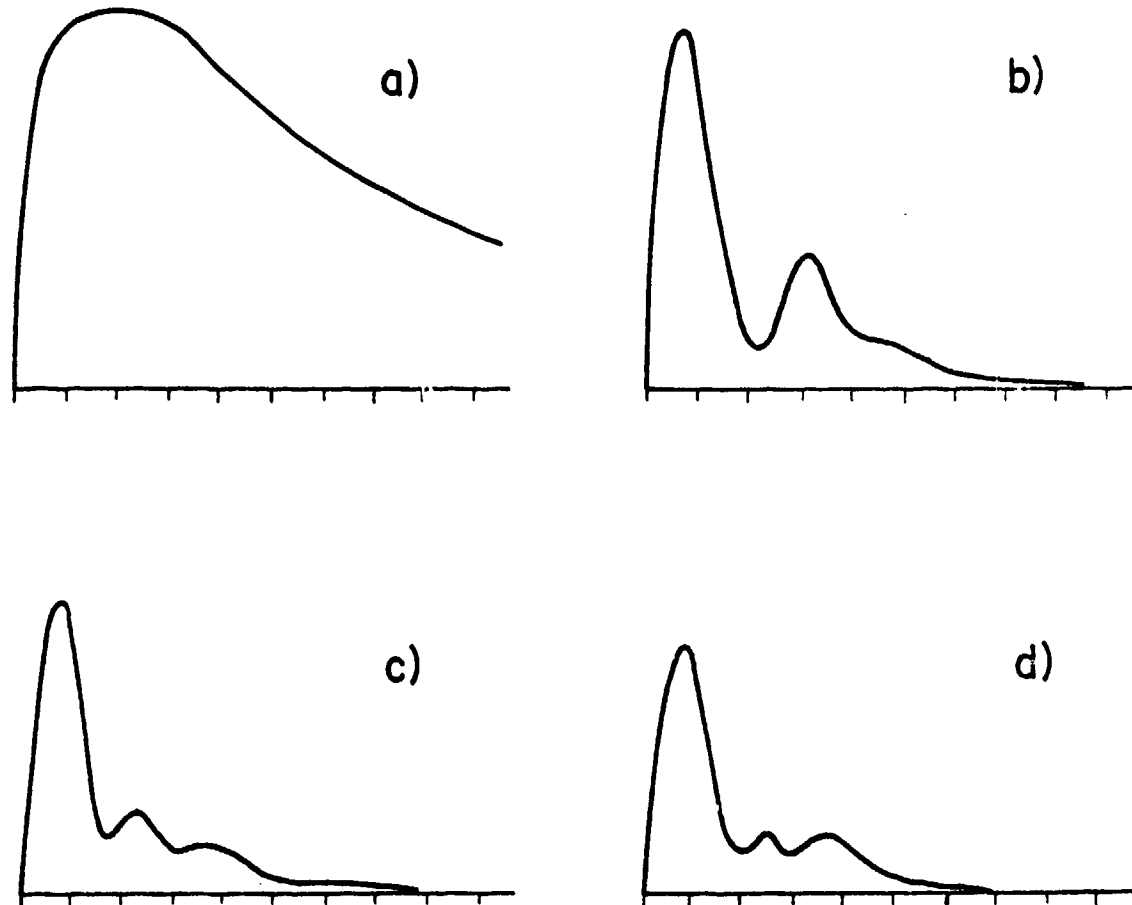
Millisecond-long pulses as well as μ sec pulses are reshaped (the reshaping mechanism is not necessarily the same for the two time regimes).

Figure III-31a shows a laser pulse about 8 msec long before it enters the sample. Figures III-31b,c show the transmitted pulse through two different regions of the sample (sample thickness = .056 inch). The vertical scales for the transmitted pulses are a factor of ten smaller than the vertical scale of the input pulse. Note that the main pulse is radically shortened (primarily on the trailing edge) while the tail of the pulse exhibits large oscillations between 0 and what appears to be a tail envelope of the input pulse. These oscillations change shape and position as the focus is moved to different parts of the sample. The main portion of the pulse was magnified and is shown in Figure III-32a (input pulse) and Figure III-32b-d (transmitted pulses). Besides being narrower than the input pulse the transmitted pulse also shows multiple peaks. These multiply-peaked pulses usually have two distinct peaks with a shoulder on the second peak or three distinct peaks. As the power of the input pulses was reduced, the shape of the transmitted pulses became identical to the input pulse shape. The power dependence of these effects indicates that some sort of heating might be the source of the effect. This conjecture was dispelled by calculations of the amount of heating caused by the pulses (the pulse energies were several tens of millijoules). Even the most conservative assumptions about heat transfer from the sample to the 1.3 K He bath yielded temperature changes of only a few degrees. This change in temperature is not enough to



Horizontal Scale 1 msec/div.

Figure III-31. Pulse distortion by .021-inch thick KI + .2% Cs⁺ + .2% ReO₄⁻ sample at 1.3 K. a) Input pulse shape. b,c) Transmitted pulse shape through different parts of the sample. Note the narrowing of the main pulse and the oscillation in the tail. The vertical scales of Figures b and c are a factor of 10 smaller than that in Figure a (i.e., there is quite a bit of attenuation of the laser pulse by the sample).

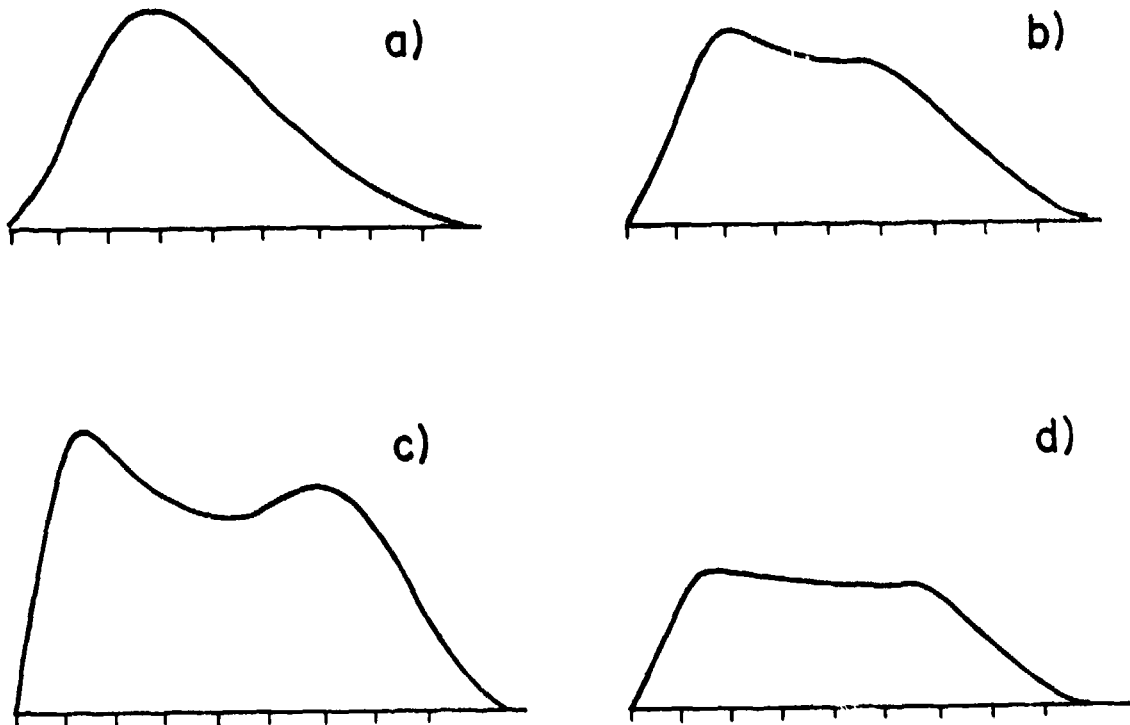


Horizontal Scale 0.1 msec/div.

Figure III-32. Pulse distortion of the main portion of the pulse shown in Figure III-31a. a) Input pulse shape. b-d) Transmitted pulse shapes through various parts of the sample. Note the narrowing and the multiple peaks. The vertical scales of b, c, and d are 10 times smaller than the vertical scale of a.

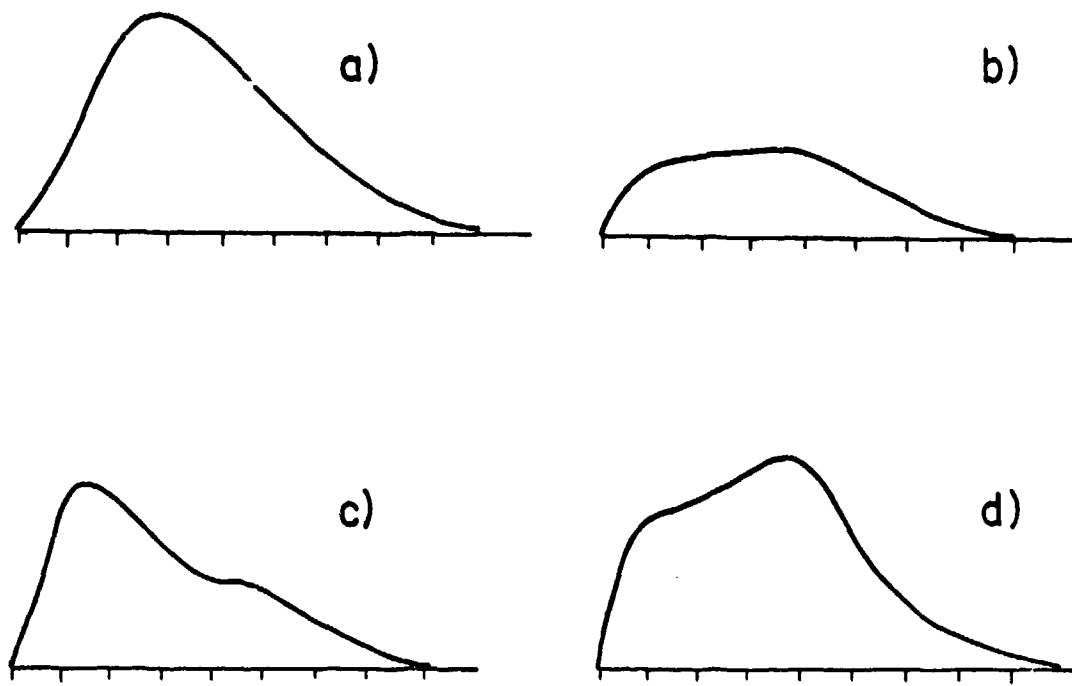
change the absorption coefficient of the sample at the laser frequency. Second sound in the helium bath or in the sample also failed as possible explanations for these effects.

Pulse reshaping on μ sec time scales was observed in several samples of $KI + .2\% ReO_4^- + .2\% Cs^+$, each of different thickness. The reshaping occurred at temperatures below 18 K. At higher temperatures there was no distortion aside from some narrowing due to saturation. Figure III-33a shows an undistorted Q-switched pulse ($P(42)$, (00^01-10^00) band) which was focused onto a .021-inch thick sample. Figures III-33b-d show the transmitted pulses at 10 K, 12 K, and 14 K respectively. It appears that the incident pulse is "broken up" by the sample. This pulse reshaping was reproduced in this sample several times with similar results each time. It was initially thought that this pulse break-up was the break-up of an $n2\pi$ pulse (this is one of several coherent optical effects discussed by Allen and Eberly⁴⁶). However, two pieces of experimental evidence have shown this not to be the case. First of all, if αL (where L = sample thickness and α = absorption coefficient) is increased, then the amount of breakup should increase, i.e., the incident pulse should break up into distinct pulses as it passes through the sample. This effect was not observed when L was increased by a factor of 3. The pulse distortion remained about the same (Figures III-34a-d). Secondly, the measurement of T_1 and T_2 at these temperatures showed that $T_2 < \tau$ (the laser pulse length). For coherent optical effects such as pulse breakup to be observed, τ must be shorter than both T_2 and T_1 .⁴⁶ Therefore, this reshaping is not the breakup of an $n2\pi$ pulse.



Horizontal Scale 100 nsec/div.

Figure III-33. Pulse distortion by .021-inch thick KI + .2% Cs^+ + .2% ReO_4^- sample. a) Input pulse shape. b-d) Transmitted pulse shape at sample temperatures of 10K, 12K, and 14K respectively. The vertical scales in b, c, and d are 10 times smaller than in a (i.e., pulse area is not conserved).



Horizontal Scale 100 nsec/div.

Figure III-34. Pulse distortion by .164-inch thick KI + .2% Cs^+ + .2% ReO_4^- sample. a) Input pulse shape. b-d) Transmitted pulse shape at sample temperatures of 5K, 1.3K, and 5.5K respectively. The vertical scales in b, c, and d are 10 times smaller than in a.

Continued investigation showed that this pulse reshaping effect had a very distinct threshold power associated with it ($\sim 500 \text{ kW/cm}^2$). This threshold value is about the same for all temperatures between 5 K and 15 K but is about 100 kW/cm^2 higher for the 1.3 K to 5 K and 15 K to 18 K temperature ranges. Pulses with lower peak powers passed through the sample undistorted while pulses with peak powers greater than the threshold value were not only attenuated but distorted as well. It then became apparent that the reshaped pulses were actually the incident pulses with their peaks absorbed to various degrees. The threshold effect, as well as the reshaping effect just mentioned, were demonstrated fairly dramatically in a simple experiment which was repeated on samples of several different thicknesses with identical results. P(42) Q-switched laser pulse were focused on a sample which was at some temperature less than 10 K (typically 1.3 K). The absolute signal level of the reshaped pulses was noted. The incident laser power was then decreased by about 20%. However, the signal level of the transmitted pulses went up instead of down and the pulse distortion nearly disappeared. This type of behavior can only be explained by a threshold effect in which pulses below threshold are undistorted and above threshold the peak of the pulse is missing and therefore the pulses appear to be weaker.

The pulse reshaping is probably not stimulated Raman scattering (which is a threshold effect) into the v_2 state. The scattered photon in such a process would have a frequency $\tilde{v}_L - \tilde{v}_2 = 583 \text{ cm}^{-1}$ (\tilde{v}_L = laser

frequency, ν_2 = frequency of ν_2 internal mode which is Raman active). No signal was observed when an OC/I step filter which is opaque to CO₂ laser frequencies and transparent below 870 cm⁻¹ was placed between the sample and the detector. The absence of 583 cm⁻¹ radiation rules out stimulated Raman scattering as an explanation for the pulse reshaping observed in our samples.

Another threshold effect, namely stimulated Brillouin scattering, cannot be totally ruled out as a possible explanation. At first glance it would appear that since the scattered photons are of nearly the same frequency as the pump photons, no energy should be removed from the beam due to such a process (and therefore stimulated Brillouin scattering could not explain the observed effect). However, in such processes it is possible to have scattered photon in the backward direction anti-parallel to the pump radiation. If stimulated Brillouin processes were occurring in the backward direction this would rob the beam in the forward direction of photons and flatten out or depress the peaks of the pulses. The threshold power for stimulated Brillouin processes is⁴⁸

$$P(\text{W/cm}^2) = \frac{8Tc\varepsilon^2\alpha_s\alpha_a}{\gamma^2 k_s^2 k_a^2}$$

where T = bulk modulus of sample

c = speed of light

ε = permittivity of the sample

α_s = attenuation of the scattered optical wave by the sample

α_a = acoustic attenuation constant

γ = electrostrictive coefficient

k_s = wavevector of scattered optical wave

k_a = wavevector of acoustic wave.

Since no values of α_a could be found for KI the value of α_a for quartz or sapphire was used. Using

$$T \sim 5 \times 10^{10} \text{ N/m}^2$$

$$\gamma \sim 10^{-11} \text{ (mks)}$$

$$\epsilon \sim 1.3 \times 10^{-11} \text{ (mks)}$$

$$k_s \sim \frac{2\pi}{\lambda} \sim 5.8 \times 10^5 \text{ m}^{-1}$$

$$k_a \sim \frac{\omega_a}{v_a} \sim \frac{2\omega_s n}{c} \sim 1.7 \times 10^6 \text{ m}^{-1}$$

$$\alpha_a \sim 20 \text{ cm}^{-1},$$

we have

$$P_T \sim 4 \times 10^9 \alpha_s (\text{W/cm}^2).$$

This means that the threshold power would be 500 kW/cm^2 (the measured threshold power for our effect) if $\alpha_s \sim 10^{-4} \text{ cm}^{-1}$. Even taking into account a possible error of several orders of magnitude in the value of α_a , this value of α_s is excessively small especially when one remembers that in the region of the absorption resonance the optical attenuation is much higher. However, one must remember that the absorption line is being totally bleached by the laser radiation. Therefore, if the frequency of the scattered photon lies within the hole burned by the laser radiation it is conceivable that the absorption coefficient seen by the scattered radiation is very small. In any case, to rule out or to confirm stimulated Brillouin scattering as the explanation for our

effect, the frequency dependence of the radiation emitted by the sample in the forward and especially the backward direction would need to be determined. Radiation shifted in frequency from the main laser line by less than several wavenumbers would indicate that the observed effect is stimulated Brillouin scattering.

In some stimulated Raman and Brillouin experiments the measured threshold input powers have been several orders of magnitude smaller than those predicted by theory. These anomalous effects are due to a phenomenon called self-focusing in which the medium in the presence of intense laser radiation acts as a positive lens and focuses the laser light. Self-focusing is also a threshold effect (i.e., the threshold occurs when the self-focusing overcomes the spreading due to diffraction) and in some materials the self-focusing input threshold is lower than the threshold for stimulated Raman or Brillouin scattering. However, when the self-focusing threshold is exceeded, the sample focuses the laser intensity in itself and this can lead to intensities sufficiently high to exceed stimulated Raman and Brillouin thresholds. If self-focusing occurred in our samples then perhaps threshold powers for Brillouin scattering (e.g., 4×10^9 for $\alpha_s = 1 \text{ cm}^{-1}$) could be exceeded even though a power density less than 1 MW/cm^2 impinges on the sample. However, Allen and Eberly point out that for a saturable absorber (homogeneously broadened) self-focusing can occur only if the laser frequency is greater than the resonance absorption frequency. In our samples the reverse is true* and therefore it appears that self-focusing

*The relative position of the absorption resonance and the P(42) CO₂ laser line is shown in Figure III-35.

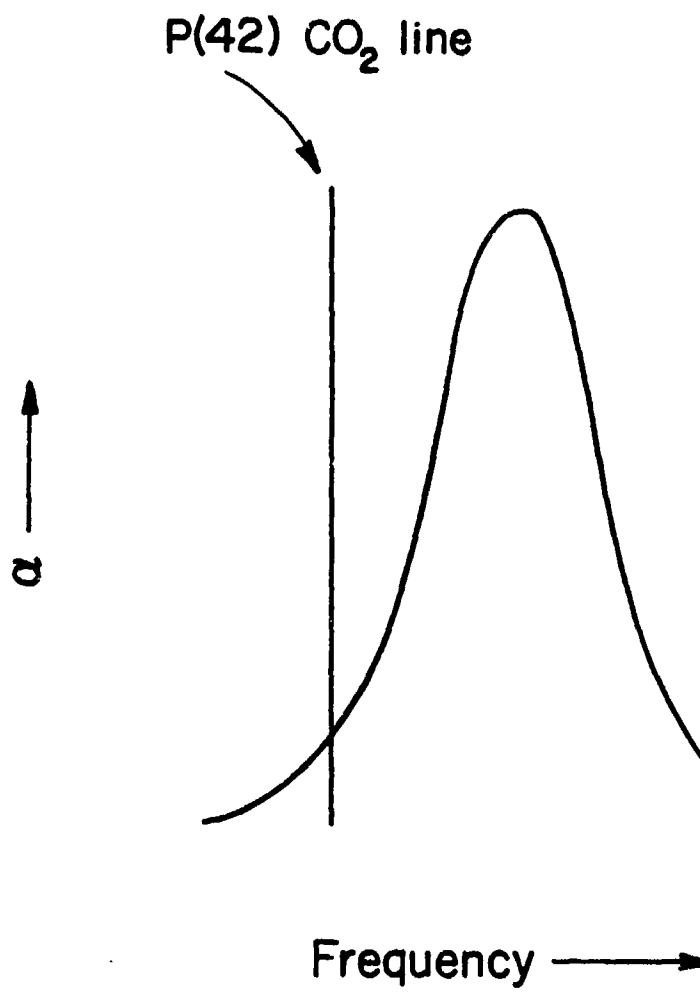


Figure III-35. Relative orientation of the P(42) CO₂ laser frequency to the absorption line of ReO₄⁻ impurities in KI + Cs⁺ at low temperatures.

does not occur in our samples. It should be pointed out that the theory of Allen and Eberly is for homogeneously broadened systems and that at very low temperatures the ReO_4^- absorption in KI is inhomogeneously broadened. The theory for inhomogeneously broadened system is extremely complicated and to the best of our knowledge has not been developed yet. As far as self-focusing is concerned, the inhomogeneously broadened absorption can be thought of as a superposition of homogeneously broadened absorptions. The homogeneous absorptions with center frequencies below the laser frequency give rise to self-focusing while those with center frequencies above the laser frequency give rise to defocusing. Since a large portion of the absorption is at higher frequencies than the laser frequency (Figure III-35) the sample will not self-focus the laser beam.

There are two other Raman processes that might be important in explaining the effect but are unobservable with our setup. The first such process assumes the ground state actually consists of a manifold of levels which come about due to the motion of the impurities. The Raman transition begins in this ground state manifold. A laser photon (922.9 cm^{-1}) is scattered into a photon of slightly different frequency and the ReO_4^- molecule is left in a different level of the ground state process. Since the sample is totally saturated by the laser pulses the excited ν_3 state of ReO_4^- will have a nonzero population during the laser pulses. Because the excited state has a finite population, there are certain transitions that can originate from this level. Among these is a Raman transition (and possibly a stimulated Raman transition) which begins in the first excited state of ReO_4^- and scatters a P(42) photon

(922.9 cm⁻¹) into a 881 cm⁻¹ photon and leaves the ReO₄⁻ molecule in the ν₁ vibrational state (which is Raman active). This process is diagrammed in Figure III-36. If this transition or the ground state manifold transition went stimulated, then the transmitted laser pulses could have the form observed in our experiments. Unfortunately, our various step and notch filters cannot resolve the laser photons from the scattered photons (881 cm⁻¹) and therefore we have no way of knowing whether such processes are occurring.

Conclusions and Future Experiments

The pulse reshaping effects observed in KI + Cs⁺ + ReO₄⁻ samples at temperatures less than 18 K have threshold input powers of about 500 kW/cm² associated with them. These effects have been shown not to be breakup of n2π pulses. No emission at 583 cm⁻¹ has been observed which indicates that these effects are not stimulated Raman scattering processes originating in the ground state of ReO₄⁻. Stimulated Raman scattering originating from the laser-populated first-excited ν₃ state of ReO₄⁻ and stimulated Brillouin scattering cannot be ruled out as possible explanations of the observed effect because we were not able to study the frequency dependence of the light emitted from the sample in the region of the pump laser frequency. A spectral analysis of the radiation from the sample in the forward and backward direction would most likely explain the nature of the observed threshold effect. Certain information as to the nature of the effect could be obtained without doing spectral analysis of the emitted radiation. By using the 1000-Ω resistor attached to the sample as a bolometer (using the bias circuit

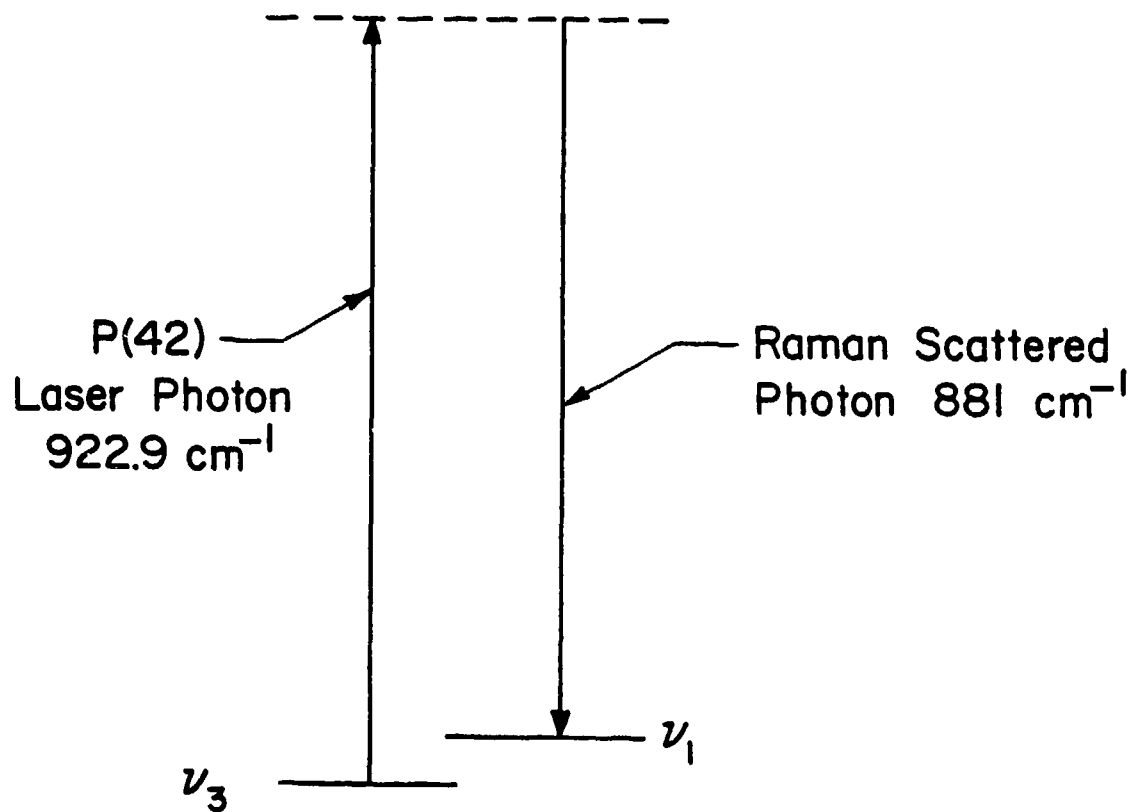


Figure III-36. Diagram of a Raman scattering process originating in the ν_3 vibrational state and ending in the ν_1 vibrational state.

described in Section C) one could monitor the heat dissipated in the sample as a function of input power. If, at the threshold power, the heating shows a sudden increase the threshold process involves phonons whereas if the heating curve shows no sudden increase with input power in the vicinity of the threshold, then the process involves γ -radiation and excludes Brillouin scattering as a possible explanation.

Since the v_3 vibrational level of the ReO_4^- impurities is totally saturated by Q-switched laser pulses there is an opportunity to study the excited-state spectrum (i.e., infrared active transitions originating in the v_3 vibrational level) of the ReO_4^- -alkali halide system. This experiment could be performed using a grating monochromator and the Q-switched CO_2 laser. A fast detector monitoring the output of the monochromator beam would exhibit "negative" pulses when a transition to the excited state of ReO_4^- occurs. The entire excited-state spectrum of ReO_4^- in alkali halides could be mapped out by sweeping the frequency of the grating monochromator.

Coherent optical effects might be observable with a mode-locked CO_2 laser putting out nanosecond pulses. Faster detectors and a mode-locked laser would be required but the dividends could be quite spectacular. Not only would this provide a direct measure of T_2 at 1.3 K but it could conceivably open a new field of infrared coherent optical effects in solids.

References

1. I. Maslakowez, Z. Phys. 51, 696 (1928).
2. R. Robertson, J. J. Fox, A. E. Martin, Phil. Trans. Roy. Soc. Lond. A232, 463 (1934).
3. G. Schäfer, J. Phys. Chem. Solids 12, 233 (1960).
4. A. S. Barker, Jr., and A. J. Sievers. Rev. Mod. Phys. 47, Suppl. 2 (1975).
5. T. F. Deutsch, J. Phys. Chem. Solids 34, 2091 (1973).
6. M. Hass, J. W. Davisson, P. H. Klein, and L. L. Boyer, J. App. Phys. 45, 3959 (1974).
7. A. R. Chraplyvy, to be published in Applied Optics, Sept. 1977.
8. L. C. Lee, Ph.D. Thesis, University of Southern California, 1971, unpublished.
9. The evolution of the study of ultratransparent materials is well documented by the various conferences on High Power Infrared Laser Window Materials listed below.
First Conference on High Power Infrared Laser Window Materials, AFCRL-71-0592 (ed. by C. Sahagian and C. A. Pitha), 1971.
Second Conference on High Power Infrared Laser Window Materials, AFCRL-TR-73-0372 (ed. by C. A. Pitha), 1972.
Third Conference on High Power Infrared Laser Window Materials, AFCRL-TR-73-0085 (ed. by C. A. Pitha and B. Bendow), 1973.
Proceedings of the Fourth Annual Conference on Infrared Laser Window Materials, AFML-TR-75-79 (1974).
Proceedings of the Fifth Annual Conference on Infrared Laser Window Materials, AFML-TR-76-83 (1976).
10. For a review of a number of such techniques see L. H. Skolnik, Optical Properties of Highly Transparent Materials, S. Mitra and B. Bendow, ed., Plenum Press, 1975.
11. V. Rehn, O. Kyser, and V. Jones, Second Conf. on High Power Infrared Laser Window Materials, AFCRL-TR-73-0372 (ed. by C. A. Pitha), 1972.
12. G. Birnbaum, E. Cory and K. Gow, Appl. Optics 13, 1660 (1974).
13. F. Deutsch, J. Phys. Chem. Solids 34, 2091 (1973).
14. T. F. Deutsch and R. I. Rudko, "Research in Optical Materials and Structures for High Power Lasers", Raytheon Research Div., Waltham, Mass., 1973.

15. D. Stierwalt and R. Potter, J. Phys. Chem. Solids 23, 99 (1962).
16. D. Stierwalt, Second Conf. on High Power Infrared Laser Window Materials, AFCRL-TR-73-0372 (ed. by C. A. Pitha), 1972.
17. L. Skolnik, M. Clark, R. Koch, W. McCann and W. Shields, Fourth Conf. on Infrared Laser Window Materials (ed. by C. L. Anderson and C. L. Strucker), 1975.
18. L. Skolnik, A. Hordvik, and A. Kahan, Appl. Phys. Lett. 23, 117 (1973).
19. A. Nurmiko, Appl. Phys. Lett. 26, 175 (1975).
20. E. L. Kerr, Appl. Opt. 12, 2520 (1973).
21. A. Rosencwaig, Opt. Comm. 7, 305 (1973).
22. A. Rosencwaig, Science 81, 657 (1973).
23. J. H. Parks, D. A. Rockwell, T. S. Colbert, K. M. Lakin, and D. Nih, Appl. Phys. Lett. 25, 537 (1974).
24. A. Hordvik, High Power Infrared Laser Window Materials Annual Report (ed. by J. Bruce and W. Ewing), 1976.
25. F. Horrigan, C. Kline, R. Rudko, and D. Wilson, Microwaves 8, 68 (1969).
26. R. Weil, J. Appl. Phys. 41, 3012 (1971).
27. T. Deutsch and R. Rudko, Raytheon Research Div. Final Tech. Report, Contract No. DAAH01-72-C-0194 (1973).
28. B. Bendow, A. Hordvik, H. Lipson and L. Skolnik, Some Aspects of Optical Evaluation of Laser Window Materials, AFCRL Report No. AFCRL-72-0404 (1972).
29. First Conf. on High Power Infrared Laser Window Materials, AFCRL-71-0592 (ed. by C. Sahagian and C. A. Pitha), 1971.
30. Second Conf. on High Power Infrared Laser Window Materials, AFCRL-TR-73-0372 (ed. by C. A. Pitha), 1972.
31. J. A. Harrington and M. Hass, Phys. Rev. Lett. 31, 710 (1973).
32. M. Hass, J. W. Davission, H. Rosenstock, J. Babiskin, Appl. Optics 14, 5 (1975).
33. Lansing Operation Manual, Lock-in Stabilizer Model 100-211

34. A. J. Sievers, R. O. Pohl, A. R. Chraplyvy, D. Pramanik, and G. Schmidt, Semiannual Technical Progress Report, Contract F19628-75-C-0177 (Feb. 1976).
35. A. J. Sievers, R. O. Pohl, A. R. Chraplyvy, D. Pramanik and G. Schmidt, Annual Technical Progress Report, Contract F19628-75-C-0177 (July 1976).
36. A. J. Sievers, R. O. Pohl, R. Alexander, Y. Chabal, A. R. Chraplyvy, D. Pramanik, G. Schmidt, Semiannual Technical Progress Report, Contract F19628-75-C-0177 (Jan. 1977).
37. M. Sparks and L. J. Sham, Phys. Rev. B₈, 3037 (1973).
38. D. L. Mills and A. A. Maradudin, Phys. Rev. B₈, 1617 (1973).
39. T. C. McGill, R. W. Helwarth, M. Manger and H. V. Winston, J. Phys. Chem. Solids 34, 2105 (1973).
40. P. H. Klein, NRL Memorandum Report 3266 (1976).
41. M. Geller and A. J. Sievers, unpublished results.
42. K. Nakamoto, Infrared Spectra of Inorganic and Coordination Compounds, John Wiley and Sons (1963), p. 107.
43. A. K. Chin, Ph.D. thesis, Cornell University, 1977, unpublished.
44. K. C. Johnson, Ph.D. thesis, Cornell University, 1972, Materials Science Center Report #1832.
45. H. H. Claassen and A. J. Zielen, J. Chem. Phys. 22, 707 (1953).
46. L. Allen and J. H. Eberly, Optical Resonance and Two-Level Atoms, John Wiley and Sons (1975).
47. A. Yariv, Quantum Electronics, John Wiley and Sons (1968), p. 267.
48. Ibid., p. 438.

MISSION
of
Rome Air Development Center

RADC plans and conducts research, exploratory and advanced development programs in command, control, and communications (C³) activities, and in the C³ areas of information sciences and intelligence. The principal technical mission areas are communications, electromagnetic guidance and control, surveillance of ground and aerospace objects, intelligence data collection and handling, information system technology, ionospheric propagation, solid state sciences, microwave physics and electronic reliability, maintainability and compatibility.